The extended light profiles of the Sculptor and Ursa Minor dwarf galaxies: Innate nature or tidal nurture?

by

Daniel A. Boyea
Bachelor of Science, The Ohio State University, 2023

A Thesis Submitted in Partial Fulfillment of the Requirements for the Degree of

MASTER OF SCIENCE

in the Department of Physics and Astronomy

We acknowledge and respect the Lək̓ʷəŋən (Songhees and Xʷsepsəm/ Esquimalt) Peoples on whose territory the university stands, and the Lək̓ʷəŋən and W̱SÁNEĆ Peoples whose historical relationships with the land continue to this day.

The extended light profiles of the Sculptor and Ursa Minor dwarf galaxies: Innate nature or tidal nurture?

by

Daniel A. Boyea
Bachelor of Science, The Ohio State University, 2023

Supervisory Committee

Dr. Julio Navarro, Supervisor
Department of Astronomy

Dr. Kim Venn, Departmental Member
Department of Astronomy

Abstract

The satellite galaxies of the Milky Way (MW), except the Magellanic Clouds, are all dwarf spheroidals (dSphs)—gas-free, non-rotating, dark-matter-dominated stellar systems. The light profiles of dSphs typically follow an exponential law, with a sharply declining outer density (Muñoz et al. 2018). Yet systems like the Sculptor (Scl) and Ursa Minor (UMi) dSphs host member stars out to ∼10 effective radii, indicating outer deviations from an exponential law. The origin of these extended profiles is unclear, possibly arising from Galactic tides or intrinsic properties. In this thesis, we review the evidence for extended light profiles in Scl and UMi, validating the Bayesian membership catalogue of Jensen et al. (2024). To evaluate if tides can produce these density features, we conduct idealized N-body simulations of both galaxies in the tidal field of the Milky Way. We find that neither dwarf experiences tides strong enough to affect their stellar distribution. One complication is that Sculptor's orbit is strongly influenced by the presence of the Large Magellanic Cloud (LMC). Our N-body models still suggest that the combined tides of the LMC and MW are unable to explain Scl's outer profile. We conclude that the extended light profiles of Scl and UMi are not of tidal origin. They are instead likely innate, possibly explained by past mergers, accretion events, or episodic star formation.

Table of Contents

List of Figures

List of Tables

Acknowledgments

While written by my hand, I cannot pretend that I alone created this work. I am ever thankful and greatly indebted to the multitude of people who have supported, inspired, and nurtured me as a human being.

To my supervisor, Julio Navarro, for being the critical eye and guiding reason to this work. I will always approach research differently now. To Giuseppina for your helpful feedback and questions during my defence.

To Raphaël, who has helped inspire and direct this project, and to everyone who has shared ideas and opportunities along the way: Isabel, Jens, Eduardo, Jorge, David, Justin, Eugene, Azi, José, and many others.

To Jax for you guidance and personal support for this project.

To all of my new friends I have made along the way—Ruxin, Aviv. To Pranav, Ted, Jono, Adrianne, Praneet, Will, Maeve, Ewoud, Anne, Anya, Shoshanah. To Akshara and Simon for all your personal and professional advice. We have built a wonderful graduate community. To all the students who have since moved on but still inspire me: Bobby, Leo, Ryan, Katie, Fletcher, Ayden, Maheyer, Jess, Dhwani, Spencer, Mallory, Omar, Isaac, and Dasha.

To my friends across UVic: Wyatt, Rosemary, Maggie. To the Linguistics extended family and team *adequate*: Melody, Lily, Gillian, Stephen, Jamie, Chloë, Alyssa, Kyle, and Marcus. You are all wonderful human beings, cooks, and always a joy to spend time with.

To my musical friends, Adrienne and Alex, for our shared joy in music making. And Steve, for showing me the joy in a simple life and beautiful music.

To the Victoria performing arts community and Fierce Brosnan, our local legend.

To my fellow fibre friends and crafters: Leise, Wes, Ashley, Sabrina, Sarah. To the graduate student society for continuing to connect us across departments.

To the international community, and my international friends—Marcela, Bernardo, Danny, Victor, Mehrab, and many others.

To Erica. To my students and everyone working with outreach here. I love being able to pass on our knowledge to the wider world.

To my TEP friends—I hope you all continue to do well.

To all of my grade school math nerds—Stanley, Alex, Rick, Andrew. I enjoyed all of our adventures together, appreciate helping myself bloom in curiosity and exploration, and keep on math-ing!

To my past advisors, James who has continued to support me long after our paths diverged, David and Jennifer for guiding my first research project. To Wayne for showing us the joy of astronomy and outreach. To my mentor, Ebtihal.

To my past roommates, Matthew, Josh, and Bryn, for putting up with my chaos and our shared time together.

To my long-time friends—Nikola, Eric, Mikey, Anthony, Anya, Kaia, Alyssa, Aaliyah, Cameron—may we continue to stay in touch.

To my parents for their continuous support throughout this project. To my grandparents for always being there. To Nolan and Olivia, always a joy to see each other. To Bridget and Gretchen. To my extended family. And to my siblings for always being a source of joy.

To Arya. To all of my furry friends of friends—Nano, Pluto, Hobbs, Penelope, Tochka, Camar, Loki, and Hermes.

To the stars and the moon, for your enduring beauty, continuing to inspire me and posing unending questions about our natural world.

To the land of Victoria, and its historical caretakers. To the waters and beautiful trees, the ocean waves, rocks and hills and jagged coastlines. To the rich, enveloping forests and rust-red arbutus tress, scraggly Garry oaks and Camus flowers. I could not imagine a more beautiful place to study and to always remind my place in the world.

In the land of my birth, there is a hill. And upon that hill is a rock where I have sat and watched a changing world. This rock will not change—I would say. I'll pass from this Earth but the rock will remain, ever watchful of the land. But my feet kicked the dirt beneath me. Were the granules of soil not once like this rock? Is the rock not a collection of their multitudes? … And is my path so different? Neither destroyed nor created, but a collection of dust meant to observe a changing world and then return to dust.

—Joe Fisher, *Midnight Burger*

1. Introduction

Dwarf galaxies host, in many ways, the most extreme galactic environments in the universe. These galaxies are typically defined to be fainter than the Large Magellanic Cloud (LMC), with $M_V \gtrsim -18$ or similarly $M_\star \lesssim 10^9 M_\odot$ (e.g., McConnachie 2012; Bullock & Boylan-Kolchin 2017). Because the galaxy luminosity function increases towards fainter objects, dwarfs are the most numerous of galaxies (e.g., Blanton et al. 2005; Mao et al. 2021). Dwarf galaxies are also highly *dark-matter dominated*, with mass to light ratios which may exceed 1000 $M_\odot/L_\odot$ (implying $\sim$ 1000 times more dark matter than stellar mass, e.g., Simon & Geha 2007; Hayashi et al. 2023).

Except for the Magellanic Clouds, most dwarf galaxy satellites of the Milky Way (MW) are *quenched*, with little to no recent star formation (e.g., Weisz et al. 2014). Indeed, most faint MW satellites contain stellar populations which are *relics* from the early universe, consisting of many of the oldest and most metal-poor stars known (Simon 2019). Understanding the properties of dwarf galaxies thus has implications across astronomy, from small-scale cosmological structure formation to the origins of the first stars.

In this Chapter, we first describe the general observed properties of local dwarf galaxies. Next, we summarize our understanding of the cosmological origin of dwarf galaxies. We later review recent advancements and pending questions concerning dwarf galaxies, and introduce the puzzle posed by the extended stellar density profiles of Sculptor and Ursa Minor. Then, we discuss the theory of tidal evolution. We end with a brief roadmap to the remainder of this dissertation.

1.1 Observations of dwarf galaxies

Dwarf galaxies have long raised conundrums for theories of galaxy formation. The discovery of Fornax and Sculptor in 1938 (Shapley 1938)[1], with no known analogues at the time, already presented an enigma. H. Shapley presented these dwarfs as a new type of *stellar*

[1]Technically, the Large and Small Magellanic Clouds (LMC, SMC) are also classified as dwarf galaxies, but these were likely always known to humans at southern latitudes.

system resembling the Magellanic Clouds and globular clusters but did not attempt to speculate on their nature. While dwarf galaxies were soon understood to be galaxies based on the inferred luminosities and sizes, their exact nature remained unclear for decades (e.g., Hodge 1971; Gallagher & Wyse 1994).

The earliest spectroscopic work hinted that dwarf galaxies may contain substantial amounts of dark matter. From velocity dispersion measurements for dwarf spheroidal (dSph) galaxies, inferred mass-to-light ratios were at least 10 times larger than for globular clusters (e.g., Aaronson 1983; Aaronson & Olszewski 1987). While uncertain initially, these values were later corroborated with larger and more precise samples (e.g., Hargreaves et al. 1994). At the time, several theories were proposed to explain these unusually high mass-to-light ratios. Examples include: ongoing tidal disruption inflating inferred velocity dispersions (e.g., Kuhn & Miller 1989), the presence of massive central black holes (e.g., Strobel & Lake 1994), or modified theories of gravity (Milgrom 1995). Over time, a consensus developed where the high mass-to-light ratios of dwarf galaxies were due to the presence of a massive dark matter halo (e.g., Dekel & Silk 1986; Wechsler & Tinker 2018). Since then, the properties of dwarf galaxies have played an increasingly important role in our understanding of the clustering of dark matter on small scales (e.g., Bullock & Boylan-Kolchin 2017; Sales et al. 2022).

Today, a common definition for a (dwarf) galaxy is that of a gravitationally bound stellar system with dark matter.[2] In contrast, star clusters (such as globular clusters) have no clear evidence for dark matter. The boundary between these two classes blurs for faint, compact stellar associations. Systems with characteristics of both globular clusters and dwarf galaxies are known as "ambiguous" systems (e.g., Smith et al. 2024).

Dwarf galaxies span a large range of sizes, luminosities, and morphologies. Broadly, there are two morphological classes of dwarf galaxies, although additional types exist outside the Milky Way system. **Dwarf irregular galaxies** (dIrr) are defined by complex morphologies and recent star formation. Around the Milky Way, only the two brightest satellites, the Magellanic Clouds, are classified as dwarf irregulars. Fig. 1.1 shows the Large Magellanic Cloud (LMC), where most stars are in a rotationally-supported disk (seen nearly face-on) with a prominent bar. In contrast, **dwarf spheroidals (dSph)**[3] are old, approxi-

[2]Or, more generally, systems inconsistent with Newtonian dynamics of visible matter alone (Willman & Strader 2012).

[3]While formally the dwarf galaxy names we discuss contain "dwarf spheroidal" (dSph), e.g., Sculptor dSph, we omit this suffix for brevity. Additionally, the 12 classical dwarf satellites of our Galaxy are (in order of decreasing luminosity) Sagittarius, Fornax, Leo I, Sculptor, Antlia II, Leo II, Carina, Draco, Ursa Minor, Canes Venatici I, Sextans I, and Crater II. The only post-digital sky survey additions are Antlia II, Crater II,

mately spheroidal, dispersion-supported, non-star-forming, and gas-poor systems. These galaxies can be further divided into classical and ultra-faint dwarfs. **Classical dSphs** have $M_V \lesssim -7.7$ or $M_\star \gtrsim 10^5\,\mathrm{M}_\odot$. All Milky Way dSph galaxies discovered before digital sky surveys are classical dwarfs, and these systems remain among the best studied. **Ultra-faint dwarf galaxies**, fainter than $M_V \approx -7.7$, have minuscule stellar masses and very metal-poor stellar populations (see the review by Simon 2019). Altogether, known dwarf galaxies span more than 15 absolute magnitudes, or over 6 decades in stellar mass.

Most well-studied dwarf galaxies lie in the vicinity of the Milky Way, the *Local Group* of galaxies. The Local Group is defined as the group consisting of galaxies within $\sim$ 1 Mpc from the MW-Andromeda centre (e.g., McConnachie 2012; and references therein). Today, we know that the Local Group is teeming with dwarfs, many of which are satellites of either the MW or Andromeda (M31). Fig. 1.2 shows the MW satellite system, including dwarf galaxies, globular clusters, and ambiguous systems. This nearby population of dwarf galaxies is amenable to resolved studies aimed at investigating their detailed history and structure.

1.2 Dwarf galaxies in a cosmological context

We only understand a fraction of the universe's composition. The leading theory of cosmology, Lambda Cold Dark Matter (ΛCDM), posits that the universe is composed of about 68% dark energy (Λ), 27% dark matter (DM), and 5% baryons[6] (Planck Collaboration et al. 2020). While the composition of dark matter and dark energy remains elusive, we know their general properties. Dark energy drives the acceleration of the expansion of the universe on large scales. We do not discuss dark energy here—it does not substantially affect the Local Group today. Dark matter, instead, makes up the vast majority of mass in galaxies. Typically, galaxies have baryonic-to-dark matter ratios of between 1:5 to beyond 1:1000 for faint dwarf galaxies (e.g., Hayashi et al. 2023).

In ΛCDM, dark matter is assumed to interact only gravitationally. Light and matter pass through dark matter unimpeded—in this sense, dark matter is transparent. Dark matter is also assumed to be *cold*, i.e., with typical velocities much smaller than the speed of light in

and Canes Venatici I.

[4]Created with hips2fits (https://alasky.cds.unistra.fr/hips-image-services/hips2fits), a service provided by CDS.

[5]https://www.esa.int/ESA_Multimedia/Images/2018/04/Gaia_s_sky_in_colour2

[6]In a classic astronomer's corruption of jargon, *Baryons* here means baryons and leptons, i.e., protons, neutrons, and electrons.

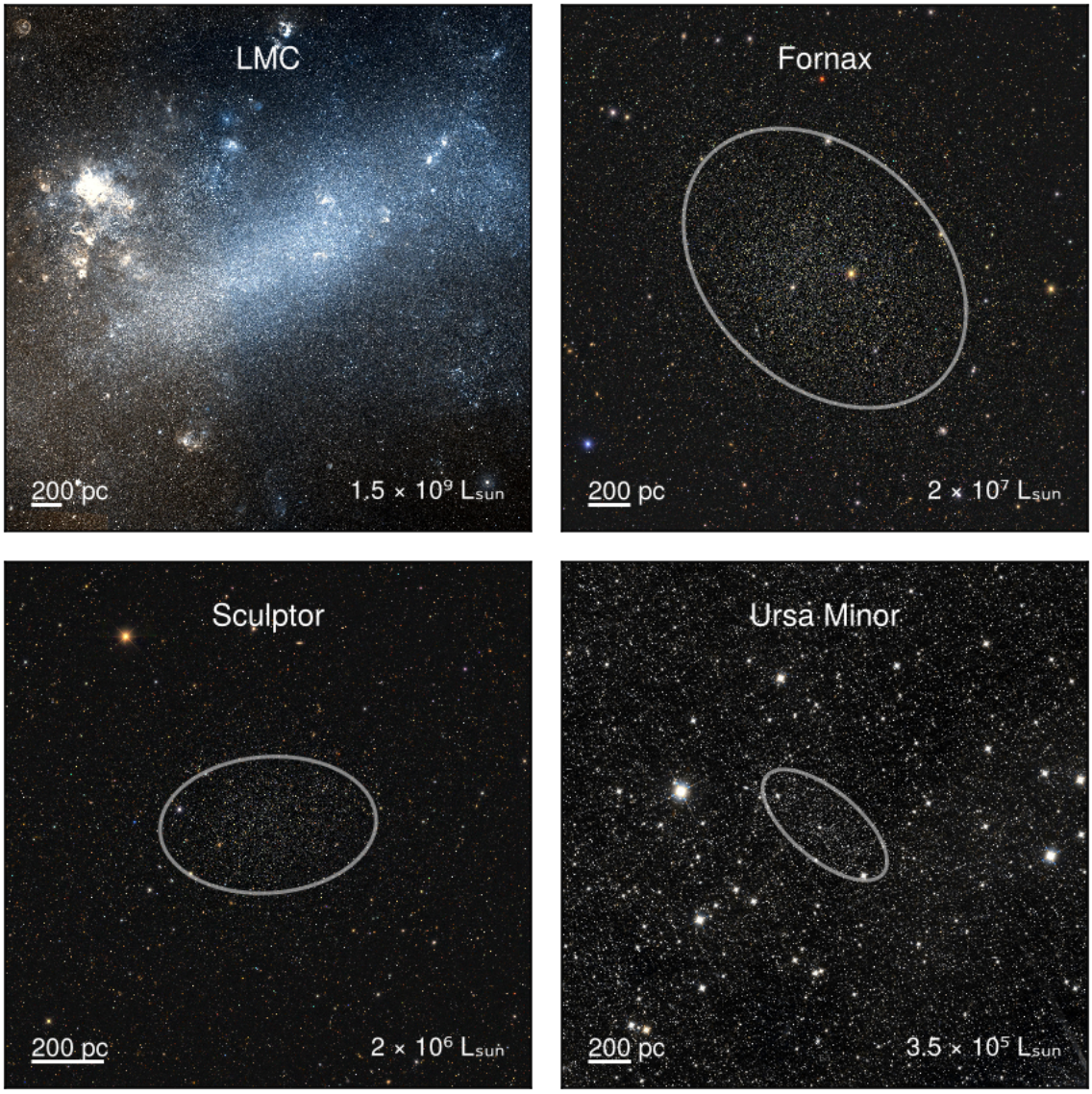

Figure 1.1: Images of the LMC (Digitized Sky Survey II, Lasker et al. 1996), Fornax (DES DR2, Abbott et al. 2021), Sculptor (DES DR2), and Ursa Minor (UNWISE, Lang 2014; Meisner et al. 2017a,b; with *Gaia* point sources overplotted).[4] The grey ellipse represents the half-light radius for the three dwarf spheroidals, and the luminosity is derived from the absolute V-band magnitude of each galaxy.

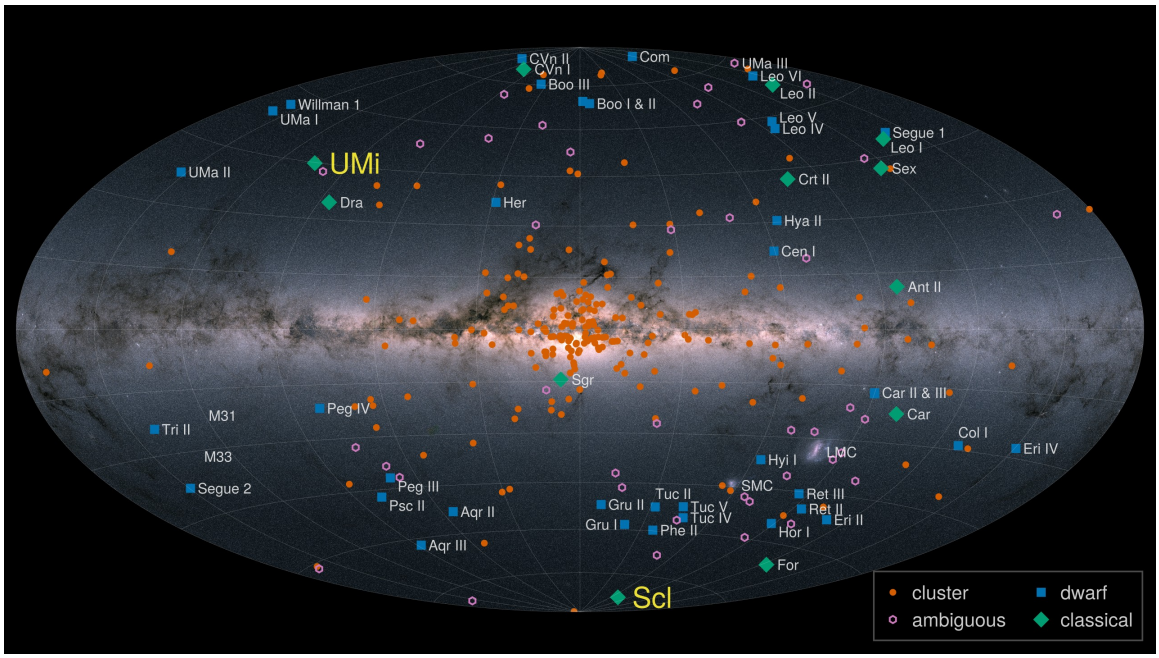

Figure 1.2: The location of MW satellites on the sky. We label the classical dwarf galaxies (green diamonds), fainter dwarfs (blue squares), globular clusters (orange circles), and ambiguous systems (pink open hexagons). Globular clusters are more centrally concentrated, but dwarf galaxies are preferentially found away from the MW disk. Sculptor and Ursa Minor are highlighted as two dwarfs we study later. The background image is from ESA/Gaia/DPAC.[5] Dwarf galaxies (confirmed), globular clusters, and ambiguous systems are from the Pace (2024) catalogue (version 1.0.3).

the early universe. If dark matter is cold, then it should condense on all scales, from the size of galaxy clusters to smaller than the faintest dwarf galaxies. Implications of dark matter properties include cosmological structure, galaxy formation, and galaxy interactions.

1.2.1 Structure formation in ΛCDM

The very early universe was almost featureless. Our earliest observations of the universe stem from the cosmic microwave background (CMB)—displaying a nearly uniform, isotropic blackbody emission (e.g., Ryden 2016). But tiny perturbations in the CMB, temperature fluctuations of 1 part in 100,000, reveal the underlying seeds of large-scale cosmological structure. In an expanding universe, gravitational instability makes CDM overdensities grow and collapse hierarchically onto larger structures. Initially, baryonic matter was coupled to radiation and resisted collapse. Dark matter, only influenced by gravity, freely collapsed into the first structures. Mass perturbations sufficiently small and overdense become self-gravitating structures, known as *halos* (e.g., Bovy in press 2026). After recombination, where electrons combined with atomic nuclei to form atoms, baryons decoupled from radiation and fell into dark matter halos, where they condensed at the centre through radiative energy losses. The densest pockets of baryons later formed the first stars and galaxies.

Dark matter halos and their associated galaxies rarely evolve in isolation. Instead, ΛCDM structure formation is *hierarchical*. Small dark matter halos collapse first and hierarchically merge into progressively larger halos (e.g., White & Rees 1978; Blumenthal et al. 1984; White & Frenk 1991). Hierarchical assembly is evident through the large-scale structure of the universe, remnants of past mergers within the Milky Way, and tidal disruption of dwarf galaxies and their streams around nearby galaxies.

Small-scale structure formation is sensitive to deviations from ΛCDM (e.g., Bechtol et al. 2022). One key prediction of ΛCDM is that mass perturbations are expected to exist on all scales, and are largest on the smallest scales, so we would expect the formation of halos on all scales. Many alternative models, such as warm dark matter, may smooth out small-scale features and reduce the abundance of small halos or change their structure (e.g., Lovell et al. 2014). Dwarf galaxies, which occupy the smallest dark matter halos capable of hosting a luminous component, are promising probes into the behaviour of dark matter on small scales.

1.2.2 The structure of cold dark matter halos

In ΛCDM cosmological simulations, dark matter halos are remarkably self-similar. Navarro et al. (1996b, 1997) observe that the spherically-averaged density profiles $\rho(r)$ are universally well described by a two-parameter law,

$$\rho/\rho_s = \frac{1}{(r/r_s)(1+r/r_s)^2}, \tag{1.1}$$

where r_s is a scale radius and ρ_s a scale density. This profile, known by the author's initials NFW, has shown remarkable success at describing ΛCDM halos across several orders of magnitude in mass. NFW profiles are *cuspy*, where the density rises like $\rho \sim 1/r$ at small radii $r \ll r_s$. The steepness of the density profile increases gradually with radius, and at large radii the density falls off like $\rho \sim 1/r^3$. The solid blue curve in Fig. 1.3 shows an example NFW halo.

The total mass of an NFW profile formally diverges, so halo masses are conventionally defined using an overdensity criterion. The virial mass, M_{200}, is defined as the mass within a radius, r_{200}, containing a mean enclosed density 200 times[7] the critical density of the universe:

$$M_{200} = 200\,\frac{4\pi}{3}\,r_{200}^3\,\rho_{\rm crit}, \qquad \text{where} \quad \rho_{\rm crit}(z) = 3H(z)^2/8\pi G, \tag{1.2}$$

and $H(z)$ is the Hubble constant, which depends on redshift. Another way of characterizing NFW halos is through the concentration parameter, $c = r_{200}/r_s$, which describes how the characteristic radial scale of the halo compares to the virial radius. Using this parameter, the scale density is a function of c alone, $\rho_s = (200/3)\,\rho_{\rm crit} c^3/[\log(1+c) - c/(1+c)]$ (Navarro et al. 1996b).

An equivalent, alternative characterization of NFW halos uses their circular velocity profiles. The circular velocity, $\mathrm{v_{circ}}(r) = \sqrt{GM(r)/r}$, reaches a maximum $\mathrm{v_{max}}$ at radius $r_{\rm max} \approx 2.16258\,r_s$. $\mathrm{v_{max}}$ and $r_{\rm max}$, like M_{200} and c, fully specify an NFW halo.

The two parameters of an NFW profile are not independent. Lower-mass dark matter halos typically collapse earlier, when the universe was denser. As a result, low mass subhalos tend to be more concentrated (e.g., Navarro et al. 1997). The relationship between M_{200} and c, or the mass-concentration relation, describes the mean trend of concentration with mass or, equivalently, the dependence of $\mathrm{v_{max}}$ on $r_{\rm max}$ (e.g., Bullock et al. 2001; Ludlow

[7]For the collapse of a uniform spherical density, the virialized overdensity would be $\Delta = 18\pi^2 \approx 178$ for a critical universe $\Omega_m = 1$. This is commonly rounded to $\Delta = 200$. While this parameter may be closer to $\Delta \approx 100$ for our universe, Δ also increases with redshift (see, e.g., eq. 6 from Bryan & Norman 1998).

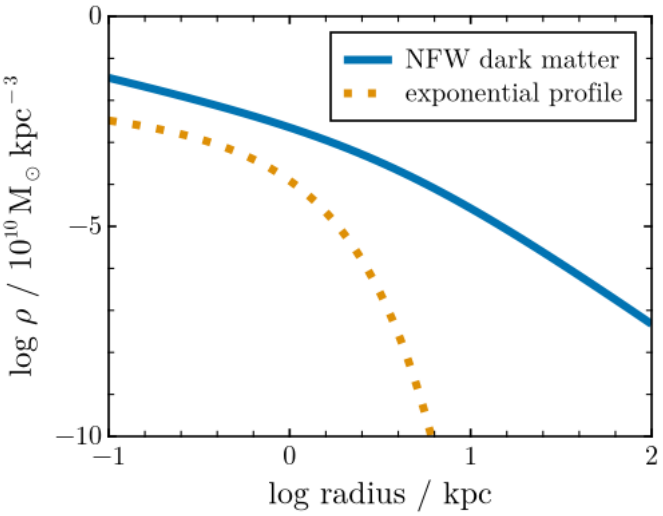

Figure 1.3: Density profiles in log 3D density versus log 3D radius for stars and dark matter in a Fornax-like galaxy. The dark matter is more extended and massive than the star across the entire galaxy. This galaxy has a stellar mass $M_\star \approx 2.5 \times 10^7\,\mathrm{M}_\odot$ with half-light radius 0.65 kpc following a projected exponential surface brightness profile (deprojected into 3D density). The corresponding cosmological-mean halo has $\mathrm{v}_{\mathrm{max}} = 40\,\mathrm{kpc}$ and $r_{\mathrm{max}} = 8\,\mathrm{kpc}$, or $M_{200} = 1 \times 10^{10}\,\mathrm{M}_\odot$ and $c = 12.5$.

et al. 2014). The left panel of Fig. 1.4 illustrates the present-day mass-concentration from Ludlow et al. (2016). While concentration tends to decrease with increasing mass, the relation has substantial scatter. Other parameters, such as the halo spin or shape, may affect the scatter of the mass-concentration relation, but their effect is typically expected to be small (Navarro et al. 2010; Di Cintio et al. 2013; Dutton & Macciò 2014).

1.2.3 Galaxy formation in ΛCDM

The observed abundance of galaxies may be compared with the abundance of ΛCDM halos to derive constraints regarding which galaxies inhabit which halos. One simple technique, dubbed "abundance matching," assumes a tight relation between the stellar mass of a galaxy and the mass of the halo it inhabits (Li & White 2009; Moster et al. 2013).

The right-hand panel of Fig. 1.4 shows the stellar mass versus halo mass relation (SMHM, with halo mass represented by $\mathrm{v}_{\mathrm{max}}$) predicted by ΛCDM cosmological hydrodynamical simulations of Local Group analogues from the APOSTLE project (Sawala et al. 2016).[8] While

[8] APOSTLE simulated Local Group analogues in a ΛCDM cosmological context with the hydrodynamical setup from the EAGLE simulations (Crain et al. 2015; Schaye et al. 2015).

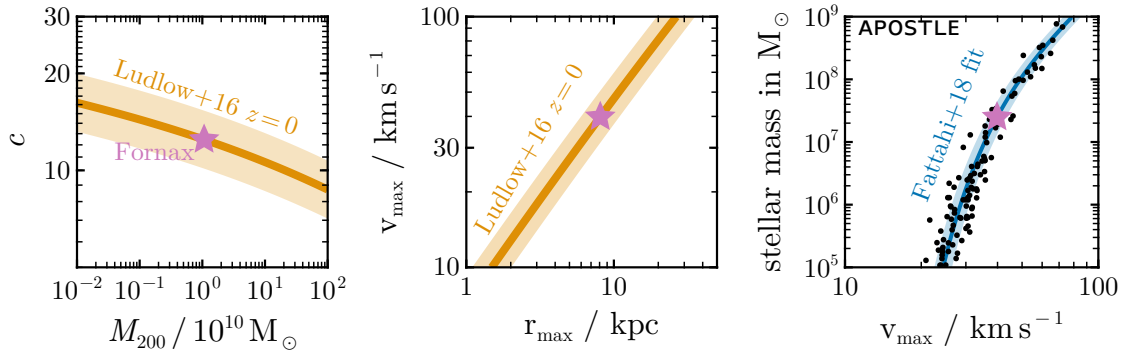

Figure 1.4: **Left** The NFW halo concentration $c = r_{200}/r_s$ as a function of virial mass M_{200}. The solid line with 1-σ shaded region is the mass-concentration relation from Ludlow et al. (2016) for $z = 0$. **Middle**: Equivalent to the left except in terms of the halo maximum circular velocity, v_{max}, and radius where the velocity is maximized, r_{max}. **Right** Stellar mass (top) as a function of maximum circular velocity. The solid line with the 1-σ shaded region is the relation from Fattahi et al. (2018) with scatter points simulated central galaxies from APOSTLE in Fattahi et al. (2018). The pink star illustrates the location of the Fornax galaxy, whose density profiles are shown in Fig. 1.3.

there is some scatter, the range of predicted v_{max} is fairly narrow across ~ 4 decades in stellar mass. This figure indicates that the SMHM relation becomes increasingly steep in the dwarf galaxy regime—many dwarf galaxies are formed in halos of similar mass. Because lower mass galaxies have shallower potential wells, the energetic output of evolving stars and possibly supermassive black holes (i.e., "feedback") becomes more effective at removing gas. Reionization additionally suppresses late star formation in the faintest galaxies. As a result, the resulting stellar mass of a dwarf galaxy is highly sensitive to the details of halo assembly and evolution.

In ΛCDM galaxy formation, the majority of mass in a dwarf galaxy comes from the extended dark matter halo. Fig. 1.3 shows an example exponential stellar component for the Fornax dwarf galaxy with its surrounding dark matter NFW halo (with parameters matching Ludlow et al. 2016; Fattahi et al. 2018). Where the stars are densest, the dark matter remains nearly an order of magnitude higher in density. Stars make a small contribution to the gravitational structure of dwarf galaxies—indeed, stars are reasonably approximated as tracer particles of the underlying dark matter halo. In addition, the stellar component is typically confined to the central regions of the dark matter halo.

Several factors affect the SMHM trend, including environment, assembly history, tidal

effects, and the details of galaxy formation. For example, effects like ram-pressure stripping (removal of gas in the dwarf galaxy due to pressure from the host's circumgalactic medium) and tidal removal of gas cause star formation to quench (e.g., Christensen et al. 2024). Additionally, the time of formation (relative to reionization) can influence the resulting stellar content (Kim et al. 2024). Finally, Galactic tides reduce both the dark matter and stellar mass but in different amounts, adding additional scatter to the SMHM trend for satellites (e.g., Peñarrubia et al. 2008; Fattahi et al. 2018). Understanding the effects of tides on Local Group dwarf galaxies may help us understand where and how these galaxies formed in a cosmological context.

1.2.4 Challenges and questions concerning dwarf galaxies

Observations of dwarf galaxies have been the origin of several disputes or *small-scale* problems for ΛCDM (see reviews by Bullock & Boylan-Kolchin 2017; Sales et al. 2022). For example, the mismatch between the number of dwarf galaxies and the predicted abundance of ΛCDM halos has been known as the *missing satellites problem*. Additionally, several observations suggest that some dwarf galaxies, although not all, possess dark matter "cores," (e.g., Moore 1994; Adams et al. 2014; Oh et al. 2015; Walker & Peñarrubia 2011; Read et al. 2019), contrary to the expectation from ΛCDM of "cuspy" inner dark matter profiles (Navarro et al. 1996b, 1997). As a result, alternative forms of dark matter have been advocated as solutions, such as Warm or Self-Interacting Dark Matter.

However, some of these tensions have eased as a result of improved understanding of baryonic physics. For example, recent hydrodynamic simulations, in particular, have shown that strong feedback can produce dark matter cores (e.g., Navarro et al. 1996a; Tollet et al. (2016); Fitts et al. 2017; Benítez-Llambay et al. 2019; Orkney et al. 2021). Several open questions remain, concerning, e.g., the nearly planar distribution of luminous Milky Way satellites, the details of the sizes and rotation curves of dwarf galaxies, and the existence and nature of stellar halos in dwarf galaxies (e.g., Sales et al. 2022). Altogether, the numerous past and ongoing challenges for ΛCDM in the dwarf galaxy regime illustrate the opportunity for dwarf galaxies to our the understanding of galaxy formation and dark matter physics.

1.3 The structure of nearby dwarf galaxies

1.3.1 The *Gaia* mission

Since Local Group dwarfs are nearby, they are resolved into individual stars, and therefore, we can study these galaxies on a star-by-star basis. As a result, it is possible to measure

the 3D velocity and position of a star if we can measure its position, distance, line-of-sight (LOS) velocity, and proper motion. Unfortunately, determining distances and full 3D velocities is challenging. The most direct measurement of distance, the parallax, requires precise tracking of a star's sky position across a year. And while line-of-sight (LOS) velocities are relatively easily determined from spectroscopy, tangential velocities, derived from proper motions and distances, are much more challenging. Typically, measuring proper motions requires precise ($\ll$ arcsecond) determinations of small changes in a star's position over baselines of years to decades. The full 6D position and velocity information for stars has, until recently, been known for only a handful of stars.

Launched in 2013, *Gaia* is a space-based, all-sky survey telescope situated at the Sun-Earth L2 Lagrange point (Gaia Collaboration et al. 2016). *Gaia* has redefined astrometry, providing photometry, positions, proper motions, and parallaxes for over 1 billion stars (Gaia Collaboration et al. 2021). While *Gaia* completed its space-based mission in 2025, two further data releases are still expected.

Determining absolute parallax measurement is facilitated by the observation that stars in different regions of the sky are affected by parallax motion with different phases. By imaging two regions separated by 106.5 degrees on the same focal plane, *Gaia* measures changes in the relative positions of stars across small and large angles. Combining measurements from multiple epochs across several years, an absolute all-sky reference frame is derived from which parallax and proper motions are calculated. In addition to astrometry, *Gaia* measures photometry in the wide G band (330–1050nm) and colours from the blue photometer (BP, 330–680 nm) and red photometer (RP, 640–1050 nm). *Gaia* additionally provides low-resolution BP-RP spectra and radial velocity measurements of bright stars (of magnitudes $G_{\rm RVS} < 16$, Gaia Collaboration et al. 2016). For our work, *Gaia*'s most relevant measurements are G magnitude, $G_{\rm BP} - G_{\rm RP}$ colour, (α, δ) position, and $(\mu_{\alpha*}, \mu_\delta)$ proper motions.[9]

1.3.2 *Gaia*'s impact on Milky Way studies

Gaia has revolutionized our understanding of Milky Way structure. For example, the 6D dynamical measurements and metallicities of MW stars led to the (re)discovery of past mergers or Milky Way building blocks like *Gaia*-Sausage Enceladus (e.g., Helmi et al. 2018; Belokurov et al. 2018; but see also Meza et al. 2005), out-of-equilibrium structures like the *Gaia* snail (e.g., Antoja et al. 2018), and dynamical effects of the Milky Way's spiral arms

[9]The proper motions μ_α and μ_δ are the apparent rates of change in right ascension, α, and declination, δ, typically in units of milli-arcsecond (mas) per year. $\mu_{\alpha*} = \mu_\alpha \cos\delta$ corrects for projection effects in α.

and the bar in the solar neighbourhood (Hunt & Vasiliev 2025; and references therein). In the Milky Way halo, *Gaia* has helped find and constrain numerous stellar streams (Ibata et al. 2019; Bonaca & Price-Whelan 2025). Altogether, *Gaia* has revealed the hierarchical formation and complex, evolving structure of our own Galaxy.

For Milky Way satellites, *Gaia* has improved orbital analysis and facilitated robust stellar membership determinations. Before *Gaia*, few galaxies had precisely measured proper motions (e.g., using the Hubble Space Telescope, Piatek et al. 2005; Sohn et al. 2017). *Gaia* allowed for some of the first systematic and precise determinations of Milky Way satellite proper motions (Gaia Collaboration et al. 2018; Simon 2018; Fritz et al. 2018; Pace & Li 2019; McConnachie & Venn 2020a). While the proper motion uncertainty of a typical dwarf member star is often large, by combining the proper motions of 100s or 1000s of stars from *Gaia*, precise average proper motion measurements can be determined, sometimes only limited by *Gaia*'s systematic error floor (e.g., McConnachie & Venn 2020a). Proper motions have thus ushered in a new era for MW satellite dynamical studies, where we can derive precise orbits for any satellite, assuming a given MW potential. In addition, *Gaia* helps establish membership by filtering contaminating MW foreground stars. By measuring parallaxes and/or proper motions, many more background and foreground stars can be classified as non-members (e.g., Battaglia et al. 2022; Jensen et al. 2024).

1.3.3 Dwarf galaxy light profiles

Projected luminosity/stellar density profiles efficiently characterize the radial structure of a galaxy. At its most basic, light profiles synthesize properties such as the shape, size, and orientation of a dwarf galaxy. In addition, the details of a stellar density profile can help interpret a galaxy's assembly and dynamical history (e.g., Peñarrubia et al. 2009; Lee et al. 2018; Querci et al. 2025). Note that for resolved galaxies, these profiles are expressed in stellar count densities instead of surface brightness.

Four different surface density laws are frequently used to parameterize dwarf galaxy profiles: Exponential, Plummer, King, or Sérsic profiles (e.g., Muñoz et al. 2018). The exponential profile is perhaps the simplest, defined in terms of the central surface density, Σ_0, and projected scale radius, R_s:

$$\Sigma_{\rm exp} = \Sigma_0 \exp(-R/R_s). \tag{1.3}$$

This profile is also often applied to the radial light distribution of galaxy disks (de Vaucouleurs 1959; Freeman 1970; Kent 1985).

To fit globular cluster density profiles, Plummer (1911) proposed a profile based on a self-gravitating polytrope,[10]

$$\Sigma_{\rm Pl} = \frac{\Sigma_0}{(1 + (R/R_h)^2)^2}, \tag{1.4}$$

where Σ_0 is the central surface density and R_h is the projected half-light radius. Now mostly superseded by the King profile for globular clusters, the Plummer model is still a good fit to many dwarf spheroidals (e.g., Moskowitz & Walker 2020).

The King (1962) profile, also a fit to globular clusters, is also used to describe dwarf galaxies, more so in older literature. Using three parameters, a core radius R_c, a truncation radius R_t, and a characteristic density, Σ_0, the King profile may be written as

$$\Sigma_{\rm K} = \Sigma_0 \left(\frac{1}{\sqrt{1 + (R/R_c)^2}} - \frac{1}{\sqrt{1 + (R_t/R_c)^2}} \right); \qquad \text{for } R < R_t \tag{1.5}$$

and $\Sigma_{\rm K} = 0$ for $R \geq R_t$. In much of the older literature, R_t was interpreted as a "tidal radius," after an analogous interpretation for globular clusters (e.g., Hodge 1961; Irwin & Hatzidimitriou 1995).

Finally, the Sérsic (1963) profile represents a generalization of an exponential profile and describes most dwarf galaxy light profiles well. Typically parameterized in terms of a half-light radius R_h, the density at half-light radius Σ_h, and a Sérsic index n, the profile's equation is

$$\Sigma_{\rm S} = \Sigma_h \exp\left[-b_n \left((R/R_h)^{1/n} - 1 \right) \right] \tag{1.6}$$

where the coefficient b_n solves $\Gamma(2n) = 2\gamma(2n, b_n)$ with Γ the Gamma function and γ the lower incomplete gamma function (Graham & Driver 2005). A Sérsic profile with $n = 1$ is equivalent to an exponential profile, while $n = 4$ recovers de Vaucouleurs's (1948) profile for elliptical galaxies. Although a Sérsic profile is less commonly applied to dwarf galaxies, Muñoz et al. (2018) advocate for the Sérsic profile since the added flexibility allows more profiles to be fit with a single law.

While there are no clear theoretical preferences for any of these profiles, exponential density profiles have been commonly used for dwarf spheroidal galaxies. Faber & Lin (1983) were among the first to demonstrate that an exponential law is a reasonable empirical fit, theorizing that dwarf spheroidals may have evolved from exponential disk galaxies and maintained a similar light profile. Later, Read & Gilmore (2005) showed that exponential profiles may originate from mass loss during the evolution of dwarf galaxies. Tides are a possible mechanism for this transformation—the *tidal stirring hypothesis* (Mayer et al.

[10] where density and pressure are assumed to be related by a power law

2001; Klimentowski et al. 2009). However, the theoretical origin of exponential disks is also unknown.[11]

Many subsequent photometric studies of dwarf spheroidal galaxies have used exponential fits, finding that exponential and King profiles both provide good descriptions in many cases (Binggeli et al. 1984; Mateo 1998; McConnachie & Irwin 2006; Cicuéndez et al. 2018). More recently, Moskowitz & Walker (2020) fit instead generalized Plummer profiles, but most of their fits would be consistent with a single-component exponential.[12] As a result, it has become conventional to assume an exponential density profile to describe dwarf galaxies in theoretical or observational modelling (e.g., Kowalczyk et al. 2013; Martin et al. 2016; McConnachie & Venn 2020a; Battaglia et al. 2022).

Dwarf galaxies outside the Local Group commonly follow exponential profiles, but sometimes with modifications. For example, many extragalactic dwarf elliptical, blue compact dwarf, and irregular dwarf galaxies are better described with an exponential profile to which a central cusp or nuclear region is added (Caldwell & Bothun 1987; Noeske et al. 2003). On the other hand, some studies find an inner density decrement relative to exponentials (e.g., Caldwell et al. 1992; Makarov et al. 2012), or that dwarfs are better fit by two nested exponentials (e.g., Aparicio et al. 1997; Graham & Guzmán 2003; Hunter & Elmegreen 2006; Lee et al. 2018). It is unclear how these conclusions apply to the dwarf spheroidals of the Local Group.

Altogether, while there is some variation in the density profiles of dwarf galaxies, an exponential is an excellent first-order approximation. Typically, deviations from exponentials are in the direction of a steeper outer cutoff or changes to the inner slope of a dwarf galaxy (due, for example, to a nuclear star cluster). Flattened density profiles in the outer regions are more unusual. Explaining in detail the origin, similarity, and diversity of dwarf galaxy density profiles is an open question for theories of dwarf galaxy formation and evolution.

1.3.4 The extended light profiles of Sculptor and Ursa Minor: Hints of tidal signatures?

Sculptor (Scl) and Ursa Minor (UMi) appear to be typical dwarf spheroidal galaxies at first glance (see Fig. 1.1). Tables 1.1, 1.2 describe the structural parameters of each galaxy.

[11] While studied for far longer, the exponential origin of disk galaxies is no better understood. Ideas range from scattering of stars (Elmegreen & Struck 2013; Wu et al. 2022) to angular momentum transport, to disk viscosity-driven radial gas flows (Lin & Pringle 1987; Wang & Lilly 2022) or spherical collapse (Freeman 1970).

[12] A single-component exponential profile is close to their "Steeper" profile in Moskowitz & Walker (2020) over the range of their data. However, most of their galaxies have little evidence to prefer the Steeper or Plummer density profile.

Sculptor, as the first discovered classical dSph, is even described as a "prototypical" dSph (e.g., McConnachie 2012).

However, many studies have speculated that Scl and UMi have been influenced by the Milky Way's tidal field. Already, Innanen & Papp (1979) found RR Lyrae candidate Scl members (from van Agt 1978) out to 180′ in an elongated distribution, speculating this to be tidal disruption. Later density profile determinations noted Scl's elongation and apparent outer density excess (Eskridge 1988; Irwin & Hatzidimitriou 1995; Walcher et al. 2003; Westfall et al. 2006; but see also Coleman et al. 2005). These studies often interpreted these features as evidence of tidal effects (e.g., Walcher et al. 2003) or sometimes a "halo"of stars surrounding the dwarf (Westfall et al. 2006).

UMi has attracted similar suspicions. Hargreaves et al. (1994) first detected a velocity gradient in UMi, suggestive of tidal disruption. Later, Martínez-Delgado et al. (2001) found stars far beyond the King-profile "tidal radius," aligned with UMi's elongation, consistent with tidally-stripping simulations in Gómez-Flechoso & Martínez-Delgado (2003). Palma et al. (2003) furthermore detected S-shaped isophotes and an extended population of "extratidal" stars.

Adding to the evidence, Sestito et al. (2023a,b) report a "kink" in the density profile of each galaxy. They spectroscopically follow up distant stars, finding members as far as 6 and 12 half-light radii from the centre of each dwarf. If these dwarfs had exponential profiles, like Fornax, then these far-outlying stars should be much rarer.

Sculptor and Ursa Minor are poorly described by an exponential profile. The left panel of Fig. 1.5 shows the density profiles of Sculptor, Ursa Minor, and Fornax (see Section 2 for details on how these profiles are measured). Compared to Fornax, both Sculptor and Ursa Minor show an excess of stars outside $\log R/R_h \approx 0.4$, implying densities which exceed 100 times the density of the exponential fit at large radii.

A goal of this work is to determine if tidal effects are indeed responsible for the extended outer light profiles of Sculptor and Ursa Minor. If tides cannot explain these features, these features may instead be due to an extended stellar "halo" or second component of the galaxy—suggestive of a complex star formation or assembly history.

1.4 Interpreting tidal signatures

The Local Group hosts several examples of ongoing tidal disruption. The Magellanic stream, a massive, gas-rich feature emanating from the Magellanic clouds, is believed to arise partially from the MW's tides (Putman et al. 1998; Diaz & Bekki 2012; D'Onghia & Fox 2016).

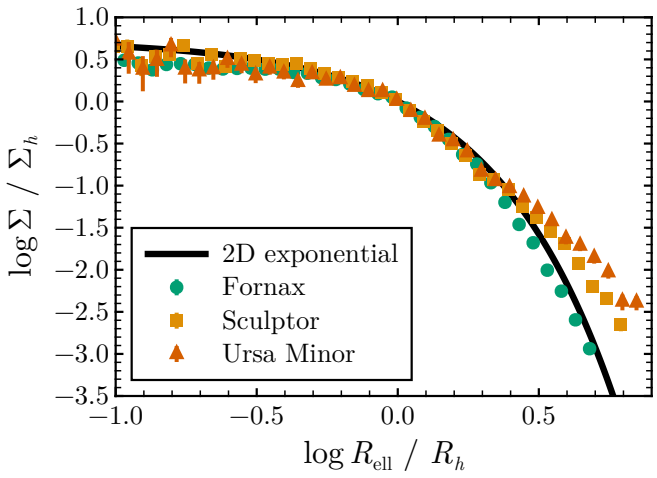

Figure 1.5: Surface density profiles of Sculptor (orange squares), Ursa Minor (red triangles), and Fornax (green circles) scaled to their half-light radius and the density at half-light radius (data described in Section 2). The solid black line is an exponential profile (Eq. 1.3). Scl and UMi show a clear excess over an exponential at large radii.

Other clear examples of tidal streams include the Sagittarius stream, the Andromeda Giant Southern stream, and the Tucana III stream (e.g., Ibata et al. 1994, 2001; Li et al. 2018). These examples illustrate that hierarchical accretion remains an active process. Interpreting such observations relies on simulations of tidal disruption.

Cosmological simulations struggle to resolve tidal effects on dwarfs. Since many dwarfs are near the resolution limit, they are vulnerable to artificial disruption (e.g., van den Bosch et al. 2018; Santos-Santos et al. 2025). To overcome numerical challenges, idealized simulations model a single subhalo in an analytic host potential, achieving excellent numerical convergence. For example, the simulations we describe later reach three times higher resolution than Aquarius (Springel et al. 2008) with 400 times fewer particles. Idealized simulations make numerous simplifications, neglecting mergers, cosmological context, mass assembly, and often baryonic physics (e.g., Hayashi et al. 2003; Bullock & Johnston 2005; Klimentowski et al. 2009; Ogiya et al. 2019). Cosmological simulations appear to predict that tidal disruption is more common than idealized simulations of MW dwarfs suggest, but the role of numerics and assumptions in this discrepancy are unclear (Panithanpaisal et al. 2021; Shipp et al. 2023; Riley et al. 2024). We shall use idealized simulations here to assess tidal effects after the satellite's infall into the MW halo.

Idealized simulations predict clear properties of tidally disrupting dwarf spheroidal galaxies. Tidally stripped stars form *tidal streams*—stellar tails with a bulk velocity gradient (e.g.,

Table 1.1: Observed properties of Sculptor. References are: (1) Muñoz et al. (2018, Sérsic fit), (2) Tran et al. (2022, RR lyrae distance), (3) Alan W. McConnachie and Venn (2020b), (4) Arroyo-Polonio et al. (2024).

parameter	value	Source
α	$15.0183 \pm 0.0012°$	1
δ	$-33.7186 \pm 0.0007°$	1
distance modulus	19.60 ± 0.05	2
distance	83.2 ± 2 kpc	2
$\mu_{\alpha*}$	$0.099 \pm 0.002 \pm 0.017$ mas yr^{-1}	3
μ_δ	$-0.160 \pm 0.002_{\rm stat} \pm 0.017_{\rm sys}$ mas yr^{-1}	3
LOS velocity	111.2 ± 0.3 km s^{-1}	4
σ_v	9.7 ± 0.2 km s^{-1}	4
R_h	9.79 ± 0.04 arcmin	1
ellipticity	0.37 ± 0.01	1
position angle	$94 \pm 1°$	1
M_V	-10.82 ± 0.14	1

Moore & Davis 1994; Johnston et al. 1995; Read et al. 2006). Most mass loss happens near pericentre, where tides are strongest. However, the central structure of a dwarf galaxy often remains undisturbed (Oh et al. 1995; Piatek & Pryor 1995). For instance, NFW halos are also found to be resilient to full tidal disruption (Errani & Peñarrubia 2020), but cored dark matter halos may disrupt fully and faster (e.g., Peñarrubia et al. 2010; Errani et al. 2023).

To first order, tidal mass loss peels away the outer layers of a dwarf galaxy in energy space. Drakos et al. (2020, 2022); Amorisco (2021) showed that tidal effects are nearly entirely described as the removal of particles above a truncation energy (see also Choi et al. 2009). Stücker et al. (2023) generalized this idea, creating a model for adiabatic tidal mass loss in an isotropic tidal field. Their model explains the resilience of NFW halos against full tidal disruption and the origin of well-defined "tidal tracks" (as observed in Peñarrubia et al. 2008; Green & van den Bosch 2019; Errani & Navarro 2021).

With precise orbital constraints and improved models of the Milky Way potential, recent studies have continued to probe the dynamical histories of individual dwarf galaxies. Battaglia et al. (2015); Borukhovetskaya et al. (2022a); Di Cintio et al. (2024) ran simulations tuned to Fornax, showing that this galaxy's stellar component or globular clusters are likely not affected by tides. Similarly, Borukhovetskaya et al. (2022b) analyzed Crater II,

Table 1.2: Observed properties of Ursa Minor. References are: (1) Muñoz et al. (2018, Sérsic fit), (2) Garofalo et al. (2025, RR lyrae distance), (3) Alan W. McConnachie and Venn (2020a), (4) Pace et al. (2020), average of MMT and Keck results with systematic uncertainty from Appendix B discussion.

parameter	value	Source
α	$227.2420 \pm 0.0045^{\circ}$	1
δ	$67.2221 \pm 0.0016^{\circ}$	1
distance modulus	19.23 ± 0.11	2
distance	70.1 ± 3.6 kpc	2
$\mu_{\alpha}*$	$-0.124 \pm 0.004 \pm 0.017$ mas yr^{-1}	3
μ_{δ}	$0.078 \pm 0.004_{\rm stat} \pm 0.017_{\rm sys}$ mas yr^{-1}	3
LOS velocity	$-245.9 \pm 0.3_{\rm stat} \pm 1_{\rm sys}$ km s^{-1}	4
σ_v	8.6 ± 0.3	4
R_h	11.62 ± 0.1 arcmin	1
ellipticity	0.55 ± 0.01	1
position angle	$50 \pm 1^{\circ}$	1
M_V	-9.03 ± 0.05	1

showing that the present-day structure is challenging to reconcile with NFW initial conditions and Galactic tides. Most relevantly, Iorio et al. (2019) also tailored simulations to Scl, finding weak Galactic tidal influence.

Building on this body of work, we will use idealized simulations to understand the severity of tidal effects on Sculptor and Ursa Minor.

1.4.1 Tidal and "break" radii

For a given orbit in a given potential, there are characteristic radii which help gauge the effects of tides on a dwarf galaxy.

The **Jacobi radius** represents the approximate radius where stars become unbound for a galaxy in a circular orbit around a host galaxy.[13] Calculated from an approximation of the location of the L_1 and L_2 Lagrange points, the Jacobi radius is where the mean density of the dwarf galaxy is roughly three times the mean interior density of the host galaxy at

[13]The Jacobi radius was derived at least as early as Laplace (1798). This radius also bears other names, such as the Hill radius (from Hill 1878). Likely only named after Jacobi for the Jacobi integral (Jacobi 1836).

pericentre, or

$$3\bar{\rho}_{\rm MW}(r_{\rm peri}) \approx \bar{\rho}_{\rm dwarf}(r_J), \tag{1.7}$$

(Binney & Tremaine 1987; eq. 7-84). If r_J is comparable to the visible extent of a galaxy, we should expect to find clear signs of tidal disturbance. While strictly valid for circular orbits, assuming $r_{\rm peri}$ for the host-dwarf distance works as most stars are lost during pericentric passages.

We also use the **break radius** as defined in Peñarrubia et al. (2009), marking the outermost radius within which the dwarf has been able to achieve equilibrium after pericentric passage in a highly eccentric orbit. The break radius $r_{\rm break}$ is proportional to the velocity dispersion, σ_v, and time elapsed since pericentre, Δt,

$$r_{\rm break} = C\,\sigma_v\,\Delta t \tag{1.8}$$

where the empirical constant is $C \approx 0.55$. $r_{\rm break}$ describes where the dynamical timescale becomes longer than the time since the perturbation, i.e., the radius within which the galaxy is dynamically relaxed.

1.4.2 A simple tidal simulation

To illustrate the effects of tides on an NFW halo due to a massive host, we consider a toy model. We evolve an N-body realization of an NFW subhalo with $r_{\rm max} = 5\,$kpc and $\mathrm{v}_{\rm max} = 27\,\mathrm{km\,s^{-1}}$ orbiting a static NFW host halo with $r_{\rm max} = 25\,$kpc and $\mathrm{v}_{\rm max} = 207.4\,\mathrm{km\,s^{-1}}$. These choices are motivated by the inferred structure and masses of dSphs and the Milky Way, respectively. We simulate the stellar component by assigning stellar weights to each particle based on the relative densities of the distribution functions in energy space (see Section 3.3.6). The stars initially follow a 2D exponential profile with a scale radius $R_s = 0.25\,$kpc and total mass $5 \times 10^5\,\mathrm{M}_\odot$, embedded within the inner dark matter halo. We start the model at apocentre on an orbit with a pericentre of 20 kpc and apocentre of 100 kpc. See Section 3 for a more detailed description of our numerical setup.

Fig. 1.6 illustrates the properties of this idealized simulation at the second apocentre, as seen from the centre of the host. The projected density of stars is relatively undisturbed and spherical in the centre, but becomes non-isotropic outside the break radius and shows nascent tidal tails. These tidally disturbed stars appear as an extended, outer density excess relative to the initial conditions. This excess appears just outside the break radius. The break radius also marks where the mean 3D radial velocity of the stars (with respect to the galaxy's centre) becomes non-zero — the galaxy is out of equilibrium outside $r_{\rm break}$.

To first order, the final density profile of this toy simulation indeed resembles the outer excess in Sculptor and Ursa Minor, motivating this thesis.

1.5 Thesis outline

The goal of this thesis is to review the evidence for an extended density profile in Ursa Minor and Sculptor, to assess the impact of tidal effects on each galaxy, and to discuss possible interpretations for the structure of these galaxies.

In Chapter 2, we describe how we compute observational density profiles following Jensen et al. (2024). In Chapter 3, we review our simulation methods. Next, we present our results for the tidal effects on Sculptor and Ursa Minor in Chapter 4. We discuss the implications of our results and end with a summary and outlook in Chapter 5.

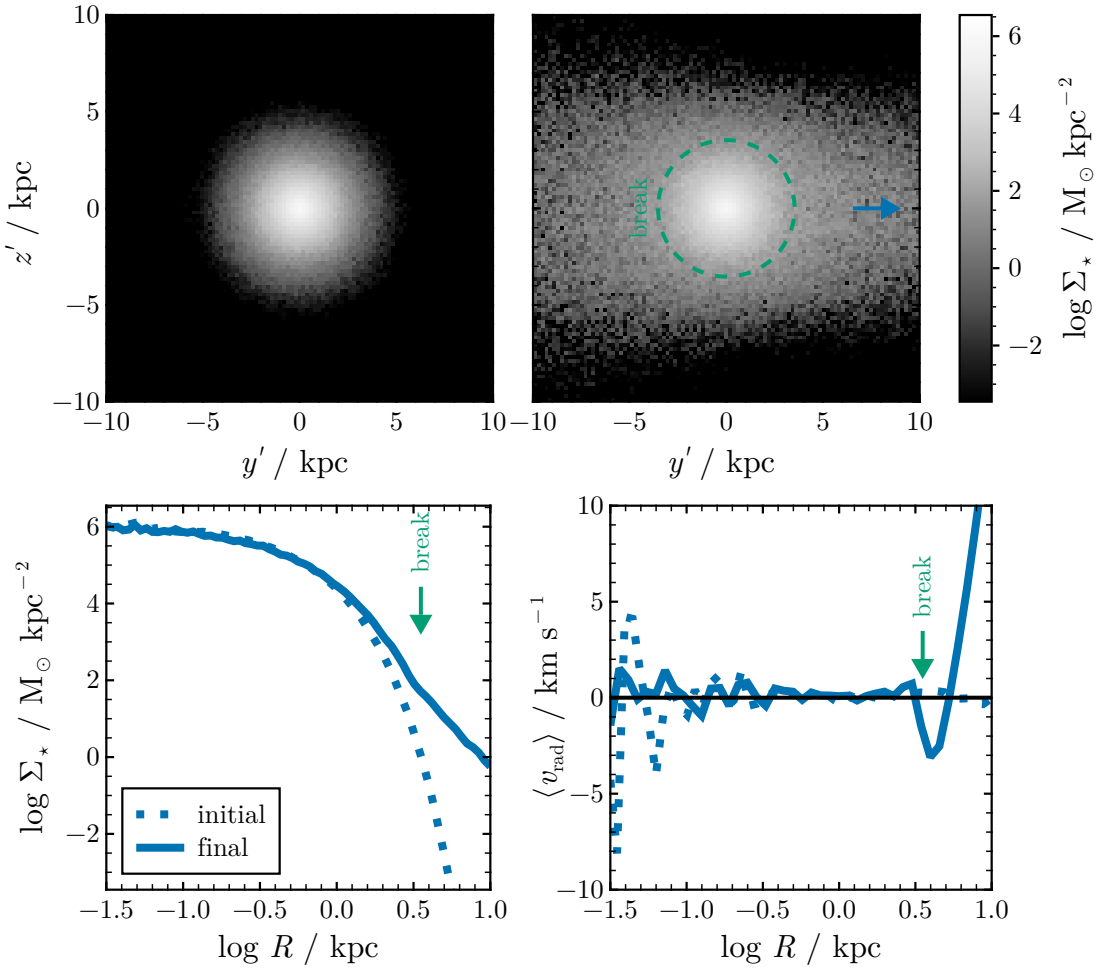

Figure 1.6: Example density and velocity distributions of an idealized dwarf galaxy model undergoing tidal stripping. **Top**: The projected 2D stellar density in the y'–z' plane for the initial (left) and final (right) simulation. y' is the direction of tangential orbital motion, and z' is the direction of orbital angular momentum, as measured from the centre of the host. The dashed green circle represents the break radius (Eq. 1.8) and the blue arrow points in the orbital direction. **Bottom left**: The projected stellar density profile for the initial (dotted) and final (solid) simulation snapshot. **Bottom right**: the mean 3D radial velocity (the dot product of relative position and velocity relative to dwarf centre) as a function of projected radius. The green arrow marks the break radius in both lower panels.

2. The Light Profiles of the Classical Dwarf Spheroidals

As discussed in Section 1.3.3, the projected luminosity/stellar mass density profile of dwarf galaxies is generally well-described by an exponential law (Eq. 1.3). A prototypical example is the Fornax dSph — well-fit by an exponential over 4.5 decades in surface density. On the other hand, Sculptor or Ursa Minor have profiles that deviate significantly from an exponential profile fitted to the inner regions, with a clear excess of stars/light in the outer regions. In this Chapter, we critically review the density profile of the MW classical dwarfs. This thesis concerns the origin of the outer deviations from exponential profiles, with a tidal interpretation explored in subsequent Chapters.

2.1 Satellite stellar membership with *Gaia*

Measuring the light profile of a resolved galaxy requires careful consideration of whether any given star belongs to the system or not. Without removing contamination from foreground/background sources, faint features may be lost in the noise or be of uncertain association. When only photometric data was available, the membership of stars was ascertained using the colour-magnitude diagram alone (e.g., matched filter methods like those used by Rockosi et al. 2002). Now that *Gaia* data are available, stellar parallax and proper motion are also available to improve membership assignment.

Here, we use the Jensen et al.'s (2024; hereafter J+24) membership probabilities from *Gaia* data. J+24 used a Bayesian framework incorporating proper motion (PM), colour-magnitude diagram (CMD), and spatial information to determine the probability that a given star belongs to the satellite or foreground/background. By accounting for PM in particular, J+24 produced low contamination samples of candidate member stars out to large distances from a dwarf galaxy. J+24 extended the algorithm presented in McConnachie & Venn (2020a,b) by additionally including a secondary, extended spatial component. J+24 detected candidate members out to ~10 half-light radii from the centres of some galaxies (R_h). Similar recent work includes Pace & Li (2019); Battaglia et al. (2022); Pace et al. (2022); Qi et al. (2022).

J+24's formulate membership through likelihoods, $\mathcal{L}$, representing the probability density that a star is consistent with either the foreground/background, $\mathcal{L}_{\rm bg}$, or the satellite galaxy, $\mathcal{L}_{\rm sat}$. In either case, the likelihoods are the product of a spatial, PM, and CMD component,

$$\mathcal{L} = \mathcal{L}_{\rm space}\ \mathcal{L}_{\rm PM}\ \mathcal{L}_{\rm CMD}. \tag{2.1}$$

For a satellite, the *spatial likelihood* is specified either as a one- or two-component elliptical exponential profile. A second exponential component is considered only when the preferred amplitude of the second component is non-zero. The *proper-motion likelihood* quantifies the agreement of a star's motion with the dwarf galaxy's systemic motion, accounting for observational uncertainties. The *CMD likelihood* measures the consistency of a star's *Gaia G* magnitude and $G_{\rm BP} - G_{\rm RP}$ colour with theoretical isochrones for the dwarf. For the background likelihoods, the spatial likelihood is a uniform distribution over the field, and the background CMD and PM likelihoods are constructed empirically from the stars in an annulus far from the satellite. Each likelihood is normalized as a probability density over the respective parameter space. Appendix A.3 discusses the details of quality cuts and the likelihood calculation (see also, McConnachie & Venn 2020a; Jensen et al. 2024).

The total likelihood is a mixture model of the satellite and background, weighted by the fraction of stars in the field belonging to the satellite, $f_{\rm sat}$:

$$\mathcal{L}_{\rm tot} = f_{\rm sat}\mathcal{L}_{\rm sat} + (1 - f_{\rm sat})\mathcal{L}_{\rm bg}. \tag{2.2}$$

The probability that a given star belongs to the satellite is then

$$P_{\rm sat} = \frac{f_{\rm sat}\,\mathcal{L}_{\rm sat}}{\mathcal{L}_{\rm tot}} = \frac{f_{\rm sat}\mathcal{L}_{\rm sat}}{f_{\rm sat}\mathcal{L}_{\rm sat} + (1 - f_{\rm sat})\mathcal{L}_{\rm bg}}. \tag{2.3}$$

J+24 fit this model using Monte Carlo Markov chain simulations, solving for the proper motions, satellite membership fraction ($f_{\rm sat}$), and structural properties of the second exponential density profile (if included). The inferred parameter modes are then used to calculate the $P_{\rm sat}$ we use for sample selection.

For our fiducial sample, we adopt a minimum probability of $P_{\rm sat} = 0.2$. We do not filter on magnitudes explicitly, but J+24's quality cuts typically only include stars with $G < 21$. We use the $P_{\rm sat}$ values from the elliptical 2-component runs if a galaxy shows evidence for an outer component, the 1-component run otherwise. Most stars have $P_{\rm sat}$ values which are nearly 0 or 1, so the exact choice of probability threshold has little effect on the resulting sample. Even at our relatively generous probability threshold of 0.2, the purity remains

high when validated against spectroscopic line-of-sight (LOS) velocities (~90%, J+24).[1] However, we find that our conclusions are unchanged when limiting samples to only the brightest stars. Altogether, the J+24 method provides a high-quality, low-contamination sample of dwarf galaxy candidate member stars, which we will now investigate in further detail.

2.2 The effects of membership criteria

We analyze stellar distributions in the tangent plane and consider the projected shape of a galaxy. The tangent plane coordinates ξ and η are offsets in right ascension (RA) and declination as measured on the plane tangent relative to the galaxy centre. To account for the elliptical shape of the galaxy, we use $R_{\rm ell}$, which we define as the circularized elliptical radius,

$$R_{\rm ell}^2 = a\, b\, \left(\frac{\xi'^2}{a^2} + \frac{\eta'^2}{b^2} \right), \tag{2.4}$$

where ξ' and η' are the tangent plane coordinates rotated to align with a dwarf galaxy's major and minor axes, and a and b are the semi-major and semi-minor axes of the galaxy.

We illustrate the likelihood-based membership selection criteria through a progressive tightening of criteria. First, we consider a minimally-refined sample, **all**, which only excludes stars with poor astrometry, unreliable photometry, or inconsistent parallaxes. Next, incorporating CMD and PM information, we use the **CMD+PM** to test a selection method agnostic to the spatial position. This sample includes stars where the CMD and PM combined likelihood favours satellite membership:

$$\mathcal{L}_{\rm CMD,\ sat}\, \mathcal{L}_{\rm PM,\ sat} > \mathcal{L}_{\rm CMD,\ bg}\, \mathcal{L}_{\rm PM,\ bg}. \tag{2.5}$$

Next, our **fiducial** sample, $P_{\rm sat} > 0.2$, includes a spatial likelihood as described in J+24. Finally, the **RV members** (for radial velocity) sample adds line-of-sight velocity information (see Appendix B for details). While the latter is the highest-purity membership sample, we do not use this sample for stellar density analysis due to its incompleteness and complex selection function.

Figs. 2.1, 2.2, 2.3 show our fiducial sample for three dSphs (Sculptor, Ursa Minor, and Fornax), as well as the impact of sample selection, in tangent-plane coordinates, the CMD, and proper-motion space. The "all" sample extends uniformly across the tangent plane, but

[1] This would indicate that the J+24 model probabilities are mis-calibrated. However, most LOS surveys of dwarf galaxies select brighter stars (which have better *Gaia* measurements) and likely members, complicating the interpretation of this purity estimate.

includes a substantial background population. The "CMD+PM" sample has a much lower background density in the tangent plane, revealing the satellite more clearly. The fiducial sample appears similar to the "CMD+PM" sample in the CMD and PM planes, but excludes improbably distant stars. The "RV members" sample also traces out similar distributions in CMD and PM space as the fiducial sample, with less dispersion, likely reflecting the brighter magnitudes of stars with spectroscopic follow-up. Each selection criterion—spatial, CMD, and PM—contributes towards a high-quality membership assignment.

Based on the fiducial sample's distribution in Figs. 2.1, 2.2, 2.3, Ursa Minor stands out because of its higher ellipticity. While Sculptor and Ursa Minor show an extended population of members past $6R_h$ in radius, Fornax does not, despite having many more stars. Fornax also has a bluer CMD, indicative of more recent star formation. Otherwise, there are no major morphological differences between these galaxies.

One limitation of the J+24 method is the assumption of a specific density profile for the dwarf galaxy (a one- or two-component exponential), which may impact the membership probability of distant stars. However, there are no clear extensions or overdensities in the "CMD+PM" selected sample, which does not include a spatial likelihood. If even fainter, more extended features exist, they are not obviously detectable with *Gaia*.

To illustrate the extent of Sculptor and Ursa Minor, we highlight distant, spectroscopically confirmed members with red-outlined stars in Figs. 2.1, 2.2. In particular, Sestito et al. (2023a); Sestito et al. (2023b) targeted distant, bright stars from the J+24 candidate membership list. The most distant stars confirmed in their work lie at radii $\gtrsim 10R_h$ from the centres of each dwarf. For an exponential profile, 0.05% of stars fall outside a radius of $6R_h$ and less than $1/10^6$ fall outside $10R_h$—the mere presence of very distant member stars implies likely deviations from an exponential profile.

2.3 Density profiles

We derive density profiles by binning member stars in constant-width bins in $\log R_{\rm ell}$ of 0.05 dex. We ignore bins interior or exterior to the first empty bin in either direction. We use symmetric Poisson uncertainties as error bars in the density estimate at each bin.

Fig. 2.4 shows the derived density profiles for Sculptor, Ursa Minor, and Fornax. We calculate density profiles for three different samples from above: "all," "CMD+PM," and the "fiducial" sample. In each case, all samples coincide towards the inner regions of the satellite. However, the density profile from "all" plateaus at the total background in the field at radii of 30-60 arcminutes, depending on the galaxy. By restricting stellar membership

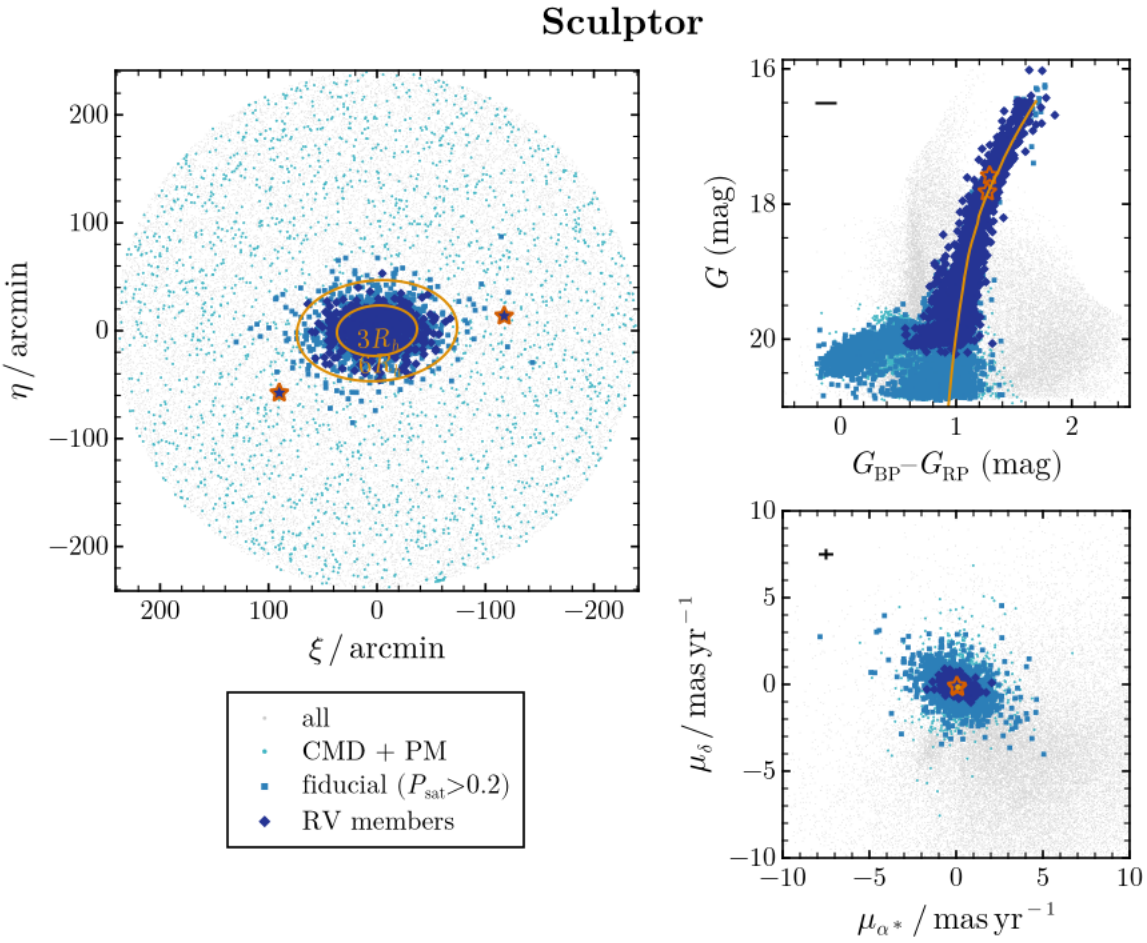

Figure 2.1: The distributions of various samples of *Gaia* stars for Sculptor. In each panel, we use light grey points for the "all" sample of stars, turquoise points for "CMD+PM" selected stars (Eq. 2.5), blue squares for the "fiducial" sample ($P_{\rm sat} > 0.2$), and indigo diamonds for the "RV members" sample. We mark the two far-outlier stars from Sestito et al. (2023a) with rust-outlined indigo stars. **Left:** Tangent plane ξ, η. The orange ellipses represent 3 and 6 half-light radii. **Top right:** Colour magnitude diagram in Gaia G magnitude versus $G_{\rm BP}-G_{\rm RP}$ colour. We plot a Padova 12 Gyr, [Fe/H] $= -1.68$ isochone in orange. The black bar in the top left represents the median member colour error. **Bottom right:** Proper motion in declination μ_δ vs RA $\mu_{\alpha*}$ (corrected). The orange point marks the systemic McConnachie & Venn (2020b) proper motion. The black cross represents the median member proper motion error.

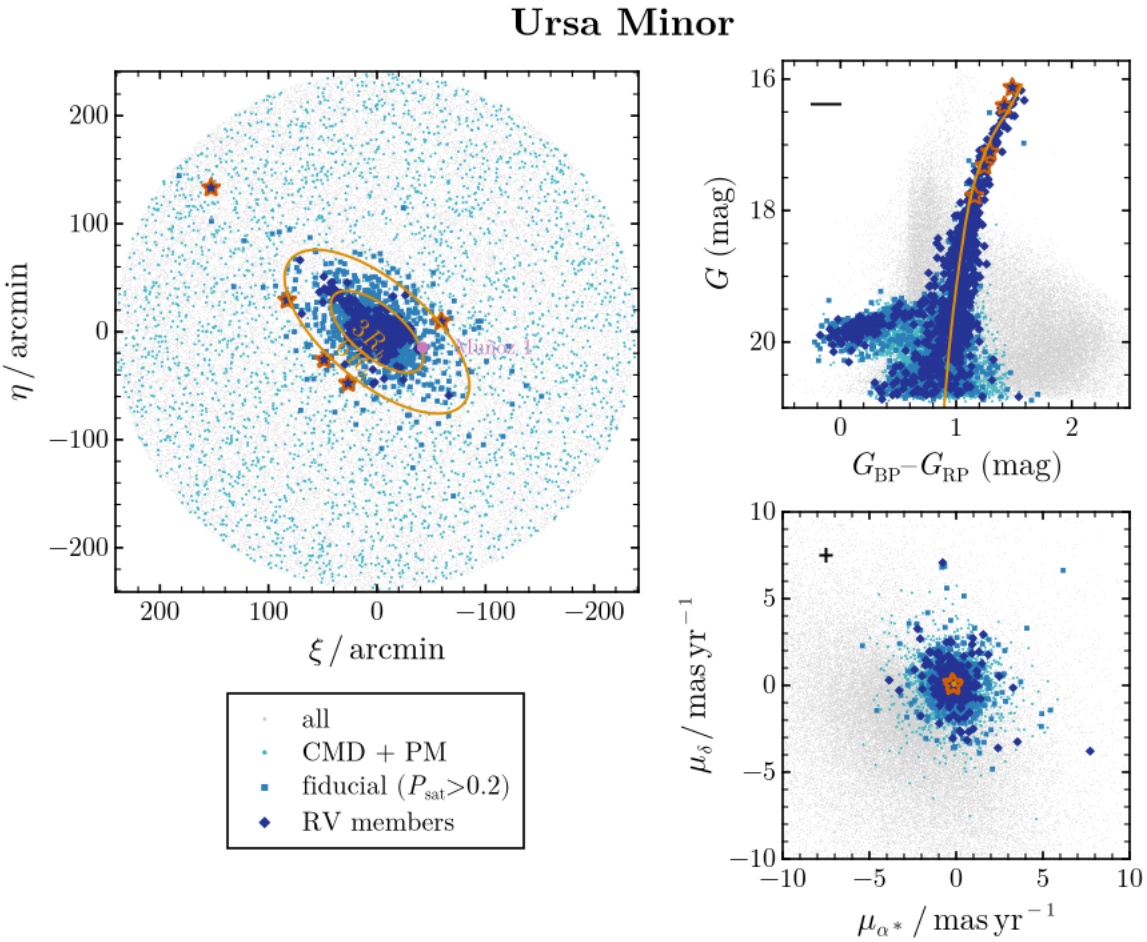

Figure 2.2: Similar to Fig. 2.1 except for Ursa Minor. We outline "velocity confirmed" members outside a radius of $6R_h$ with red stars (from Sestito et al. 2023b; Pace et al. 2020; Spencer et al. 2018). The isochrone is 12 Gyr old with [Fe/H] = −2.13. We also mark the location of Muñoz 1 with a pink circle.

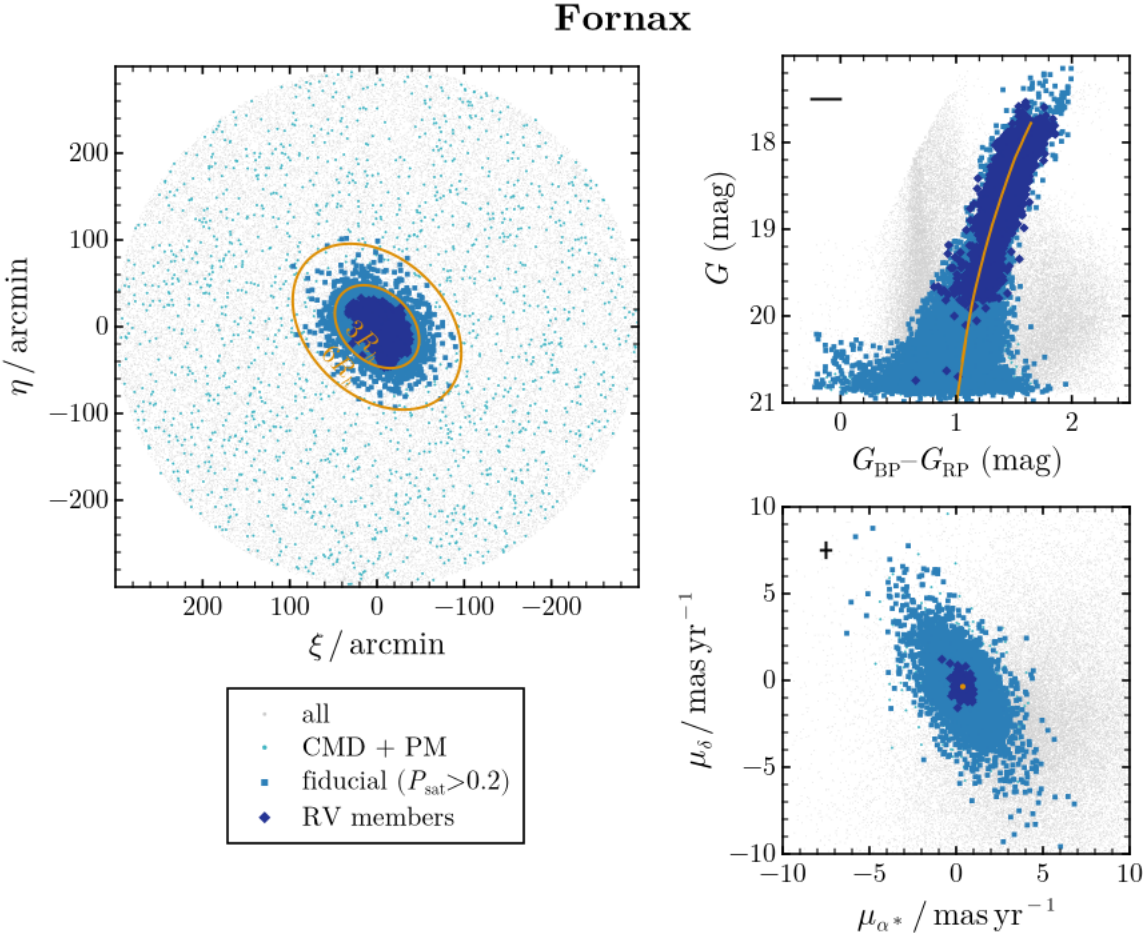

Figure 2.3: Similar to Fig. 2.1 except for Fornax. The isochrone is instead for a 2Gyr, [Fe/H] = −0.99 stellar population. RV measurements are from Walker et al. (2009a) and APOGEE. Fornax does not show the same extended outer halo of probable members as Sculptor or Ursa Minor.

with CMD and PM information, the background is reduced by 1–2 dex. The "CMD+PM" background plateau represents the density of background stars that could be mistaken as members because of their coincident colours and proper motions. Finally, the "all – background" profile results from subtracting the apparent background in the "all" profile.

The density profiles of all samples agree in the inner regions. However, outside $\sim 6R_h$, these profiles would diverge as the "fiducial" sample becomes vulnerable to the assumed spatial likelihood (an exponential in J+24). We thus truncate the fiducial profiles near the "CMD+PM" background to avoid misleading density profiles. We explore this in more detail in Appendix A.3.

Near UMi, there is a small ($R_h \sim 0.5'$), likely unassociated, ultra-faint star cluster, Muñoz 1 (Muñoz et al. 2012). The cluster is at a relative position of $(\xi, \eta) \approx (-42, -15)$ arcminutes, corresponding to an elliptical radius of 37 arcminutes. Muñoz 1 does not have a bright RGB, so the cluster has few stars above the *Gaia* magnitude limit. The cluster has little effect on the elliptically-averaged density profile (see location on Fig. 2.4).

Our density profiles are robust to alternative methodologies and magnitude cuts. Density profiles based on J+24 candidates may be biased by their assumed spatial likelihoods. To address this, we consider a Bayesian model with a non-parametric spatial likelihood. We also explore selections using absolute cuts, and the effect of structural assumptions of the density profile in Appendix A. These methodologies are consistent except when the derived density drops below the background of satellite-like stars (from the CMD+PM sample). We also do not find evidence of magnitude biases in the density profiles, indicating that inhomogeneous magnitude-completeness is small. Our density profiles furthermore agree with photometric surveys and similar literature (see Appendix A). We conclude that selection criteria do not influence our conclusions.

Fig. 2.5 compares the fiducial density profiles of Sculptor, Ursa Minor, Fornax, and other classical dwarf galaxies. Of the classicals, we exclude Antlia II, due to the extremely high background, and Sagittarius, which was not included in J+24. The density profiles are scaled to match at the half-light radius, taken from Muñoz et al. (2018). All of the classical dwarfs appear to be well described by an exponential profile in the inner regions.[2] In the outer regions, however, Sculptor and Ursa Minor deviate and show a clear outer excess over an exponential law (solid black line). These galaxies are better fit by a Plummer law (dashed black line). The deviation from an exponential grows outwards, and at $\sim 8R_h$, may reach 2

[2]Comparing density profiles of dwarf galaxies is complicated by variations in the effective depth between galaxies. However, the deviations between Scl, UMi, and other galaxies are apparent even where the data is complete across all dwarfs.

orders of magnitude. The remainder of this thesis will be devoted to assessing whether the outer excesses shown by Scl and UMi are due to Galactic tides.

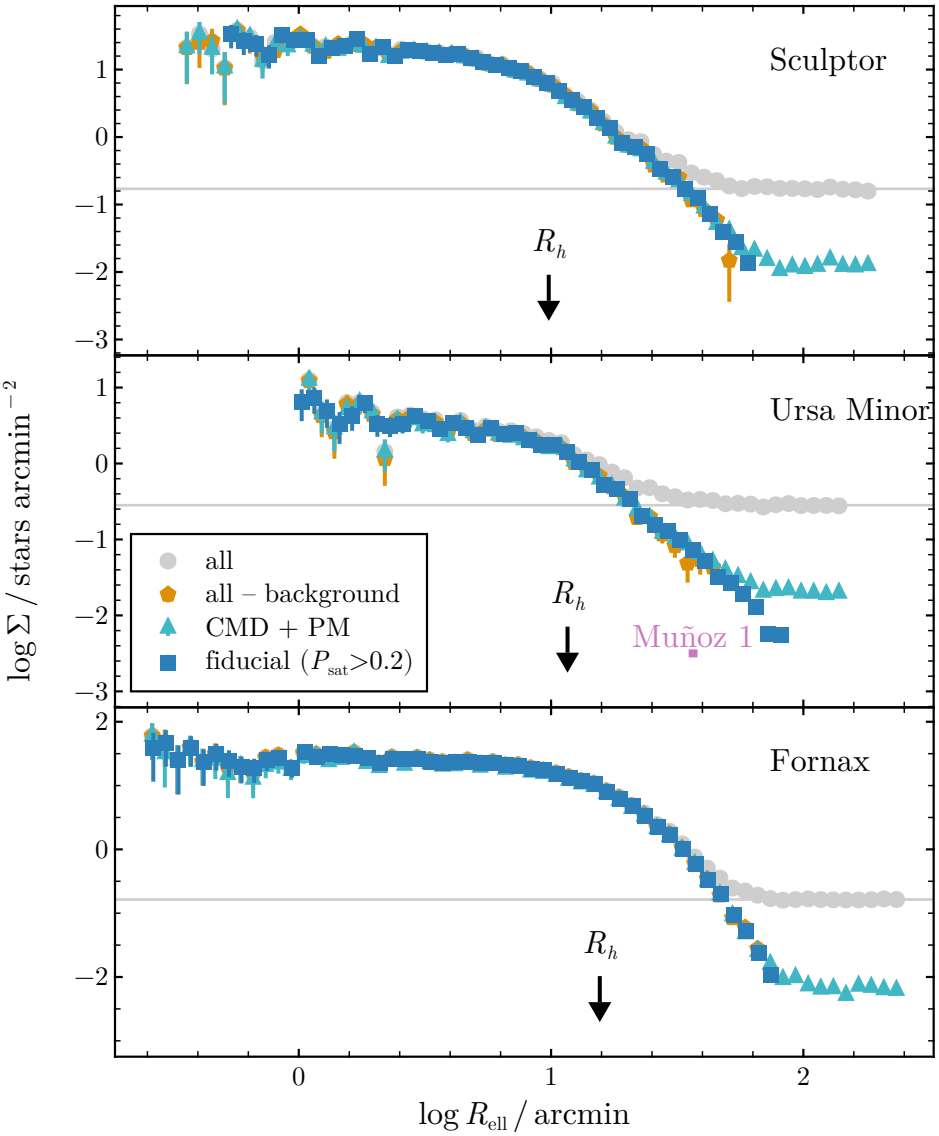

Figure 2.4: The density profile of Sculptor, Ursa Minor, and Fornax for different selection criteria, plotted as log surface density versus log elliptical radius. The samples are: "all" selects any high-quality and parallax-consistent star (grey circles), "all–background" subtracts a uniform background density from the "all" profile (orange pentagons), "CMD+PM" selects stars according to CMD and PM only (turquoise triangles), and "fiducial" also includes spatial information (blue squares). We mark the half-light radius with a vertical dashed line and the background density with the horizontal grey line. For Ursa Minor, we show the expected location of Muñoz 1 stars as a horizontal bar (ranging from ±3 times the cluster's half-light radii).

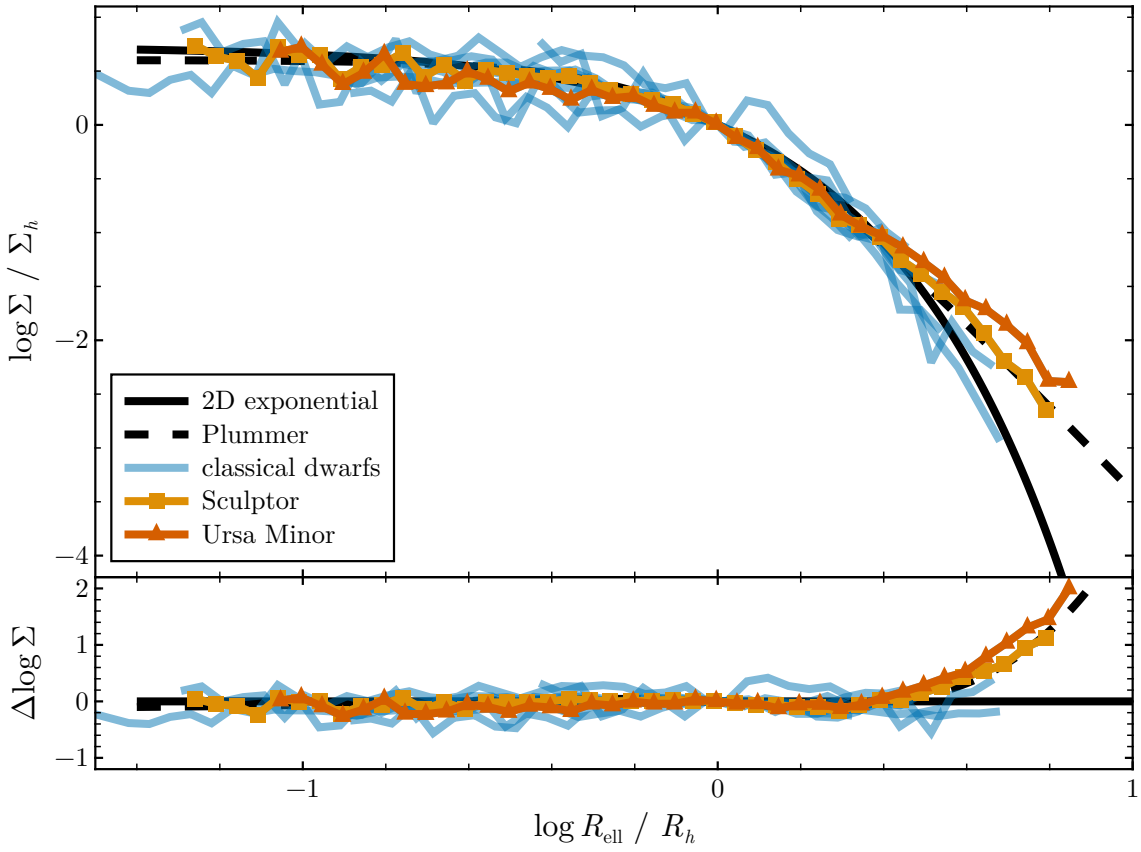

Figure 2.5: The density profiles of Sculptor, Ursa Minor, and other classical dwarfs compared to a 2D exponential and Plummer density profiles. Dwarf galaxies are scaled by the half-light radius and density at half-light radius. The residuals (lower panel) are with respect to a 2D exponential. Sculptor and Ursa Minor have an excess of stars in the outer regions (past $\log R/R_h \sim 0.3$) compared with other classical dwarfs.

3. Simulation Methods

In the previous Chapters, we have seen that the Scl and UMi classical dSphs have outer density profiles that appear to deviate from the exponential law that approximates well all other classical dSphs. Our main intention is to assess whether such deviations result from the effects of Galactic tides. To this purpose, we use N-body simulations of the evolution of CDM halos in a Galactic potential, constrained to have the orbital parameters consistent with a dwarf's present-day position and velocity. We shall assume that, over the past 10 Gyr, the Galactic potential is the static, analytic potential inferred by McMillan (2011) from observations of kinematic tracers. We also assume that the potential of each dwarf may be initially approximated by a cuspy NFW profile. Since the dwarfs in question are heavily dark-matter-dominated, we shall use a carefully selected sample of dark matter particles to emulate the evolution of an embedded tracer stellar component. In this Chapter, we describe our choice of Galactic potential, orbital estimation, initial conditions setup, and N-body methods.

3.1 Orbital estimation

To explore the possible orbits of a dwarf galaxy, we perform a Monte Carlo sampling of the present-day observables. The present-day position, distance modulus, LOS velocity, and proper motions are each sampled from normal distributions given the reported uncertainties in Tables 1.1, 1.2. We integrate each sampled position/velocity back in time for 10 Gyr using Agama (Vasiliev 2019). Dynamical friction is not expected to impact orbits substantially because of the low masses and large pericentres of the dwarfs, so we assume a single point-mass particle for the backwards integration.

3.1.1 Galactocentric frame

To convert observed positions and velocities to Galactocentric coordinates, we use the Astropy v4 Galactocentric frame (Astropy Collaboration et al. 2022). Our Cartesian Galactocentric coordinates here assume the Galactic centre is at $[x, y, z] = [0, 0, 0]$, where x is the

direction from the sun to the Galactic centre, y is the direction of the motion of the Local Standard of Rest, and z is the direction perpendicular to the Galactic plane. The coordinate frame is also right-handed, such that the z-angular momentum of the sun is negative (since the sun is at $x < 0$). In this frame, the solar position is $[-8.122 \pm 0.033, 0, 0.0208 \pm 0.003]$ kpc (GRAVITY Collaboration et al. 2018; Bennett & Bovy 2019) and the solar velocity is $\mathrm{v}_\odot = [-12.9 \pm 3.0, 245.6 \pm 1.4, 7.78 \pm 0.08]$ km/s (Reid & Brunthaler 2004; Drimmel & Poggio 2018; GRAVITY Collaboration et al. 2018). The uncertainties in this reference frame are typically smaller than the uncertainties on a dwarf galaxy's distance and tangential velocity.

3.1.2 Milky Way potential

We adopt the Milky Way potential described in Errani & Peñarrubia (2020), which is an analytic approximation to that proposed by McMillan (2011). Fig. 3.1 plots the circular velocity profiles of each component and the total circular velocity profile for this potential. The potential includes a stellar bulge, a thin and thick disk, and a dark matter NFW halo.

The Galactic bulge is described by a Hernquist (1990) potential,

$$\Phi(r) = -\frac{GM}{r+a}, \tag{3.1}$$

where $a = 1.3$ kpc is the scale radius and $M = 2.1 \times 10^{10}\,\mathrm{M}_\odot$ is the total mass. The thin and thick disks are represented with the Miyamoto & Nagai (1975) cylindrical potential,

$$\Phi(R, z) = \frac{-GM}{\sqrt{R^2 + \left(a + \sqrt{z^2 + b^2}\right)^2}}, \tag{3.2}$$

where a is the disc radial scale length, b is the scale height, and M is the total mass of the disk. For the thin disk, $a = 3.944$ kpc, $b = 0.311$ kpc, and $M = 3.944 \times 10^{10}\,\mathrm{M}_\odot$. For the thick disk, $a = 4.4$ kpc, $b = 0.92$ kpc, and $M = 2{\times}10^{10}\,\mathrm{M}_\odot$. The halo is an NFW dark matter halo (Eq. 1.1) with $r_{\mathrm{max}} = 43.7$ kpc and $\mathrm{v}_{\mathrm{max}} = 191\,\mathrm{km\,s^{-1}}$, or $M_{200} = 126.6 \times 10^{10}\,\mathrm{M}_\odot$ and $r_s = 20.2$ kpc.

3.1.3 Sculptor's orbit

Sculptor's orbit in the assumed potential is relatively well-constrained. Fig. 3.2 illustrates point particle orbits for 100 samples of Sculptor's observed kinematics integrated backwards for 10 Gyr in both Galactocentric Cartesian coordinates (x, y, z) and in Galactocentric radius

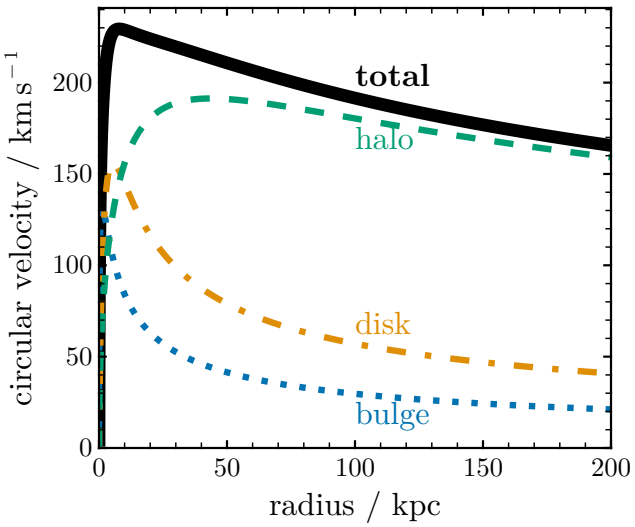

Figure 3.1: Circular velocity profile of Errani & Peñarrubia (2020) potential. The total circular velocity (thick black line) is composed of an NFW halo (green dashed line), thin and thick Miyamoto & Nagai (1975) disks (orange dash-dotted line), and a Hernquist (1990) bulge (blue dotted line).

with time. These orbits sample the uncertainties in distance, proper motion, and radial velocity, as given in Table 1.1. All sampled orbits of Sculptor have nearly the same shape—the orbit primarily resides in the y–z plane and completes a similar number of periods and pericentric and apocentric passages.

To maximize tidal effects, we select an orbit with the $\sim 3\sigma$ smallest pericentre among all possible orbits integrated backwards for 10 Gyr. We achieve this by taking the median parameters of all orbits with a pericentre less than the 0.0027th quantile pericentre, yielding a pericentre of 43 kpc. Given the current observations, it is unlikely that Sculptor has had a significantly smaller pericentre than our selected orbit, which we refer to as the `smallperi` orbit. We take the first apocentre after a look-back time of 10 Gyr, or at ~ 9.1 Gyr, as the initial conditions for our model of Sculptor, noted in Table 3.1.

3.1.4 Ursa Minor's orbit

Similar to Sculptor, Ursa Minor has a well-constrained orbit in the assumed MW potential. Fig. 3.3 shows 100 random point-mass orbits of Ursa Minor. As for Sculptor, we select an orbit with approximately the 3σ smallest pericentre, the Ursa Minor `smallperi` orbit (see Fig. 3.3 and Table 3.1).

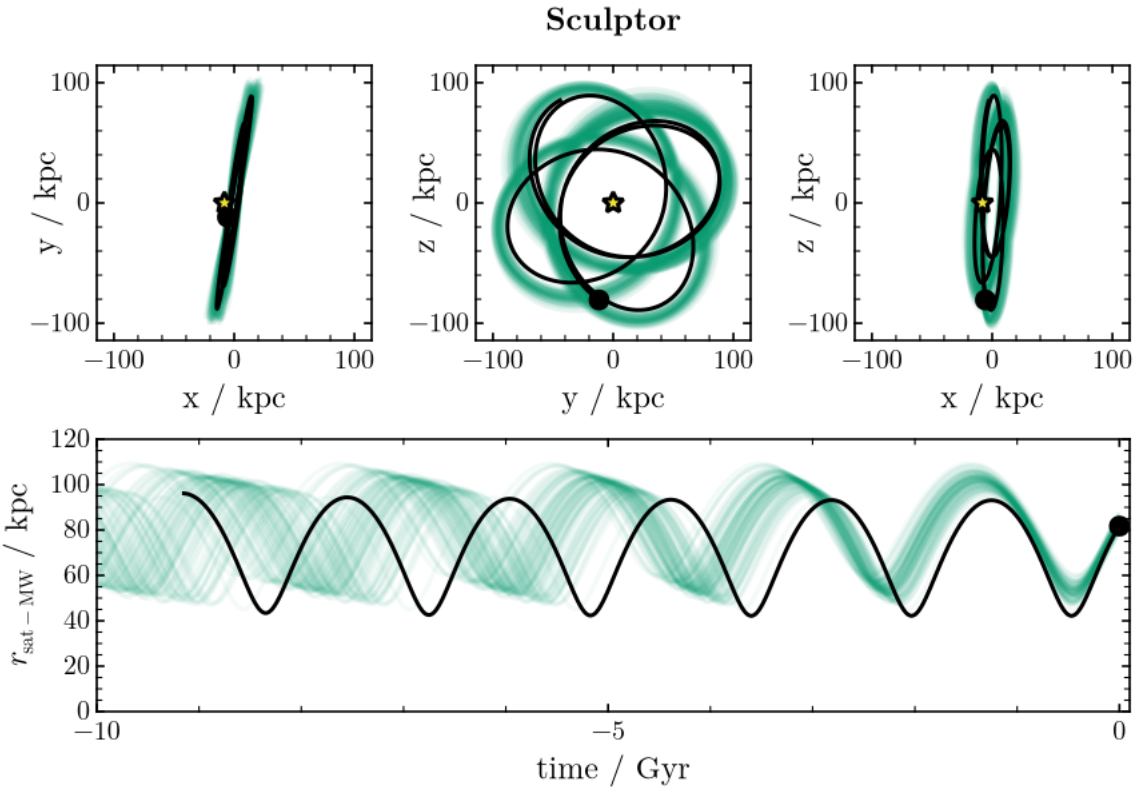

Figure 3.2: The orbits of Sculptor in a static Milky Way potential in Galactocentric x, y, and z coordinates (top) and in Galactocentric radius r versus time (bottom). The Milky Way is at the centre with the disk lying in the x–y plane and the yelow star marks the Sun's location. The black line shows our N-body's `smallperi` orbit and light green transparent lines represent orbits sampled over Sculptor observables in Table 1.1. The orbit of Sculptor is well-constrained in this potential, and it is unlikely to achieve a smaller pericentre than the `smallperi` orbit.

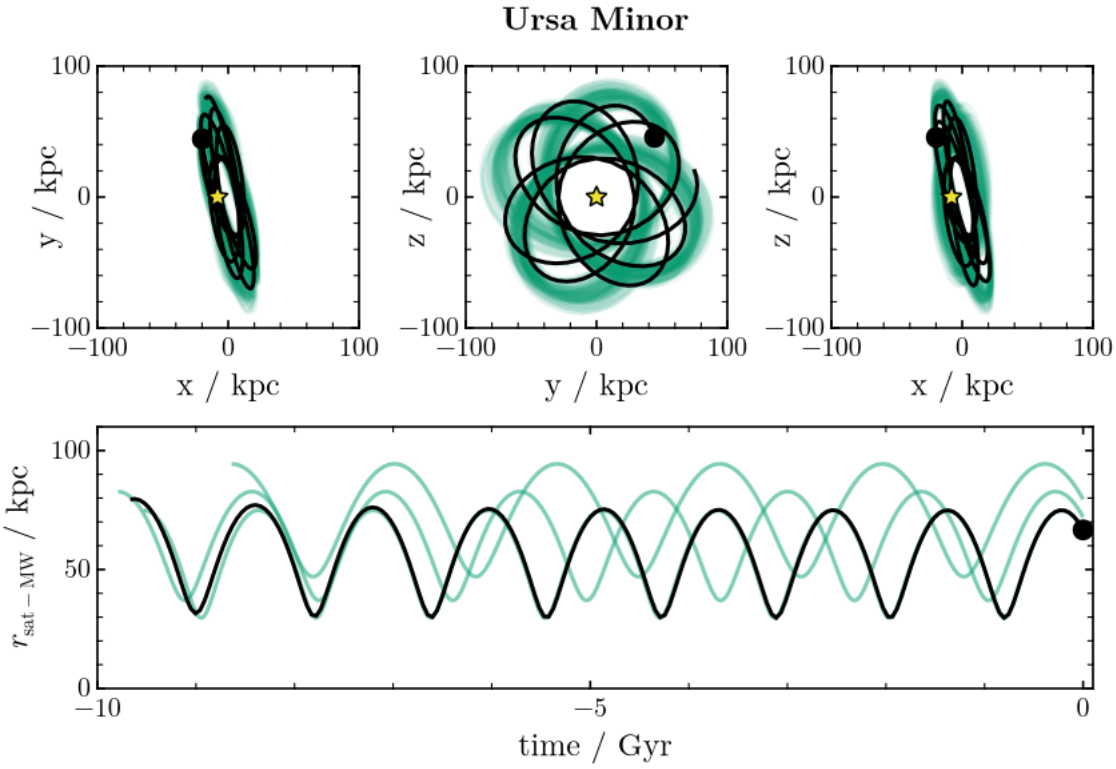

Figure 3.3: Similar to Fig. 3.2, the orbits of Ursa Minor in a static Milky Way potential in Galactocentric x, y, and z coordinates. In the lower panel, we show the radius versus time for the selected `smallperi` N-body orbit (black) and three point orbits of Ursa Minor, representing the `smallperi`, the mean orbit, and 3σ-largest pericentre orbit.

Table 3.1: The orbital initial conditions for models presented in this work. The observables record the intended final position of the N-body model derived from point-mass orbit quantiles. Instead, the initial position and velocity represent the initial conditions for the actual N-body model. The `smallperi` orbits represents the 3σ-smallest-pericentre orbit, which we use to provide an upper limit on tidal effects. We describe the `LMC-flyby` orbit in Section 4.1.3.

Property	Scl: `smallperi`	Scl: `LMC-flyby`	Umi: `smallperi`
distance / kpc	82.6	73.1	64.6
$\mu_{\alpha*}$/mas^{-1} yr^{-1}	0.134	0.137	-0.158
μ_{δ}/mas^{-1} yr^{-1}	-0.198	-0.156	0.050
LOS velocity / km s^{-1}	111.2	111.2	-245.75
t_i/Gyr	-9.17	-2.0	-9.67
x_i/kpc	-2.49	4.30	-17.40
y_i/kpc	-42.78	138.89	74.51
z_i/kpc	86.10	125.88	21.34
$\mathrm{v}_{x,i}$/km s^{-1}	-20.56	6.89	14.27
$\mathrm{v}_{y,i}$/km s^{-1}	-114.83	-56.83	48.62
$\mathrm{v}_{z,i}$/km s^{-1}	-57.29	52.09	-114.08

We shall see later that the orbit of Ursa Minor's N-body model differs from the point particle orbit because of the effects of tidal mass loss. To ensure the final conditions of the N-body simulation are close to the intended final position, we iteratively adjust Ursa Minor's initial conditions. Initially, starting with low-resolution runs, we adjust the cylindrical actions of the initial orbit by the final difference in actions at the end of orbital evolution. After the initial actions have converged (2 iterations), we change the initial action angles by the final difference in action angles (2 more iterations). This method converges to an orbit agreeing with the observed kinematics of Ursa Minor. Since Sculptor's orbit is less strongly affected by tides, we do not carry out this correction for Sculptor.

3.2 Initial conditions

We use Agama (Vasiliev 2019) to generate the initial N-body dark matter halo. We assume galaxies are described by a spherical, isotropic NFW dark matter potential (Eq. 1.1). We also assume the stars do not contribute to the potential. The dark matter density is truncated

in the outer regions by

$$\rho_{\rm tNFW}(r) = e^{-(r/r_t)^3}\,\rho_{\rm NFW}(r), \tag{3.3}$$

where we adopt $r_t = 20 r_s$.

3.2.1 Initial dark matter halos for Sculptor and Ursa Minor

The observed half-light radius and velocity dispersion of Sculptor and Ursa Minor, together with the mass-concentration relation of ΛCDM halos, determine the properties of the N-body models adopted for each dwarf.

Table 3.2 lists our inferred halo and kinematic properties of Sculptor and Ursa Minor. First, taking the absolute magnitudes from Muñoz et al. (2018) with the mass-to-light ratio from Woo et al. (2008), the total current stellar mass of Sculptor and Ursa Minor are $M_\star \approx 3.1 \times 10^6 {\rm M}_\odot$ and $M_\star \approx 7 \times 10^5 {\rm M}_\odot$, respectively. Based on the stellar mass-$\rm v_{max}$ relation (from Fattahi et al. 2018), Sculptor and Ursa Minor's halos should have $\rm v_{max} \approx 31\,km\,s^{-1}$ and $\rm v_{max} \approx 27\,km\,s^{-1}$. Finally, using the Ludlow et al. (2016) $z = 0$ mass-concentration relation, this constraint translates into a $r_{\rm max} \approx 6\,$kpc and $r_{\rm max} \approx 5\,$kpc for each galaxy.

The observed velocity dispersion constrains the inner mass profile. From the Wolf et al. (2010) mass estimator, the mass contained within the 3D half-light radius r_h is

$$M(r_h) \approx \frac{3}{G}\sigma_{\rm v}^2\, r_h \tag{3.4}$$

for a velocity dispersion $\sigma_{\rm v}$. For Scl and UMi, the cosmological mean parameters above would predict $\sigma_{{\rm v},i} \approx 8.5\,{\rm km\,s^{-1}}$ and $8.0\,{\rm km\,s^{-1}}$ assuming $r_h = 240\,$pc. This is below the observed values of $9.7\,{\rm km\,s^{-1}}$ and $8.7\,{\rm km\,s^{-1}}$, and tidal evolution will further reduce the dispersion. To match the observed $\sigma_{\rm v}$ at the end of the simulation, we choose $\rm v_{max} = 31\,km\,s^{-1}$ and $r_{\rm max} = 3.2\,$kpc for Scl and $\rm v_{max} = 38\,km\,s^{-1}$ and $r_{\rm max} = 4\,$kpc for UMi.

While there is some range in the choice of initial halo, reasonable changes to the initial halo do not substantially affect the tidal evolution for either galaxy. So, the tidal effects on stars should be similar for halos with similar velocity dispersions (See Appendix D).

3.3 Numerical methods

3.3.1 The N-body code: GADGET-4

To simulate the tidal evolution of galaxies, we use N-body simulations integrated with the parallel, gravitational-tree program GADGET-4 (Springel et al. 2021). The N-body method

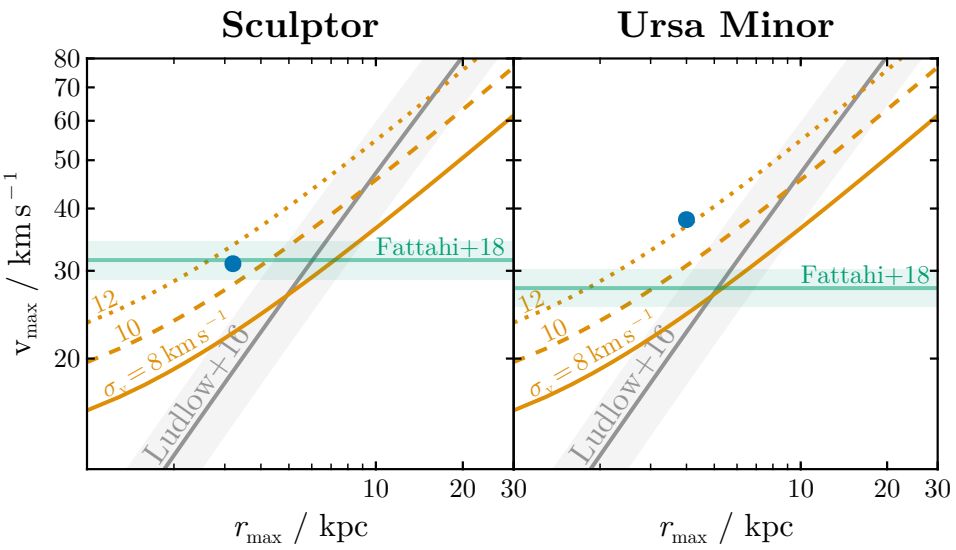

Figure 3.4: The blue point indicates our choice of initial halo parameters for Sculptor and Ursa Minor. The grey line and green line with shaded regions represent the Ludlow et al. (2016) mass-concentration relation and Fattahi et al. (2018) SMHM relation, respectively. The curved orange lines show the velocity dispersion of an exponential stellar component with the observed half-light radius of Sculptor and Ursa Minor.

Table 3.2: Inferred properties of the stellar component and halo for Sculptor and Ursa Minor. We record the total luminosity, stellar mass, mass-to-light ratio, dark matter halo v_{max} and r_{max}, and dark matter halo virial mass M_{200} and concentration c_{NFW}. Uncertainties are the 16-84th percentile derived using Monte Carlo sampling, assuming 0.035 and 0.1 dex uncertainties in the $v_{max}(M_\star)$ and $c(M_{200})$ relations.

parameter	Sculptor	Ursa Minor
$L_\star$	$1.8 \pm 0.2 \times 10^6\ L_\odot$	$3.5 \pm 0.1 \times 10^5\ L_\odot$
$M_\star$	$3.1^{+1.6}_{-1.0} \times 10^6\ \mathrm{M}_\odot$	$7^{+3}_{-2} \times 10^5\ \mathrm{M}_\odot$
$M_\star/L_\star$	$1.7 \times 10^{\pm 0.17}$	$1.9 \times 10^{\pm 0.17}$
v_{max}	$31.5 \pm 3\,\mathrm{km\,s^{-1}}$	$27^{+3}_{-2}\,\mathrm{km\,s^{-1}}$
r_{max}	6 ± 2 kpc	5^{+2}_{-1} kpc
M_{200}	$0.5 \pm 0.2 \times 10^{10}\ Mo$	$0.3^{+0.2}_{-0.1} \times 10^{10}\,\mathrm{M}_\odot$
c_{NFW}	13^{+4}_{-3}	13.5^{+4}_{-3}

calculates and evolves the gravitational accelerations between a large number of collisionless particles to approximate the dynamical evolution of matter. To approximate a collisionless system (i.e., without strong particle-particle gravitational deflections), the force is tapered below a *softening length*. Resolution is limited by the number of particles and the softening length. Tree codes organize particles into a spatial tree, enabling the grouping of the gravitational forces from nearby particles. A gravitational tree code substantially reduces the required number of force computations, as compared to the exact, direct-summation method.

3.3.2 Isolation runs and simulation parameters

To ensure that the initial conditions of the simulation are dynamically relaxed and well-converged, we run a halo first in isolation using GADGET-4. Since gravity is scale-free, we use the same isolation run for all halos and rescale the results to the desired values of size and mass. We adopt a fiducial value of $r_{max} = 6.0\,\mathrm{kpc}$ and $v_{max} = 31\,\mathrm{km\,s^{-1}}$ for the isolation halo based on Sculptor's mean properties. We run this model for 5 Gyr (about one-half crossing time $t_{cross} = 2\pi\, r/v_{circ} \approx 9\,\mathrm{Gyr}$ at $r_{200} = 36\,\mathrm{kpc}$).

For our simulation parameters, we adopt a softening length of

$$h_{grav} = 0.014\,\mathrm{kpc}\left(\frac{r_{max}}{6.0\,\mathrm{kpc}}\right)\left(\frac{N}{10^7}\right)^{-1/2}, \tag{3.5}$$

for a halo with N particles. GADGET-4 adopts a spline kernel softening law (eqs. 70–71 in Springel et al. 2001; but with the spline characteristic radius $2.8h_{\rm grav}$, see Springel et al. 2021). See Appendix C for a discussion of this choice and our simulation parameters, which is similar to the Power et al. (2003) suggested softening.

3.3.3 Numerical fidelity

Fig. 3.5 illustrates how well our numerical setup is able to reproduce the desired initial conditions, before and after running the model in isolation. This figure shows that our numerical methods are able to approximate well an NFW halo down to a resolution-dependent radius. The larger the number of particles, the smaller the radius that is effectively "resolved" in a given simulation. For the Sculptor-like halo shown in this figure (with $r_{\rm max} = 6.0\,$kpc and $v_{\rm max} = 31\,{\rm km\,s^{-1}}$), a simulation with 10^7 particles is needed to resolve the innermost 100 pc. For reference, the half-light radius of Sculptor is ∼200 pc, which means that at least 10 million particles are needed to follow faithfully its tidal evolution.

Vertical arrows in Fig. 3.5 indicate the "convergence radius" defined by Power et al. (2003; their eq. 13) for NFW halos formed in cosmological N-body simulations. This radius marks the region where collisional effects driven by the finite number of particles used to describe the innermost regions of a halo become important over a Hubble time in a cosmological simulation. Our effective resolution is nearly the converged radius. The softening length (from Eq. 3.5) is typically a few times smaller than the converged length.

3.3.4 Orbital evolution

Next, we evolve the halo in the Galactic potential. We scale the relaxed snapshot and softening length to match the initial halo, and shift the snapshot to the initial conditions inferred from the orbital analysis (see Table 3.1). We then evolve the full N-body NFW model forward in time in the Galactic potential until the present time, when the halo is closest to its present-day observed position in the MW halo.[1]

3.3.5 Halo centring

To accurately follow the evolution of a halo, we must determine the centre of the self-bound halo remnant at each time chosen for analysis. We use a shrinking-spheres centre method inspired by Power et al. (2003). First, we start with an initial centre estimate using all bound

[1]Specifically, the snapshot which best agrees (as measured by χ^2) with the intended final position (in Table 3.1) and the observed position and velocity uncertainties. We use R_h as the uncertainty in α and δ.

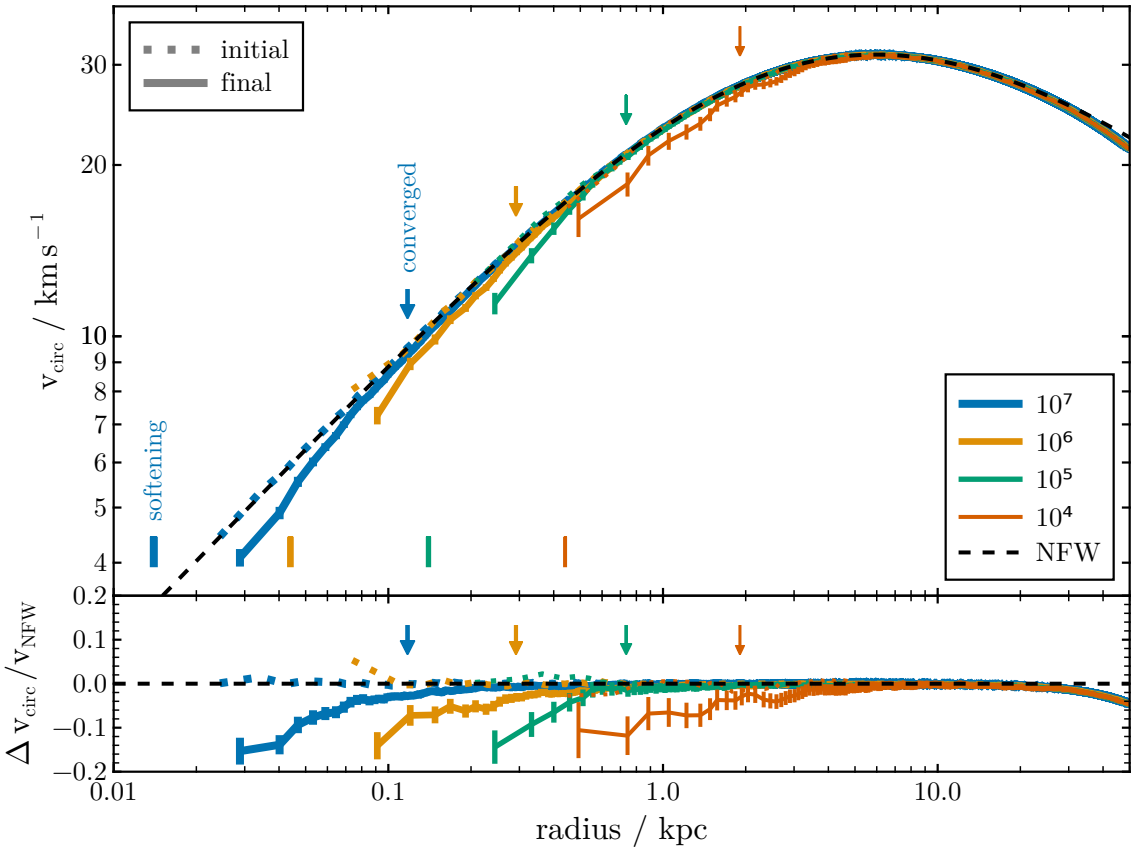

Figure 3.5: Numerical convergence test for circular velocity as a function of radius for simulations with different total numbers of particles in isolation. Residuals in the bottom panel are relative to NFW. The initial conditions are dotted, the converged radius is marked by arrows (eq. 13, Power et al. 2003), and the softening length is marked by a vertical bar. Note that a slight reduction in density starting around $r = 30$ kpc is expected given our outer truncation choice.

particles from the previous snapshot. Then, we calculate the distance of all particles from the centre, remove particles with a distance beyond the 0.95 quantile of the centre, and recalculate the centre of mass. The procedure is repeated until the selection radius is less than ~1kpc or fewer than 0.1% of particles remain. We then remove all unbound particles based on the GADGET-4 calculated potential of the halo and recalculate the centre. For all future timesteps, we consider only particles retained from the previous iteration.

The statistical centring uncertainty for the full resolution (10^7 particle) isolation run is ~0.003 kpc, but fluctuations are observed ~0.03 kpc. This is about three times the softening length but is still less than the numerically converged radial scale.

3.3.6 Sculptor and Ursa Minor's initial stellar components

We "paint" stars onto dark matter particles using the particle-tagging method (e.g., Bullock & Johnston 2005), assuming spherical symmetry. We initially assume stars follow a projected exponential law (Eq. 1.3) with $R_s = 0.10\,\mathrm{kpc}$ for both galaxies. The tagging method assigns a probability to each dark matter particle, which is proportional to the "light-to-mass" ratio required to match the assumed stellar light profile. We briefly describe the procedure next, but refer interested readers to Errani & Peñarrubia (2020).

Let Ψ be the potential (normalized to vanish at infinity) and $\mathcal{E}$ the binding energy, $\mathcal{E} = \Psi - 1/2v^2$. If we know the distribution function[2] $f(\mathcal{E})$, then we assign a stellar weight to a given particle with energy $\mathcal{E}$ using

$$P_\star(\mathcal{E}) = \frac{f_\star(\mathcal{E})}{f_{\rm halo}(\mathcal{E})}. \tag{3.6}$$

We use Eddington inversion to find the distribution function,

$$f(\mathcal{E}) = \frac{1}{\sqrt{8}\,\pi^2}\left(\int_0^{\mathcal{E}} \frac{d^2\rho}{d\Psi^2}\frac{1}{\sqrt{\mathcal{E}-\Psi}}\,d\Psi + \frac{1}{\sqrt{\mathcal{E}}}\left(\frac{d\rho}{d\Psi}\right)_{\Psi=0}\right) \tag{3.7}$$

(eq. 4-140b in Binney & Tremaine 1987). In practice the right, boundary term is zero.[3] We take Ψ from the underlying assumed analytic dark matter potential. $\rho_\star$ can be calculated from the surface density, $\Sigma_\star$, via the inverse Abel transform.

Fig. 3.6 shows the initial circular velocity profiles of stars and dark matter, demonstrating that these galaxies are stable in isolation and that the stellar component contributes

[2] i.e., the phase-space density of particles. Note that since f is formally defined in 6D phase space, there is an additional "density of states" term in order to calculate the histogram of particles with $\mathcal{E}$, $dM/d\mathcal{E}$ (section 4.4.5, Binney & Tremaine 1987).

[3] If, at large r, $\rho \propto r^{-n}$ with $n > 1$, then Ψ falls off no steeper than $\Psi \sim r^{-1}$. So $d\rho/d\Psi$ decays no less rapidly than r^{-n+1} which $\to 0$ at large r.

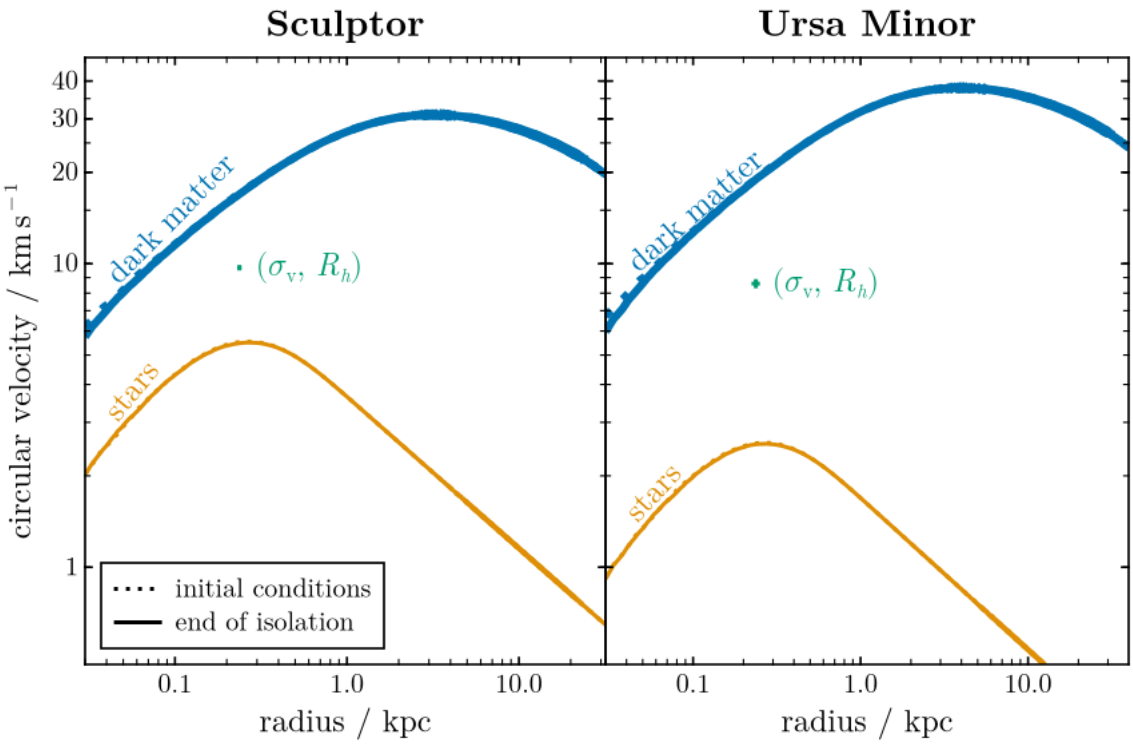

Figure 3.6: The initial circular velocity profiles of dark matter (blue) and stars (orange) for Sculptor and Ursa Minor. The initial conditions are dotted, and the isolation-evolved profiles are solid. The green cross marks the present-day half-light radius and velocity dispersion. To calculate the velocity profiles, unbound particles are iteratively removed, recalculating the potential at each step assuming spherical symmetry.

negligibly to the total mass ($M \sim v_{circ}^2 R$). Our cosmologically-motivated, observationally-based, and numerically-converged initial conditions enable us to accurately consider tidal effects in the next Chapter.

4. Galactic Tidal Effects on Sculptor and Ursa Minor

As discussed in Chapters 1 and 2, this thesis aims to test whether Galactic tides are responsible for the extended density profiles of Scl and UMi. In this Chapter, we analyze tailored N-body simulations, using the methods described in Chapter 3, to assess the tidal impact of the Galactic potential. To anticipate our main conclusion, we find that tides drive dark matter loss in both systems but leave their compact stellar components largely unaffected. The Large Magellanic Cloud (LMC) has the potential of substantially perturbing Scl's and even UMi's orbit, yet the resulting tidal effects are still too weak to account for the extended outer profiles. Our simulations thus demonstrate that recent tides are unlikely to have altered the stellar structure of Scl or UMi.

In this Chapter, we consider Scl first, describing tidal effects from the MW on its dark matter and stellar components. Next, we consider how accounting for the LMC may affect our conclusions. We then analyze UMi, considering in turn the dark matter evolution, stellar evolution, and orbital effects of the LMC.

4.1 Tidal effects on Sculptor

4.1.1 Evolution of Sculptor's dark matter halo

As a representation of an extreme tidal history, we initially investigate the `smallperi` orbit, described in Section 3.1.3, chosen to maximize possible effects of Galactic tides.

Scl experiences moderate tidal mass loss after 10 Gyrs of evolution. Fig. 4.1 shows the stripping of dark matter and the formation of diffuse streams trailing and leading Sculptor's orbit. Because tidal stripping can be described as a gradual removal of the least bound particles, most mass loss occurs in the outer halo. Instead, the inner regions of the galaxy may be relatively unaffected.

N-body models may deviate from a point-particle trajectory due to dynamical "self-friction" (e.g., White 1983; Miller et al. 2020). However, this effect is slight for Scl, which ends near the observed position, without adjusting the initial conditions (the green point in Fig. 4.1).

Table 4.1: The orbital and dark matter properties for the simulation of Sculptor. The random samples column shows the distributions from point orbits, and the `smallperi` column contains the results from the N-body simulation.

Property	random samples	`smallperi`
pericentre / kpc	53 ± 3	42
apocentre / kpc	102 ± 3	94.4
time of last pericentre / Gyr	-0.45 ± 0.2	-0.47
number of pericentres	5–6	6
Jacobi radius / kpc	4.5 ± 0.3	3.5
Jacobi radius / arcmin	186 ± 12	148
final heliocentric distance / kpc	83.2 ± 2	81.6
$v_{\mathrm{max,\,f}}/v_{\mathrm{max,\,i}}$		0.695
$r_{\mathrm{max,\,f}}/r_{\mathrm{max,\,i}}$		0.406
fractional final bound mass		0.0893

The inner density cusp is tidally resilient. Fig. 4.2 shows the initial and final circular velocity profiles, and the evolution of the maximum circular velocity. The maximum velocity drops from 31 km s^{-1} to 22 km s^{-1}, evolving along the tidal track from Errani & Navarro (2021). The final circular velocity profile resembles the initial with an inner cusp, but has a sharper outer truncation. Quantitatively, the halo loses $> 90\%$ of its initial mass (see Table 4.1). However, the inner structure is not affected, as the Jacobi radius is over 3 kpc, outside of r_{max} (see Table 4.1 and Fig. 4.2). Thus, tides may remove significant amounts of mass, but mostly from the outer halo.

4.1.2 Evolution of Sculptor's stars

Tides minimally affect the stellar component of Sculptor in the `smallperi` orbit. In Fig. 4.3, the projected stellar distribution displays no prominent distortions, and the radial density profile is nearly unchanged. Only at a surface density $\sim 10^8$ times fainter than the centre do some faint tidal features emerge. The total stellar mass lost corresponds to ~ 10 stars in total (see Table 4.1)—a formidable challenge to detect even with the best of observations.

This result implies that Scl's extended profile cannot be reproduced by Galactic tides operating on an initially exponential profile. The weak effect of tides suggests that the outer profile of Sculptor is innate, and not the result of tidal evolution. We check this assertion by

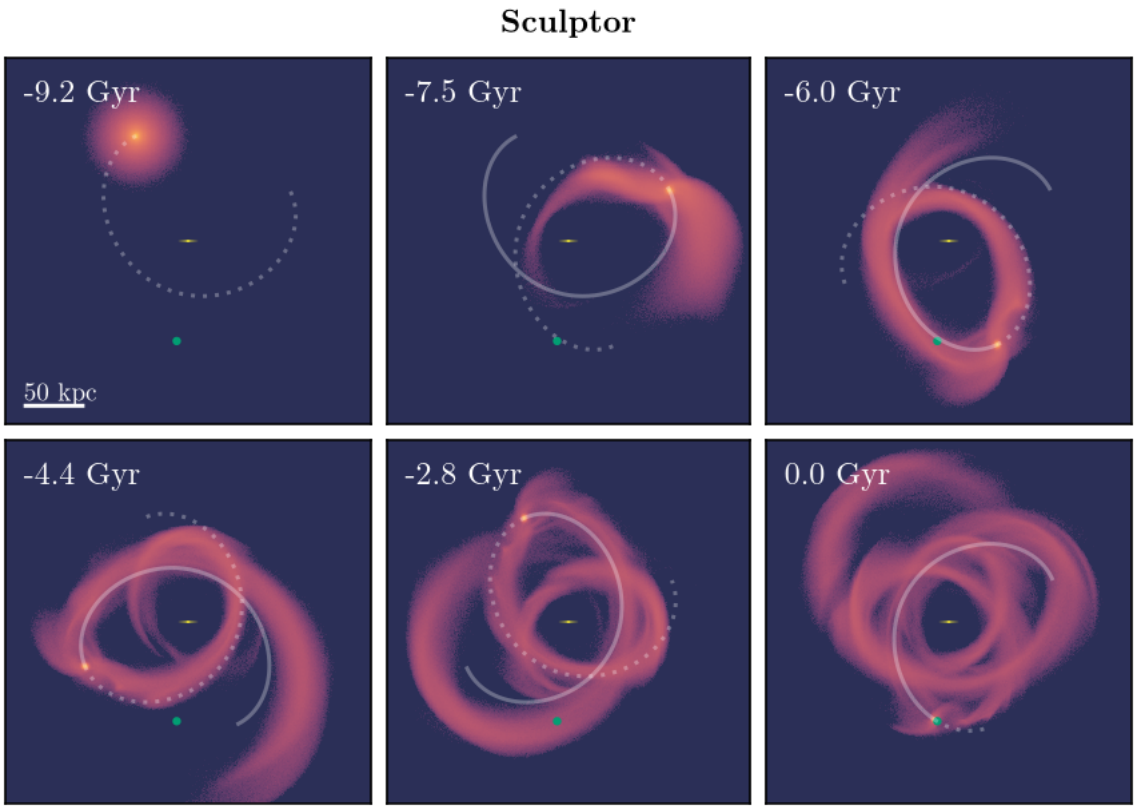

Figure 4.1: Images of the dark matter evolution over a selection of past apocentres and the present day. Limits range from -150 to 150 kpc in the y–z (~orbital) plane, and the colourscale is logarithmic, spanning 5 orders of magnitude between the maximum and minimum values. The green dot represents the final expected position of the galaxy, and the solid and dotted grey curves represent the orbit over one previous or future radial oscillation, respectively.

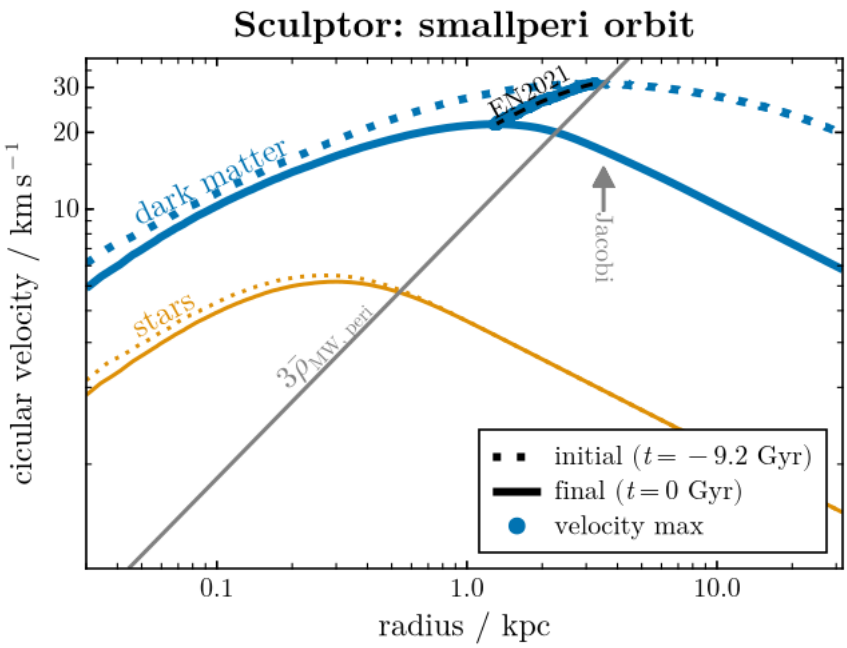

Figure 4.2: Dynamical evolution for the `smallperi` model of Sculptor. Dotted and solid lines show the initial and final circular velocity profiles, and blue and orange lines show the dark matter and stellar (2D exponential) profiles. The blue points represent the evolution of the maximum circular velocity, and the dashed black line shows the tidal track from Errani & Navarro (2021). The grey diagonal line marks three times the MW mean enclosed density at pericentre, whose intersection with the initial halo is the Jacobi radius.

Table 4.2: The present-day stellar properties for the simulations of Sculptor. In each row, we have the initial stellar velocity dispersion (within 1kpc), the final velocity dispersion, the fraction of stellar mass unbound, the initial half-light radius, the final half-light radius, and the break radius in arcmin and kpc (Eq. 1.8).

Property	Exponential	Plummer
$\sigma_{\mathrm{v},i}$ / km s^{-1}	9.8	10.7
$\sigma_{\mathrm{v},f}$ / km s^{-1}	8.8	9.4
fractional stellar mass loss	2.1×10^{-6}	0.024
$R_{h,i}$ / kpc	0.169	0.202
$R_{h,f}$ / kpc	0.189	0.227
break radius / arcmin	98	105
break radius / kpc	2.3	2.5

choosing a different initial stellar profile which matches the observed profile and assessing how it evolves on the `smallperi` orbit. We show in Fig. 4.4 that a Plummer profile (instead of an exponential) provides an adequate fit to Scl's observed profile. The Plummer model loses more stellar mass and forms more luminous tidal tails. Observations reaching surface densities ~ 10 times fainter than our data could reveal a stream in this case. Nevertheless, over the radial extent probed by our data, the stellar profile remains nearly unchanged by tidal evolution.

The Jacobi and break radii further support the conclusion that tidal effects should not be apparent. As calculated for this model (see Tables 4.1, 4.2), the break and Jacobi radii both fall outside $\gtrsim 100$ arcminutes, beyond the reach of our data. Indeed, the stellar component only begins to deviate from an exponential profile around the break radius (Figs. 4.3, 4.4). Since no orbits of Scl produce significantly smaller break or Jacobi radii, it is unlikely that any orbit would produce an observable density excess.

Table 4.2 quantifies the evolution of stellar properties. We calculate the velocity dispersion using all particles within 1 kpc of the dwarf's centre. The stellar velocity dispersion decreases by only ~ 1 km s^{-1} and the half-light radius expands by $\sim 10\%$. This is consistent with adiabatic expansion due to the reduction of the total mass (e.g., Stücker et al. 2023). Altogether, Galactic tides negligibly impact Scl's stellar component.

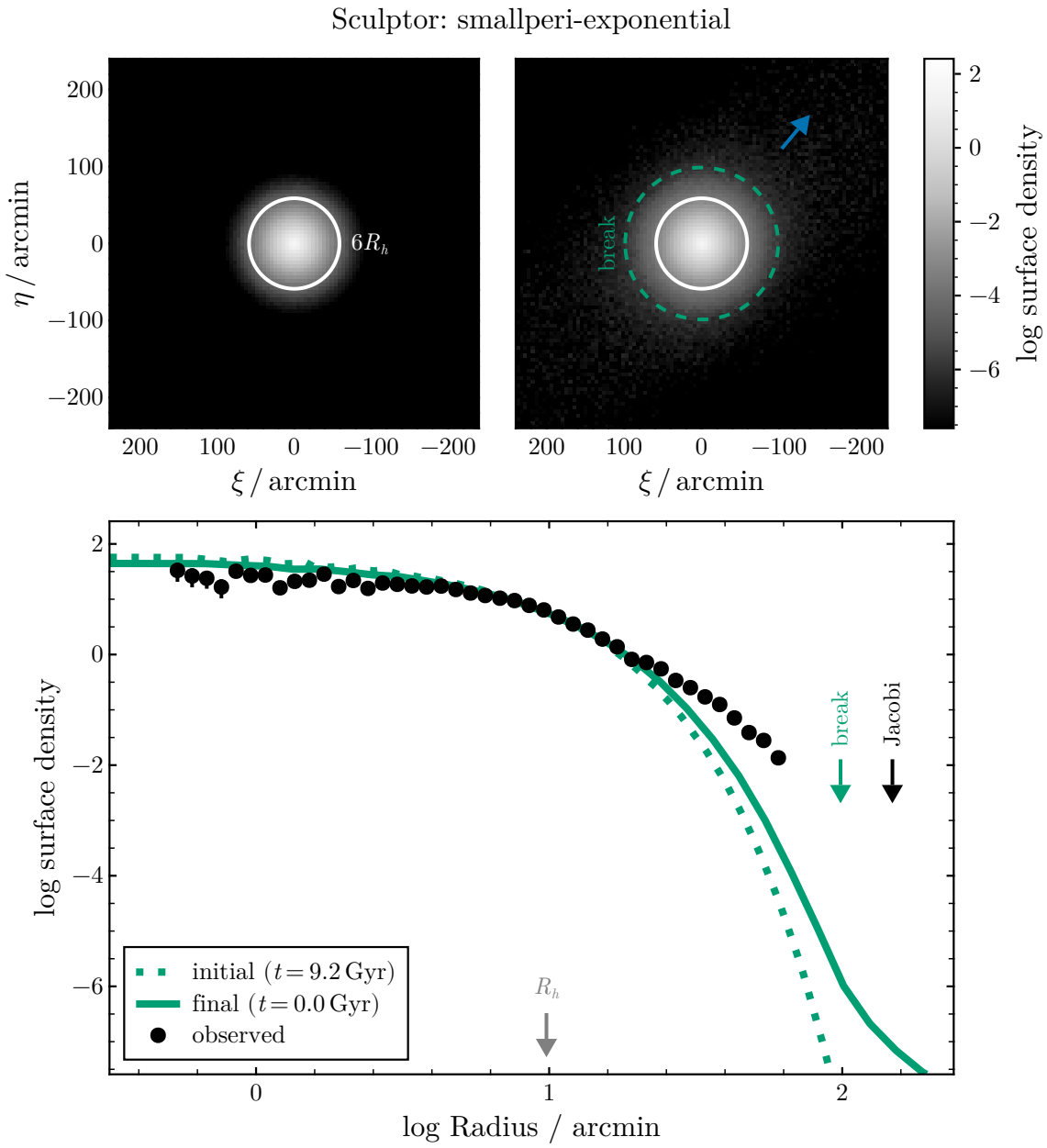

Figure 4.3: The tidal effects on Scl's stellar component, for the `smallperi` orbit with the fiducial halo and exponential stars with $R_s = 0.10$ kpc. **Top:** the initial (left) and final (right) 2D projected density of stars on the sky. The solid circle marks $6R_h$, the dotted circle the break radius, and the blue arrow the orbital direction. **Bottom:** The initial (dotted) and final (solid) stellar density profiles as compared to the observed stellar density profile (black points). Arrows mark the half-light (R_h), break, and Jacobi radii (Eqs. 1.8, 1.7) .

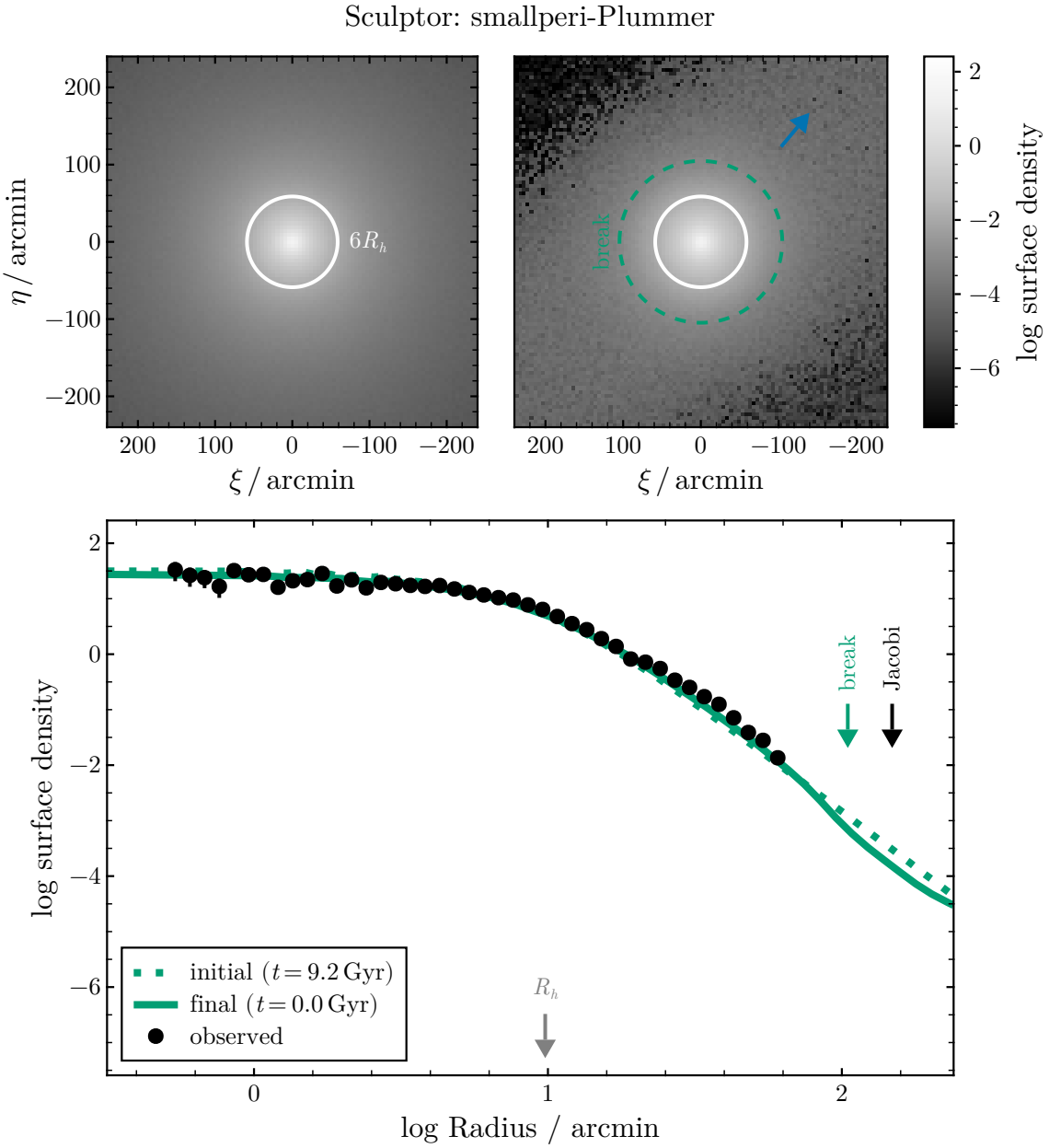

Figure 4.4: Similar to Fig. 4.3 except for Plummer initial stars with $R_h = 0.20$ kpc. While a faint stream may be visible with deeper observations, effects on the stellar profile are minimal.

4.1.3 Orbital effects of the LMC

The Milky Way isn't the only galaxy in town. Recently, work has shown that the infall of the LMC may substantially affect the Milky Way system (e.g., Erkal et al. 2019; Cautun et al. 2019; Garavito-Camargo et al. 2021; Vasiliev 2023). With a mass up to one fifth of the MW (e.g., Peñarrubia et al. 2015), the LMC infall affects the MW properties and the orbits of satellites (see e.g., Patel et al. 2020; Battaglia et al. 2022; Correa Magnus & Vasiliev 2022). In this section, we examine how the LMC may affect the orbital history of Sculptor.

We use the `L3M11` model of the MW and LMC potential from Vasiliev (2024). The `L3M11` potential is an evolving multipole approximation of an N-body simulation including a live MW and LMC dark matter halo. The potential includes a static MW bulge and disk, evolving MW and LMC halos, and the MW reflex motion. In their simulation, the MW was initially a NFW halo with $r_s = 16.5\,\mathrm{kpc}$ and $M_{200} = 98.4 \times 10^{10}\mathrm{M}_\odot$, and the LMC a NFW halo with $r_s = 11.7$ and $M_{200} = 24.6 \times 10^{10}\mathrm{M}_\odot$. The total `L3M11` MW mass is lighter than our initial Errani & Peñarrubia (2020) potential.

The inclusion of the LMC reshapes Scl's orbital history, as shown in Fig. 4.5. In the MW-only potential, Scl's orbit is typical of a long-term MW satellite. However, Scl's closest approach to the LMC $\sim 0.1\,\mathrm{Gyr}$ ago affects the long-term orbit—Scl is inferred to have reach an apocentre of nearly 300 kpc. According to this, Scl may be on first or second infall, depending on the MW and LMC mass.[1] Scl's is orbiting the Milky Way on a similar plane to the LMC, but in the opposite direction—thus, Scl is unlikely to be an LMC satellite.

Interestingly, the timing of the LMC encounter implies a break radius ($\sim 25'$, from Table 4.4) consistent with the beginning of Scl's observed density excess (see Fig. 2.5, and Section 2.3). To probe this further, we select an orbit with the smallest LMC-Scl pericentre (20 kpc) in the `L3M11` model, consistent with Scl's present-day position and velocity. The orbit is selected following the procedure in Section 3.1 (with uncertainties doubled). This `LMC-flyby` orbit is integrated back in time 2 Gyr ago to isolate recent tidal effects. We modify Scl's initial halo to have $r_{\mathrm{max}} = 2.5\,\mathrm{kpc}$ and $\mathrm{v}_{\mathrm{max}} = 25\,\mathrm{km\,s^{-1}}$, slightly reducing the initial stellar velocity dispersion. Fig. 4.5 shows this selected orbit in black and Table 3.1 records the initial conditions.

[1] The orbital periods may be $\gtrsim 7\,\mathrm{Gyr}$ for the lighter MW model, compared to $\sim 2\,\mathrm{Gyr}$ for the MW-only case

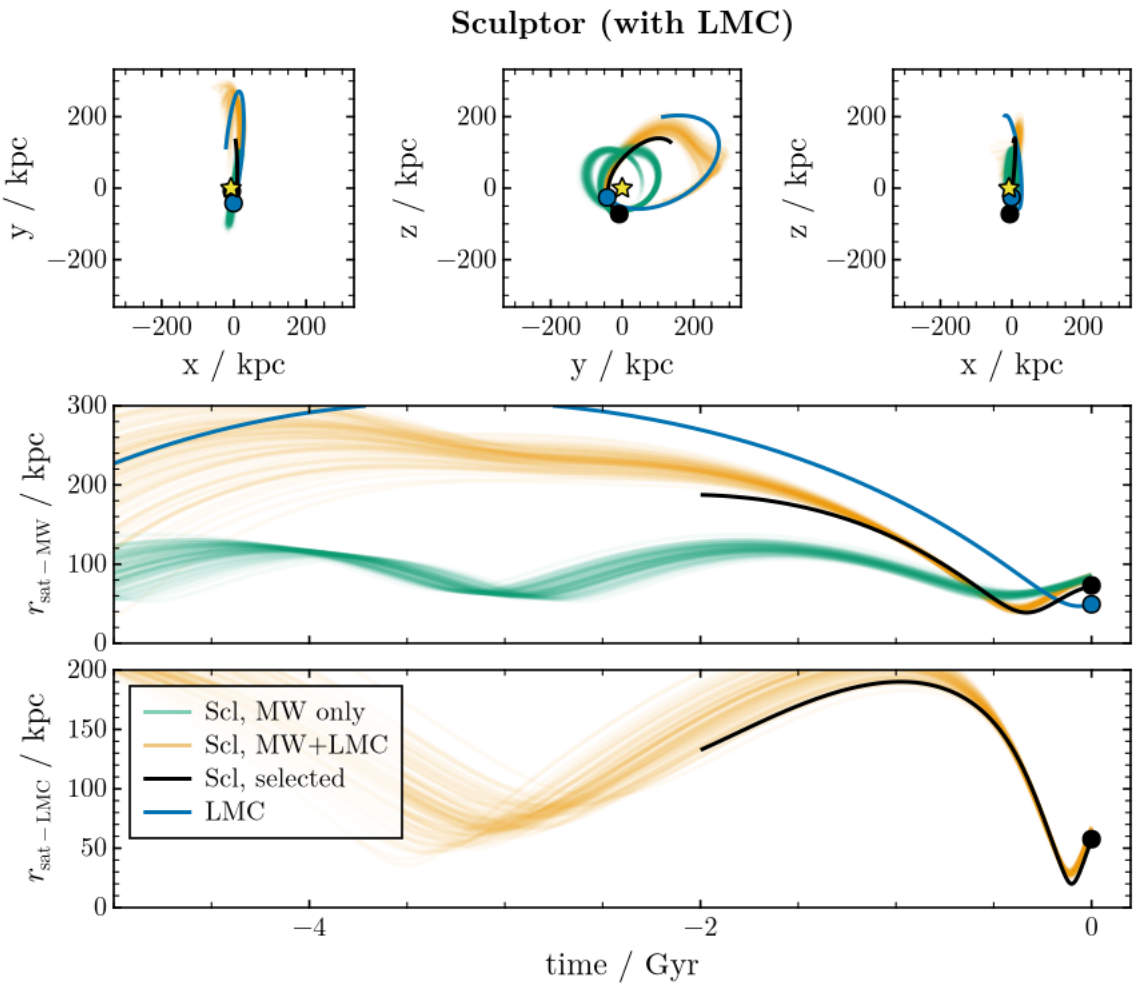

Figure 4.5: Similar to Fig. 3.2 except for orbits with (orange) and without (green lines) the inclusion of an LMC (blue line) in the potential. The bottom row additionally shows the distance between Scl and the LMC over time.

Table 4.3: The orbital properties and dark matter evolution for the models including an LMC. Similar to Table 4.1 except quantities with respect to the LMC are in parentheses.

Property	random samples	`LMC-flyby`
pericentre / kpc	44 ± 3 (29 ± 2)	39 (20)
apocentre / kpc	218 ± 8	–
time of last pericentre / Gyr	−0.38 ± 0.01 (−0.11)	−0.33 (−0.10)
number of pericentres	1 (1)	1 (1)
Jacobi radius / kpc	3.3 ± 0.2 (3.6 ± 0.2)	2.8 (2.6)
Jacobi radius / arcmin	136 ± 9 (159 ± 5)	132 (121)
final heliocentric distance / kpc	83.2 ± 2	72.9
$v_{\mathrm{max,\,f}}/v_{\mathrm{max,\,i}}$		0.928
$r_{\mathrm{max,\,f}}/r_{\mathrm{max,\,i}}$		0.763
fractional final bound mass		0.5402

4.1.4 Tidal effects of the LMC

Perhaps surprisingly, the combined tidal effect of the MW and LMC is weaker for Scl than in the MW-only case. Fig. 4.6 shows the dark matter evolution of Scl and the passage of the LMC. With only one MW pericentre, Scl's dark matter is less disrupted than in the previous MW-only model. The subsequent LMC passage modifies Scl's orbit but has otherwise little effect. The dark matter structure evolves mildly and $\sim$ 50% of mass remains bound (Table 4.3).

Correspondingly, the stellar component is nearly unchanged by the combined MW and LMC tides. Fig. 4.7 shows the projected stellar distributions and density profiles of this model. While the break radius is within the observed density profile, tidal effects are too weak to be detectable. Structural properties of the stars similarly evolve little (Table 4.4).

The reduced tides of the LMC-including model are likely a result of the altered orbit of Sculptor. Compared to the MW-only `smallperi` orbit, the `LMC-flyby` model completes fewer orbits and therefore experiences a reduced net tidal effect. And while the instantaneous tidal force from the LMC is larger than the MW, Scl does not experience the LMC tidal field long enough to display disturbances. Furthermore, the Jacobi radius due to the LMC still falls outside the observed density profile (Fig. 4.7), and the MW Jacobi radius is even larger. As a result, tides in an MW and LMC potential are even weaker overall than for the MW-only orbit.

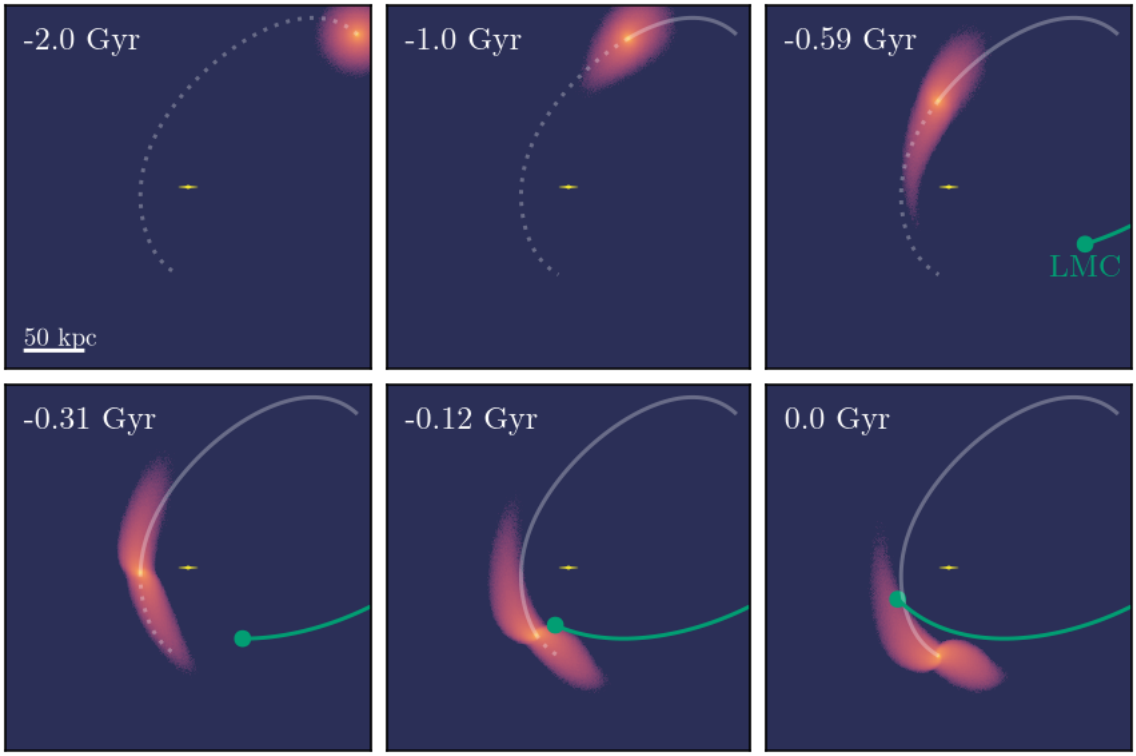

Figure 4.6: Similar to Fig. 4.1 for the case where the potential includes an LMC. The current position and path of the LMC are represented by the green dot and line, respectively. We also plot the full orbit (over the past 2Gyr) for both Scl and the LMC, as less than one radial period happens over this time frame.

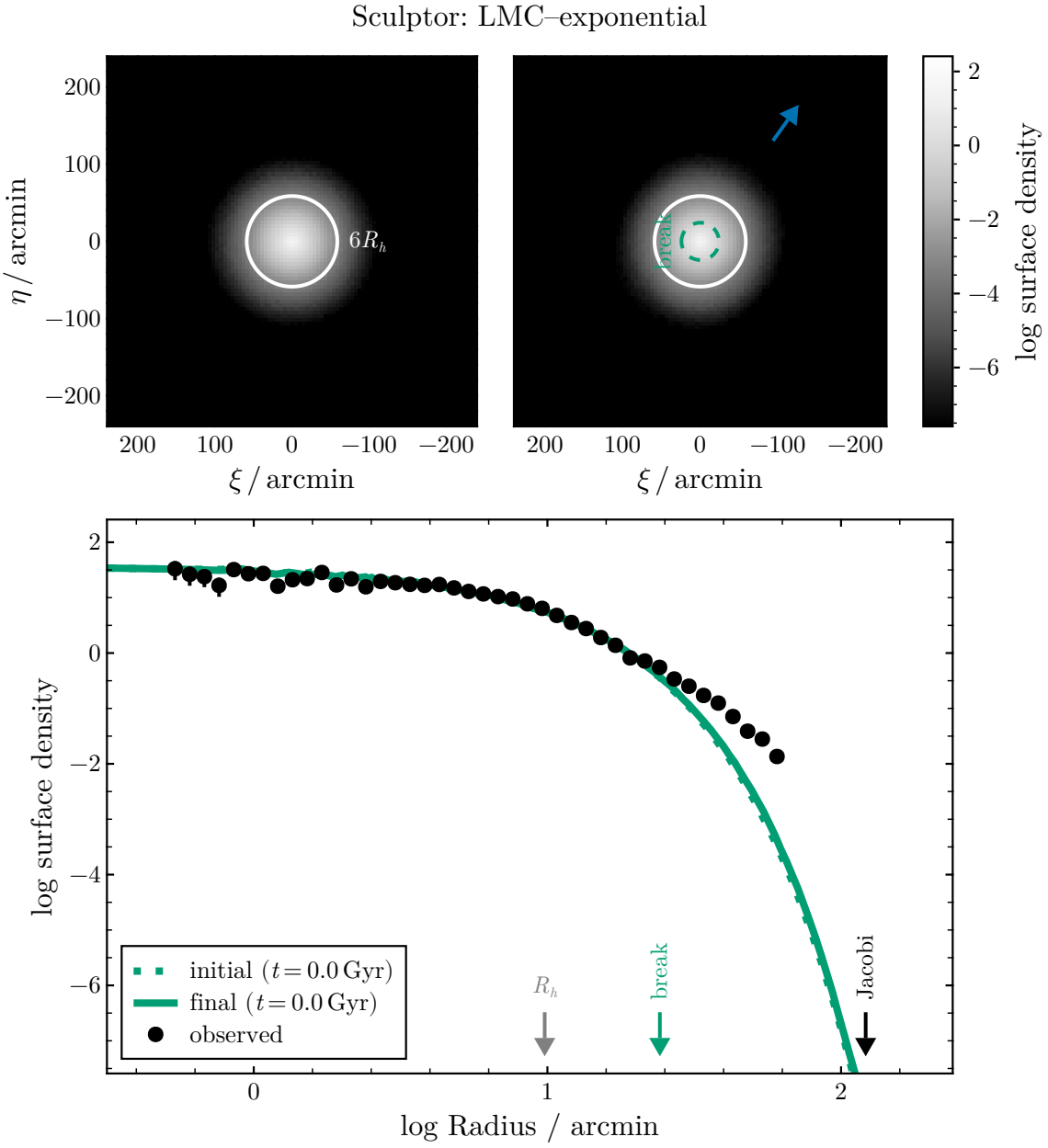

Figure 4.7: Similar to Fig. 4.3 for the `LMC-flyby` model. The Jacobi and break radii here are calculated with respect to the LMC; the corresponding radii with respect to the MW are larger. With only one MW pericentre and a recent, rapid LMC encounter, tidal forces do not appear to affect the stellar distribution.

Table 4.4: Similar to Table 4.2, but for the properties of the stellar components of the `LMC-flyby` model of Sculptor.

Property	Scl: LMC-exponential	LMC-Plummer
$\sigma_{\mathrm{v},i}$ / km s^{-1}	9.0	9.4
$\sigma_{\mathrm{v},f}$ / km s^{-1}	8.8	9.2
fractional stellar mass loss	$< 10^{-12}$	0.0013
$R_{h,i}$ / kpc	0.186	0.201
$R_{h,f}$ / kpc	0.189	0.205
break radius	78′, 1.6 kpc	81′, 1.7 kpc
LMC break radius	23′, 0.49 kpc	24′, 0.52 kpc

4.1.5 Summary

We find, including only the MW potential, that tides only remove dark matter from the outskirts of Scl. The central cusp and compact stellar distribution are resilient to tides. Any tidal effects are predicted to be well outside the reach of current observations. We have also found that the LMC strongly perturbs Scl's orbit—in this case, Scl may be on first infall. However, with only one pericentre each for the LMC and MW, the combined tides are weaker than for our initial model. In either case, we conclude that tides are unlikely to affect Sculptor's stellar component.

4.2 Tidal effects on Ursa Minor

4.2.1 Evolution of Ursa Minor's dark matter halo

The tidal evolution of Ursa Minor is similar to that of Sculptor in the MW-only potential. Fig. 4.8 shows snapshots of the DM evolution. UMi loses significantly more DM mass than Scl, forming substantial dark matter streams encircling the MW several times.

UMi only retains 3% of its total mass after 9 Gyr (Table 4.5). As a result, the final dark matter component is much smaller than the initial, but still evolves along the predicted tidal track (Fig. 4.9). Despite the more substantial tidal evolution, the Jacobi radius is still large, lying at ∼3 kpc, well beyond the final r_{max}.

Because of UMi's mass loss, the orbit deviates substantially from a point orbit. Through our orbit-adjustment procedure in Section 3.1.4, we recover nearly exactly the present-day position of Ursa Minor by changing the initial position and velocity by ∼20 kpc and ∼9 km s^{-1}.

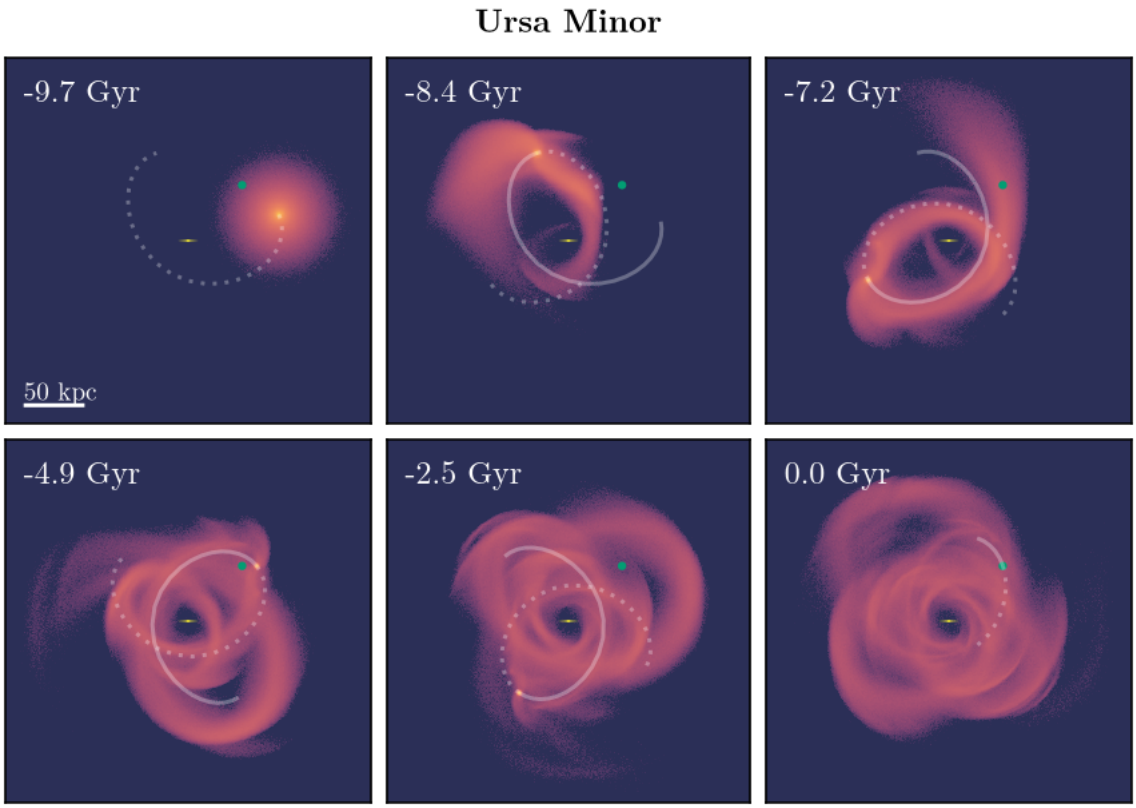

Figure 4.8: Similar to Fig. 4.1 but for Ursa Minor on the `smallperi` orbit. Dark matter evolution is more dramatic than for Sculptor.

Table 4.5: The present-day properties for Ursa Minor's final dark matter halo. See Table 4.1 for details.

Property	Random orbits	`smallperi`
pericentre / kpc	37 ± 3	30
apocentre / kpc	83 ± 4	75
time of last pericentre / Gyr	−0.96 ± 0.07	−0.80
number of pericentres	7–8	8
Jacobi radius / kpc	3.7 ± 0.3	2.9
Jacobi radius / arcmin	184 ± 12	156
final heliocentric distance / kpc	70.1 ± 3.6	64.7
$v_{\max f}/v_{\max i}$		0.511
$r_{\max f}/r_{\max i}$		0.249
fractional final bound mass		0.035

These adjustments do not significantly affect the qualitative structure or pericentre of the orbit.

4.2.2 Evolution of Ursa Minor's stars

Tidal features in UMi's stellar component are still extremely faint, becoming apparent only outside 100 arcminutes in Fig. 4.10. The observed size and velocity dispersion of Ursa Minor evolve little (Table 4.6). For exponential initial conditions, tidal effects are unlikely to be observable in the near future.

The break and Jacobi radii fall well outside the observed stellar profile. Tides would have to be far stronger to affect the observed stellar component. As a result, the minimal tidal evolution of this model is not unexpected.

As for Scl (Section 4.1.2), we also consider a model where UMi's stars follow initially a Plummer profile, resembling the present-day density profile. The stellar evolution of this Plummer stellar component is similar (Fig. 4.11). Because there are more loosely-bound stars, the Plummer model loses nearly 7% of its initial stellar mass to tides (Table 4.6). Tidal features may be detectable if we measure densities 2 orders of magnitude fainter than our present data. We show the properties of a stream in the Appendix (Fig. D.10), but such a stream is unlikely to be observable in the near future. We conclude that tides do not strongly affect the stellar component of this model.

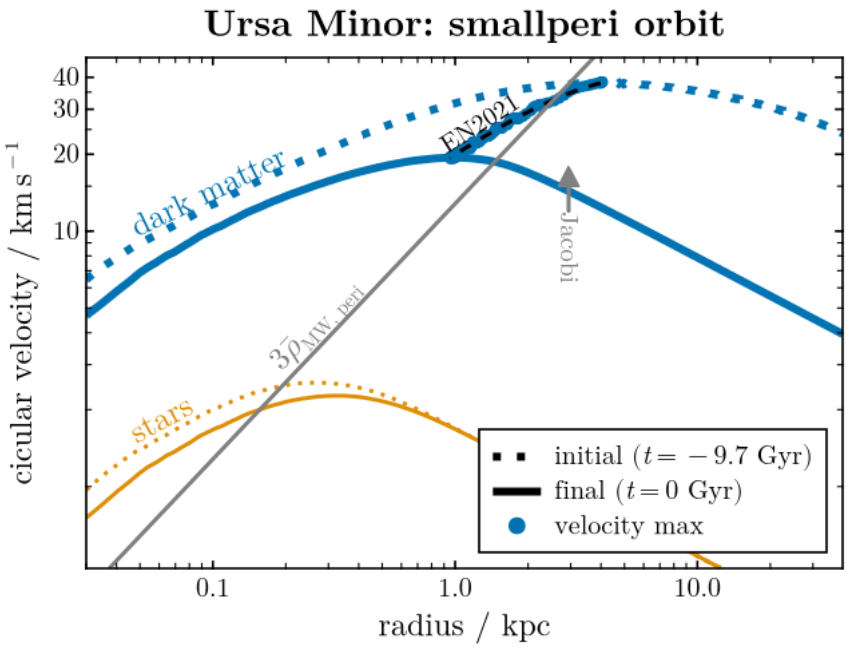

Figure 4.9: Similar to Fig. 4.2 except for Ursa Minor. Ursa Minor loses substantially more mass than Sculptor.

4.2.3 Effects of the LMC

Fig. 4.12 shows the effects of including an LMC on the orbit of Ursa Minor. Predominantly, the orbital period, apocentre, and pericentre all increase. Yet, the orbit remains in a similar plane and with similar shape to the MW-only case. As UMi is on the opposite side of the Galaxy of the LMC and has a closest LMC approach of $\gtrsim 100$ kpc, this is not surprising.

The deviation from the MW-only orbit is mostly due to the LMC-induced reflex motion of the Milky Way. Because the MW centre is accelerated towards the LMC and away from UMi, UMi's orbit increases in characteristic radius.

4.2.4 Summary

While tides affect UMi more strongly than Scl, the tidal effects are insufficient to reshape the observed stellar density profile. Faint tidal tails may be observable with deeper data. Finally, including the LMC in the potential further weakens the tides experienced by UMi.

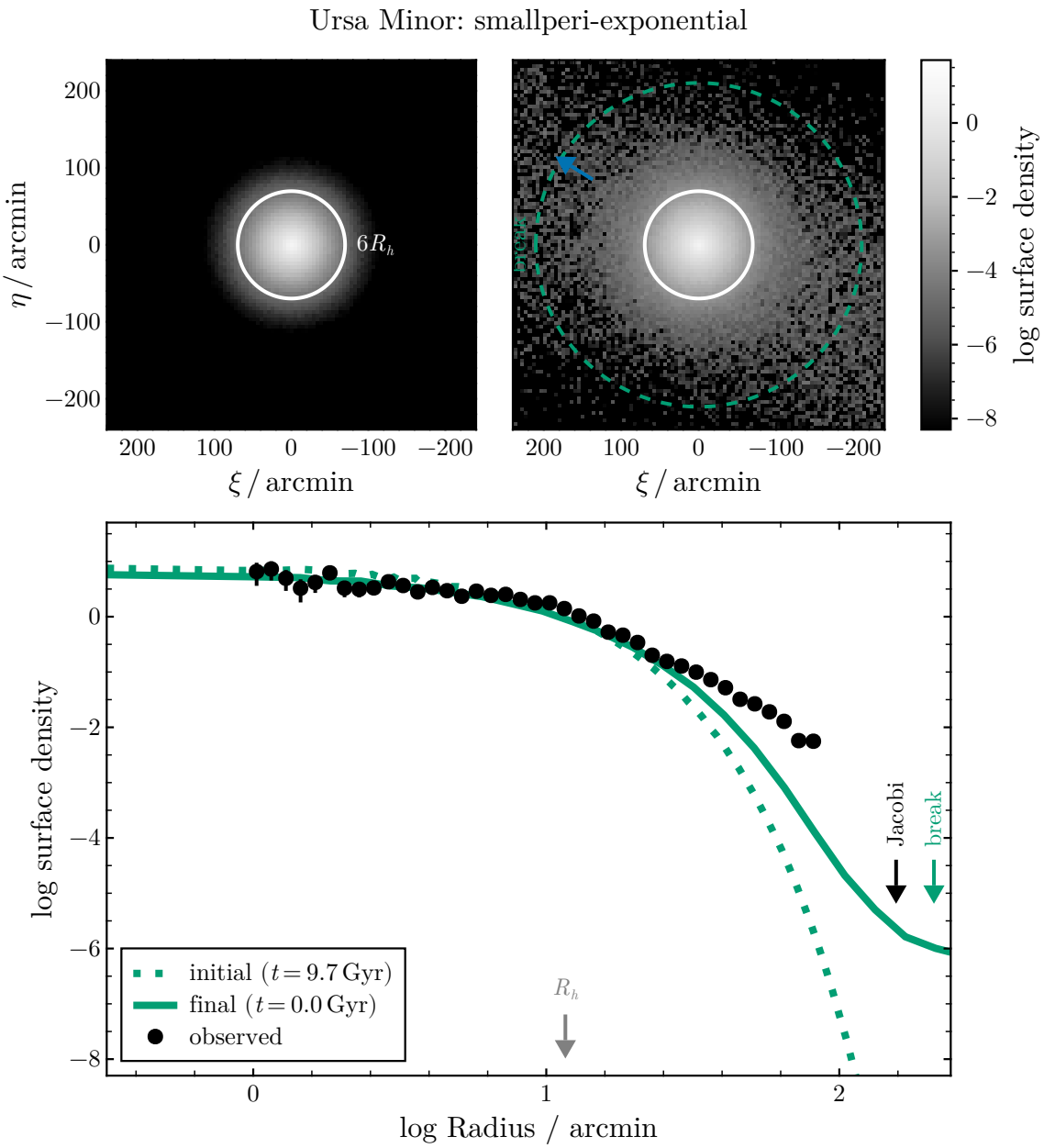

Figure 4.10: Similar to Fig. 4.3: the tidal effects on the stellar surface density of Ursa Minor for exponential stars on the `smallperi` orbit.

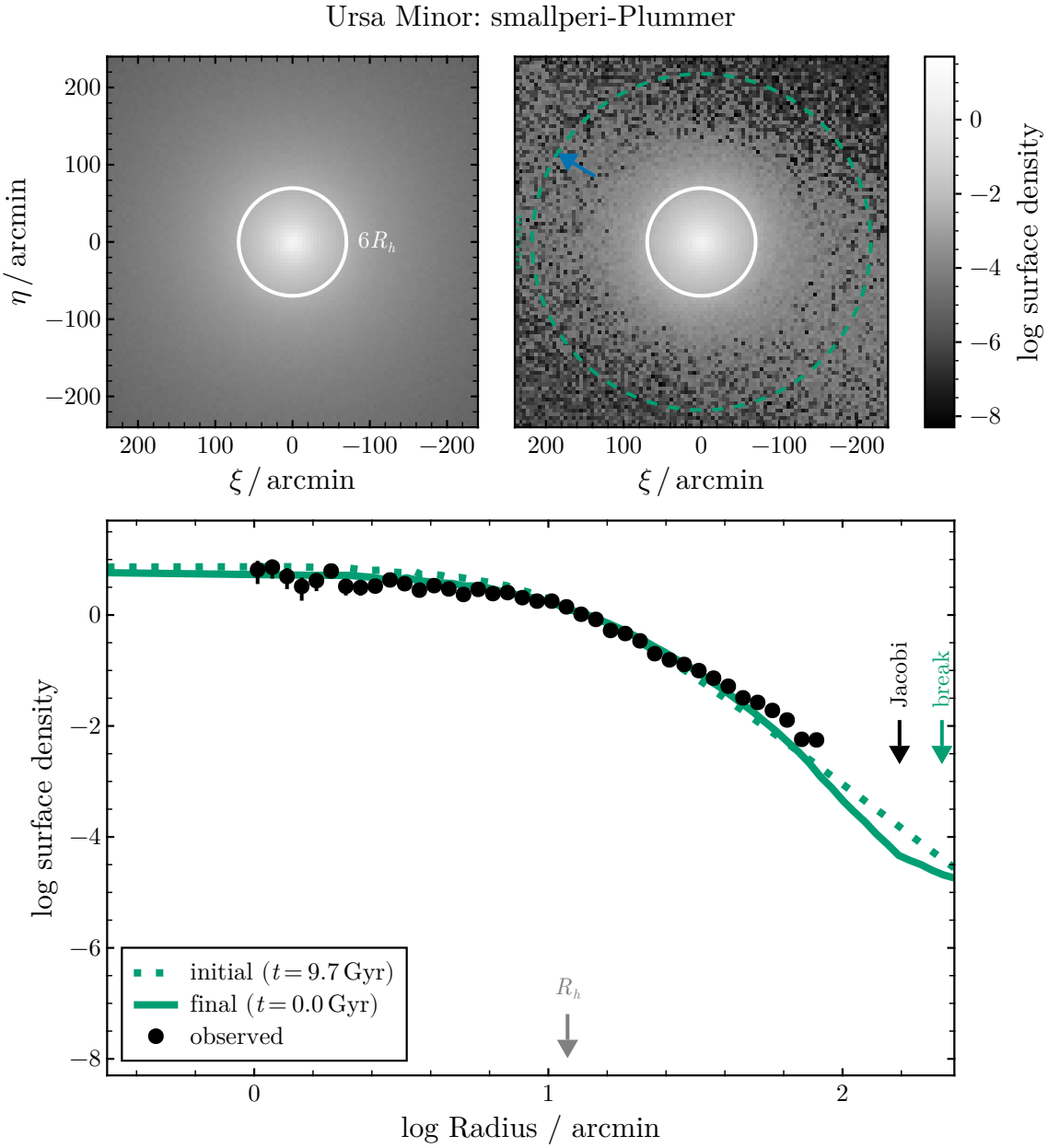

Figure 4.11: Similar to Fig. 4.3: the tidal effects on the stellar surface density of Ursa Minor for Plummer stars on the `smallperi` orbit.

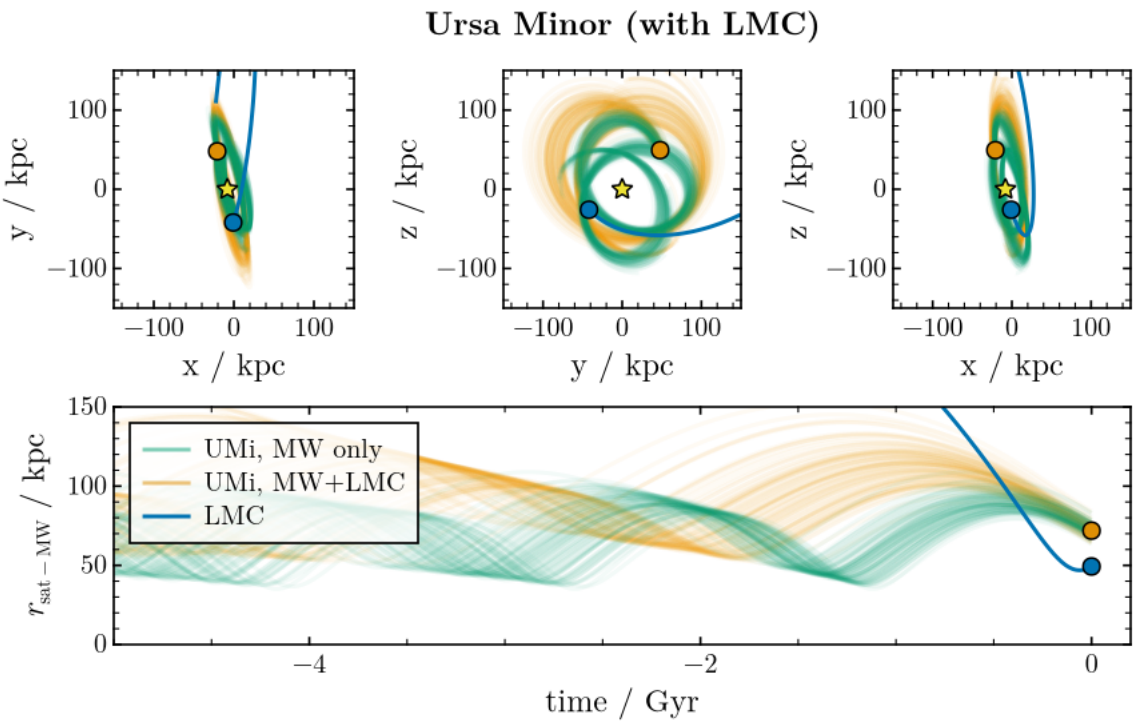

Figure 4.12: Orbits of Ursa Minor with (orange) and without (green) an LMC. The final positions of Ursa Minor and the LMC are plotted as scatter points, and the solid blue line represents the LMC trajectory. Note that the LMC mostly increases Ursa Minor's pericentres and apocentres.

Table 4.6: Similar to Table 4.2, the present-day stellar properties for the simulation of Ursa Minor for exponential and Plummer stars.

Property	`smallperi-exp`	`smallperi-Plummer`
$\sigma_{\mathrm{v},i}$ / km s^{-1}	11.0	12.1
$\sigma_{\mathrm{v},f}$ / km s^{-1}	8.8	9.1
fractional stellar mass loss	0.00138	0.068
$R_{h,i}$ / kpc	0.201	0.20
$R_{h,f}$ / kpc	0.212	0.257
break radius	210 arcmin, 4.0 kpc	218 arcmin, 4.1 kpc

4.3 Modelling uncertainties

4.3.1 Halo structure

As the above results show, tides only marginally affect the stellar components of Scl and UMi, even with orbits chosen to have the smallest observationally-consistent pericentres. While we have only presented select models, alternative initial conditions do not affect our qualitative conclusions on tidal effects expected for Scl and UMi in the Galactic (and LMC) potential.

Although our analysis neglects baryonic physics, Scl and UMi have predominantly stars older than ~ 9 Gyr (Carrera et al. 2002; de Boer et al. 2011; Weisz et al. 2014; de los Reyes et al. 2022; Sato et al. 2025). So, gas dynamics are unlikely to affect recent evolution. A collisionless dark-matter-only simulation should therefore be an excellent approximation.

Cored or less concentrated dark matter halos disrupt quicker (e.g., Stücker et al. 2023). Our fiducial UMi halo, in particular, is among the least concentrated halos consistent with UMi's velocity dispersion. Although Scl's fiducial halo is more concentrated, less concentrated and cored halos evolve similarly (see Appendix D).

Galaxies are rarely perfect isotropic spheres. Sculptor and Ursa Minor are elliptical, and halos are expected to be radially anisotropic (e.g., Navarro et al. 2010). We test non-spherical and anisotropic models in Appendix D, finding that these assumptions likely do not alter our conclusions.

While alternative initial conditions may influence the total mass evolution, they should produce a similar final stellar structure. A system's observed velocity dispersion directly constrains the mean density within R_h (e.g., Wolf et al. 2010). Thus, the tidal force required

to disrupt the stellar component depends mainly on the total mass inside the half-light radius, and less on the inner density profile shape.

4.3.2 Orbital uncertainties

The long-term orbital evolution of satellites are uncertain. Analytic Milky Way potentials neglect many unknown details, including triaxiality, mass evolution, and substructure. Due to these inadequacies, calculated orbits may diverge significantly from the true orbits of satellites (e.g., D'Souza & Bell 2022). Dynamical friction and the mass-growth of the Milky Way both imply that orbits were typically less bound in the past. Orbital energy and angular momentum of subhalos are also not conserved in cosmological N-body simulations. Consequently, orbits in analytic potentials may overestimate the pericentre and underestimate the maximum tidal stress (although typically not by enough to change our conclusions, Santistevan et al. 2023, 2024).

As an example, Fig. 4.13 illustrates how changes to the LMC potential modify the long-term orbital trajectories of Scl and UMi. More than 4 Gyr ago, the orbits of Scl diverge substantially. Some orbits are near apocentres of ~ 300 kpc when others approach pericentres as small as ~ 10 kpc. Ursa Minor's orbit is more stable until the possible previous LMC pericentre. In some cases, Ursa Minor may have been bound to the LMC.

Motivated by Fig. 4.13, we examine an extreme pericentre of 4 kpc of Scl with the MW in Appendix D, finding it still insufficient to produce the observed density profile. Regardless, we conclude our simulated orbits represent reasonable extremes for *recent* tidal effects. Past encounters with the LMC are revisited below as a form of "pre-processing" in Section 5.2.

4.3.3 Summary

While the long-term tidal evolution is unconstrained, we conclude that our models are reasonable representations of recent tidal effects. As a result, recent tides are unlikely to affect the stellar distributions of Sculptor and Ursa Minor.

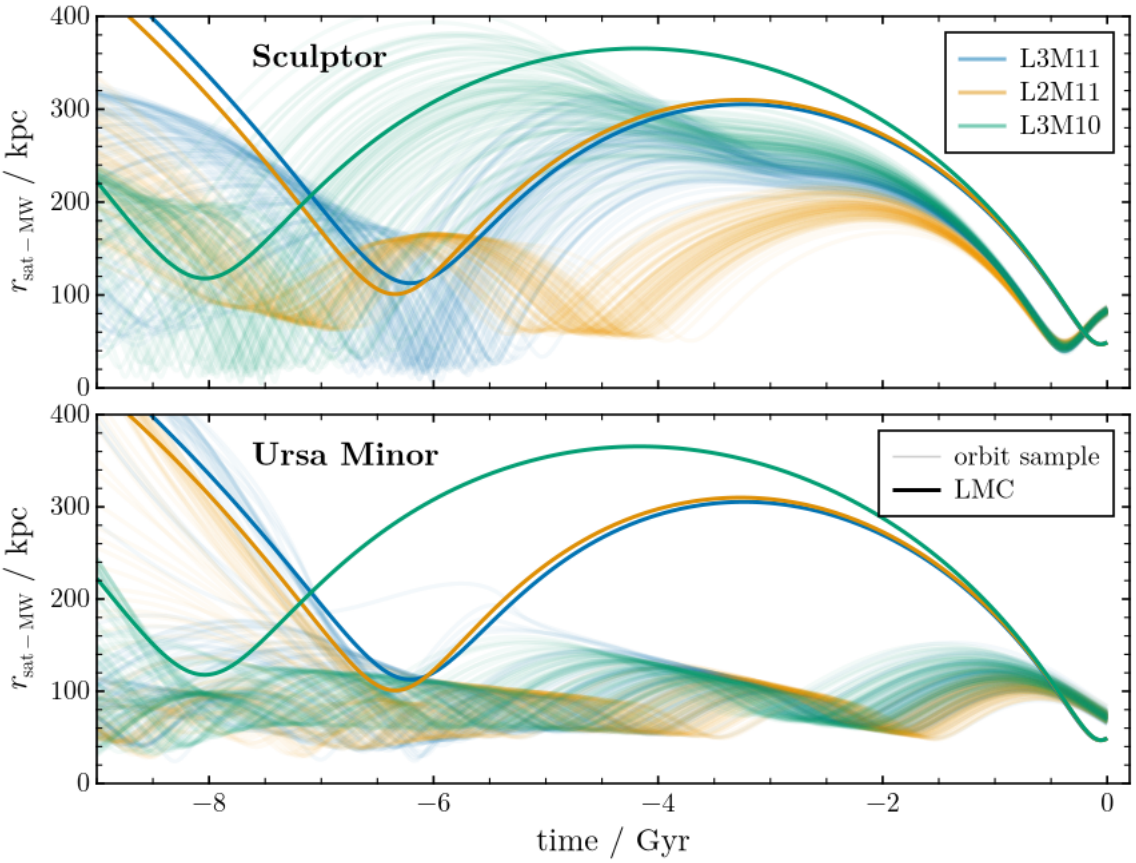

Figure 4.13: The long-term orbital history of Sculptor (**top**) and Ursa Minor (**bottom**) is uncertain. In both panels, light, transparent lines represent randomly sampled orbits of the satellites (following Section 3.1.3) in three different LMC/MW mass models from Vasiliev (2024). The LMC orbits are in solid, thick lines of the corresponding colour. The `L2M11` has a lighter LMC mass, and the `L3M10` model has a lighter MW mass than our fiducial `L3M11` LMC model.

5. Discussion & Conclusions

In the previous chapters, we have shown that Sculptor and Ursa Minor have more extended density profiles compared to other MW classical satellites, and that recent tides are an unlikely explanation for their extended outer structure. We therefore suggest Scl and UMi host an additional, extended population of stars, such as a "stellar halo." With our data, other classical dwarfs lack evidence for similar extended populations. Thus, Scl and UMi have followed a divergent evolutionary path, motivating our following discussion of extended density formation pathways here.

In this chapter, we compare our results to past work and interpretations. We first review studies considering tidal effects on Scl and UMi and detections of peculiarities. We then consider possible origins of extended stellar populations in these galaxies. Scenarios include multi-epoch star formation, past mergers depositing stars into the outskirts, and even departures from ΛCDM. We later discuss how future studies may distinguish formation scenarios. Finally, we summarize the main conclusions of this thesis.

5.1 Comparison with prior work

5.1.1 The role of tides

Tidal effects have long been invoked to explain features of dwarf galaxies (e.g., Section 1.3.4, Mayer et al. 2001; Tsujimoto & Shigeyama 2002). Yet, a growing body of work suggests tides may not be as commonplace as suspected. For example, Read et al. (2006) suggested that the absence of rising radial velocity dispersion profiles in dwarfs implies a lack of tidal disruption. Peñarrubia et al. (2009), introducing the break radius as a diagnostic (Eq. 1.8), showed that most satellite orbits were inconsistent with observable tidal effects. Recently, Pace et al. (2022) used a Jacobi radius-based criterion (Eq. 1.7) to reach a similar conclusion. Except for the Sagittarius dSph, these results suggest tides have a mild influence on the stellar components of classical dwarfs.

A few studies have modelled Sculptor or Ursa Minor specifically, finding similar conclusions. Iorio et al. (2019) applied idealized N-body simulations to study tidal effects on Scl.

They similarly found weak tidal effects, even for a dark-matter-free model. Most recently, Tchiorniy & Genina (2025) also used idealized simulations tuned to five classical dwarfs with a focus on the inner density, concluding that tides do not strongly affect equilibrium assumptions or the stellar component.

Our work extends these models, adding updated structural properties, a broader range of orbital histories, and the influence of the LMC. Despite these considerations, we still reach similar conclusions: tidal effects do not shape Scl or UMi's stellar component. A non-tidal process likely underlies the origin of these galaxies' outer density excess.

5.1.2 Peculiarities in the galaxies

Besides their extended stellar density profiles, Sculptor and Ursa Minor display other peculiarities that may hold clues to their formation. Scl and UMi both host at least two distinct chemodynamic populations, as revealed through their photometric or metallicity-velocity structure[1] (Tolstoy et al. 2004; Battaglia et al. 2008; Pace et al. 2020). The inner population is younger, higher metallicity, and dynamically colder, whereas the outer population is older, lower metallicity, and dynamically hotter.

Could these internal stellar populations map to the observed density excess? In Scl, both populations have scale radii likely smaller than the half-light radius. However, a third, more tentatively detected population in Arroyo-Polonio et al. (2024) would reside within the outer density excess. In Ursa Minor, the transition between the metal-rich and metal-poor stellar components occurs at ∼30 arcmin (Pace et al. 2020), which coincides with our density excess. This metal-poor population may thus be related to the extended stellar density of Ursa Minor.

Fig. 5.1 shows the radial metallicity distribution in both galaxies. To aid in comparison, we fit a 2-component exponential to the density profiles. We also mark where the densities of each component become equal, the "transition" radius. Scl and UMi both show evidence of a metallicity gradient. But, the relation between the metallicity gradient and the transition from the inner to the outer density profile is unclear. UMi also has few measurements past the transition radius. Further observations would be necessary to understand if the extended stellar component represents a chemically distinct population.

Ursa Minor has also shown evidence for possible inner substructure, such as stellar or

[1]Other examples of galaxies with multiple populations include Carina (Battaglia et al. 2012; Fabrizio et al. 2016; Kordopatis et al. 2016), Fornax (Battaglia et al. 2006; Amorisco & Evans 2012; del Pino et al. 2015), Sextans (Battaglia et al. 2011; Cicuéndez & Battaglia 2018; Roederer et al. 2023), and Andromeda II (McConnachie et al. 2007; Ho et al. 2012; del Pino et al. 2017).

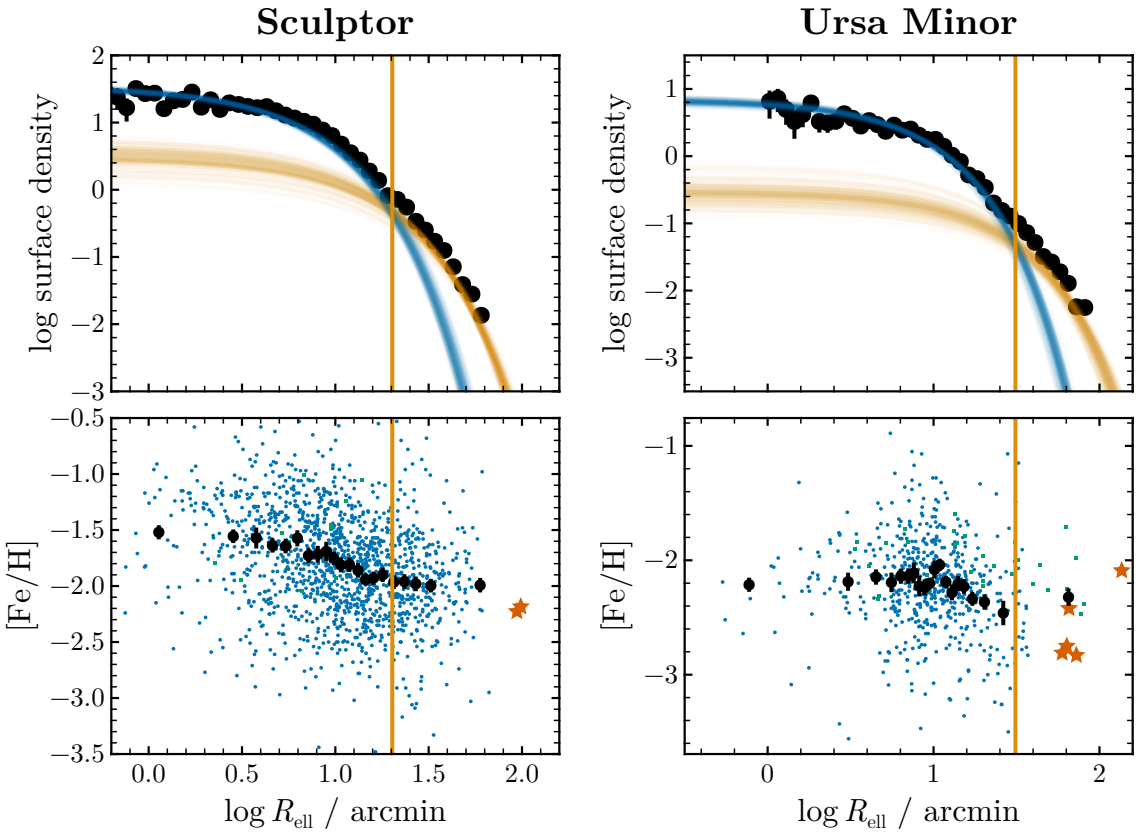

Figure 5.1: Density profiles and metallicity gradients in Scl (left) and UMi (right). **Top**: Black points show the J+24 density profiles as a function of elliptical radius, and transparent lines represent the two components of a double-exponential density fit. The vertical lines represent the transition from the inner to the outer exponential profile. **Bottom**: Metallicities as a function of elliptical radius for stars crossmatched against J+24 as described in Appendix B. Larger, red stars show the members from Sestito et al. (2023a,b).

kinematic "clumps" (e.g., Olszewski & Aaronson 1985; Demers et al. 1995; Kleyna et al. 1998; Battinelli & Demers 1999; Bellazzini et al. 2002). While one clump was re-detected kinematically in Pace et al. (2014), Muñoz et al. (2018) find no evidence of substructure with modern photometry. In any case, the survival of a cold clump depends on the inner structure of the halo, disrupting quickly in halos with substructure or inner density cusps but surviving longer in smooth, cored halos (Kleyna et al. 2003; Lora et al. 2012).

The multiple chemical populations and possible inner structure of Sculptor and Ursa Minor may represent the signatures of the unusual assembly histories that produced the dwarfs' extended stellar densities.

5.2 Forming an extended stellar population

As we disfavour a tidal origin for Scl and UMi's extended density profiles, we now consider six other processes that may form an extended stellar population in these dwarfs.

Episodic star formation. Star formation may quench and reignite, creating successive stellar generations with differing distributions. External star formation triggers include tidal compression (Mayer et al. 2001; Dong et al. 2003), collisions with gaseous filaments (Genina et al. 2019), perturbations from dark halos (Starkenburg et al. 2016), or shocks with the MW corona (Wright et al. 2019). More common mechanisms, like feedback or reionization-driven quenching, may also form multiple stellar generations (Kawata et al. 2006; Benítez-Llambay et al. 2015; Revaz & Jablonka 2018). However, such processes would not explain why extended stellar populations appear to be non-universal. If an extended population was formed during a separate star formation event, then the star formation history should contain evidence of a corresponding burst.

Major mergers. Dwarf galaxy mergers may be relatively common (Deason et al. 2014). After a merger, stars from the lower-mass galaxy are preferentially dispersed, forming an extended stellar component and population gradient (Benítez-Llambay et al. 2016; Deason et al. 2022). If the galaxies contain gas, the merger can also trigger new star formation, forming a younger population of stars (e.g., Genina et al. 2019). A few local dwarfs are suspected to have undergone a major merger, including Sextans, Tucana II, Andromeda II, and Phoenix (Lokas et al. 2014; Fouquet et al. 2017; Cicuéndez & Battaglia 2018; Tarumi et al. 2021; Cardona-Barrero et al. 2021; Querci et al. 2025). A galaxy having undergone a major merger should harbour at least two or three populations with distinct origin.

Just as the Milky Way's halo is likely built from many minor mergers, dwarf galaxies may have built accreted "stellar halos" composed of even fainter satellites (Ricotti et al.

2022). Few examples of dwarf-dwarf accretion are known, but a possible stream around And II or chemical peculiarities around Sextans I may be such instances (Amorisco et al. 2014a; Roederer et al. 2023). In this scenario, the extended stellar populations would contain chemical signatures from several distinct ultra-faint dwarf galaxies.

Tidal preprocessing. Some dwarf galaxies may have been tidally "preprocessed" by a massive satellite like the LMC (e.g., Santistevan et al. 2023; Riley et al. 2024). Tidal preprocessing redistributes already-present stellar populations and may mimic a stellar halo. Key evidence suggestive of preprocessing may include distant dwarf stars or stellar streams.

Dark-matter-free dwarfs. Tidal dwarfs are galaxies that formed in gas-rich tidal streams during the merger of two larger galaxies (e.g., Mirabel et al. 1992; Bournaud & Duc 2006). Without a dark matter halo, tidal dwarfs may be more susceptible to tides, forming extended density profiles and inflating the velocity dispersion (Casas et al. 2012; Yang et al. 2014; Wang et al. 2024).

Similarly, in Modified Newtonian Dynamics (MOND), galaxies do not contain dark matter. Instead, the gravitational force law is altered to explain rotation curves. Dwarfs would similarly experience stronger tidal effects in MOND (McGaugh & Wolf 2010; Brada & Milgrom 2000).

In both cases, tides more plausibly produce extended density profiles. However, recovering the observed velocity dispersions often requires ongoing tidal disruption (McGaugh & Wolf 2010; but see also Sánchez-Salcedo & Hernandez 2007). Current data do not show evidence of such features (see Appendix B)—future data would be needed to uncover signs of disruption to support this hypothesis.

Dynamical heating. Old stars in dwarf galaxies may be dynamically hotter than younger stars due to processes including stellar feedback (Stinson et al. 2009; Maxwell et al. 2012; El-Badry et al. 2016; Mercado et al. 2021), sub-subhalo interactions (Peñarrubia et al. 2025), or even fuzzy dark matter interference fringes (e.g., El-Zant et al. 2020; Dutta Chowdhury et al. 2023). However, most of these processes should operate similarly across dwarf galaxies—extended stellar populations should be more common if these processes are important.

5.3 Disentangling the origin of extended stellar populations

We have reviewed a number of different, possibly concurrent explanations for the formation of extended populations. While we leave the nature of Scl and UMi's extended stellar densities an open question, we can discuss possible clues to different formation scenarios.

Precise chemistry. Chemical abundances, comparing the inner and outer regions, can

test if the halo was formed within the dwarf or accreted. If external in origin, chemistry could reveal the properties of any past mergers.

Detailed kinematics. For models relying on recent tidal disruption, kinematic disequilibrium features should be visible. These would appear as velocity gradients, increasing velocity dispersions, outward-biased moving stars, or non-phase mixed structures (e.g, Kroupa 1997; Read et al. 2006; Sánchez-Salcedo & Hernandez 2007). In addition, measurements of the ellipticity and anisotropy would help verify or alter our understanding of the mass structure and whether DM-free models may be permissible.

Deep photometry may find or rule out signs of dynamical disequilibrium and tidal tails for tidally susceptible models (e.g., *pre-processing* and *DM-free dwarfs*). In addition, photometry will help constrain the prevalence and nature of extended features in dwarf galaxies.

Star formation histories can be derived through photometry or chemistry. Evidence of significant star formation episodes or lack thereof may differentiate scenarios that rely on strong star formation bursts (e.g., *episodic star formation history, induced star formation,* and *gas-rich mergers*).

Ongoing and future observational surveys will be instrumental for testing dwarf galaxy halo formation. Because dSph stars are usually faint, detailed chemical analysis will rely on medium–high resolution multi-object spectroscopy on large telescopes, such as 4MOST (Skúladóttir et al. 2023) or the extremely large telescope (Jagourel et al. 2018). Mapping the 3D kinematics across a dwarf may require a *Gaia* successor, but ongoing surveys with JWST and HST can derive precise proper motions within select regions of dwarf galaxies, reconstructing internal structure and anisotropies (e.g., Vitral et al. 2025). Current wide-field photometric surveys by the Rubin Observatory (Ivezić et al. 2019) and *Euclid* (Euclid Collaboration et al. 2025) will trace even fainter features around dwarf galaxies, possibly finding halos, tidal streams, and unusual stellar populations. Together, these observational programs promise a new window into the detailed structure, evolution, and outskirts of dwarf galaxies.

The next generation of dwarf simulations will likewise continue to refine our understanding of dwarf galaxy formation. Notable recent simulation projects include EDGE (Agertz et al. 2020) and LYRA (Gutcke et al. 2021), both of which can simulate the cosmological formation of isolated dwarf galaxies while resolving individual (massive) stars. Next steps for simulations include improved realism (e.g., magnetic fields), refining physical models (including feedback and star formation), and improving numerical resolution. With these continuing advances, future simulations may shed light on the viability of extended stellar population formation scenarios and the details of dwarf galaxy assembly.

5.4 Conclusion and outlook

In this thesis, we have investigated the extended, outer density excess of Sculptor and Ursa Minor and its possible tidal origin. We have shown that the density profiles are robust, implying that Scl and UMi contain a true density excess relative to other classical dwarfs.

We then investigated whether tides are a possible explanation. By modelling each galaxy based on cosmological initial conditions, we showed that tides do not strongly affect either galaxy. The LMC changes the orbital history of Scl and UMi, but tides become even weaker in a combined LMC and MW potential. We conclude that recent tides are unlikely to shape the outer radial distribution of stars in Scl and UMi.

Finally, we discuss the implications of a non-tidal density excess in Scl and UMi. We review mechanisms ranging from episodic star formation histories, to accretion, to departures from ΛCDM. Future simulations and observational programs will be able to investigate the nature of dwarfs with ever-increasing detail. Abundant opportunities await to uncover the cosmic origins of dwarf galaxies, the building blocks of galaxies like ours.

Research Acknowledgments

This work used the DiRAC@Durham facility managed by the Institute for Computational Cosmology on behalf of the STFC DiRAC HPC Facility (www.dirac.ac.uk). The equipment was funded by BEIS capital funding via STFC capital grants ST/K00042X/1, ST/P002293/1, ST/R002371/1 and ST/S002502/1, Durham University and STFC operations grant ST/R000832/1. DiRAC is part of the National e-Infrastructure.

Computations were performed on the Niagara supercomputer (Ponce et al. 2019) at the SciNet HPC Consortium (Loken et al. 2010). SciNet is funded by Innovation, Science and Economic Development Canada; the Digital Research Alliance of Canada; the Ontario Research Fund: Research Excellence; and the University of Toronto.

This work has made use of data from the European Space Agency (ESA) mission *Gaia* https://www.cosmos.esa.int/gaia), processed by the *Gaia* Data Processing and Analysis Consortium (DPAC), https://www.cosmos.esa.int/web/gaia/dpac/consortium. Funding for the DPAC has been provided by national institutions, in particular the institutions participating in the *Gaia* Multilateral Agreement.

This work has made use of software including Jupyter, astropy, TOPCAT, Makie, Turing, and Pluto.

Bibliography

Aaronson, M. 1983, ApJ, 266, L11, doi: 10.1086/183969

Aaronson, M., & Olszewski, E. 1987, in Dark Matter in the Universe, Vol. 117, 153. https://ui.adsabs.harvard.edu/abs/1987IAUS..117..153A

Abbott, T. M. C., Adamów, M., Aguena, M., et al. 2021, Astrophys. J. Suppl. Ser., 255, 20, doi: 10.3847/1538-4365/ac00b3

Abdurro'uf, Accetta, K., Aerts, C., et al. 2022, 259, 35, doi: 10.3847/1538-4365/ac4414

Adams, J. J., Simon, J. D., Fabricius, M. H., et al. 2014, ApJ, 789, 63, doi: 10.1088/0004-637X/789/1/63

Agertz, O., Pontzen, A., Read, J. I., et al. 2020, MNRAS, 491, 1656, doi: 10.1093/mnras/stz3053

Agnello, A., & Evans, N. W. 2012, ApJ, 754, L39, doi: 10.1088/2041-8205/754/2/L39

Amorisco, N. C. 2021, Cold Dark Matter Subhaloes at Arbitrarily Low Masses, arXiv, doi: 10.48550/arXiv.2111.01148

Amorisco, N. C., & Evans, N. W. 2012, ApJ, 756, L2, doi: 10.1088/2041-8205/756/1/L2

Amorisco, N. C., Evans, N. W., & van de Ven, G. 2014a, Nature, 507, 335, doi: 10.1038/nature12995

Amorisco, N. C., Zavala, J., & de Boer, T. J. L. 2014b, ApJ, 782, L39, doi: 10.1088/2041-8205/782/2/L39

An, Z., & Koposov, S. E. 2022, MNRAS, 511, 4316, doi: 10.1093/mnras/stac308

Antoja, T., Helmi, A., Romero-Gómez, M., et al. 2018, Nature, 561, 360, doi: 10.1038/s41586-018-0510-7

Aparicio, A., Dalcanton, J. J., Gallart, C., & Martinez-Delgado, D. 1997, AJ, 114, 1447, doi: 10.1086/118575

Arroyo-Polonio, J. M., Battaglia, G., Thomas, G. F., et al. 2024, A&A, 692, A195, doi: 10.1051/0004-6361/202451102

Astropy Collaboration, Price-Whelan, A. M., Lim, P. L., et al. 2022, ApJ, 935, 167, doi: 10.3847/1538-4357/ac7c74

Battaglia, G., Helmi, A., Tolstoy, E., et al. 2008, ApJ, 681, L13, doi: 10.1086/590179

Battaglia, G., Irwin, M., Tolstoy, E., de Boer, T., & Mateo, M. 2012, ApJ, 761, L31, doi: 10.1088/2041-8205/761/2/L31

Battaglia, G., Sollima, A., & Nipoti, C. 2015, MNRAS, 454, 2401, doi: 10.1093/mnras/stv2096

Battaglia, G., Taibi, S., Thomas, G. F., & Fritz, T. K. 2022, A&A, 657, A54, doi: 10.1051/0004-6361/202141528

Battaglia, G., Tolstoy, E., Helmi, A., et al. 2011, MNRAS, 411, 1013, doi: 10.1111/j.1365-2966.2010.17745.x

—. 2006, A&A, 459, 423, doi: 10.1051/0004-6361:20065720

Battinelli, P., & Demers, S. 1999, AJ, 117, 1764, doi: 10.1086/300801

Bechtol, K., Birrer, S., Cyr-Racine, F.-Y., et al. 2022, Snowmass2021 Cosmic Frontier White Paper: Dark Matter Physics from Halo Measurements, doi: 10.48550/arXiv.2203.07354

Bellazzini, M., Ferraro, F. R., Origlia, L., et al. 2002, AJ, 124, 3222, doi: 10.1086/344794

Belokurov, V., Erkal, D., Evans, N. W., Koposov, S. E., & Deason, A. J. 2018, MNRAS, 478, 611, doi: 10.1093/mnras/sty982

Benítez-Llambay, A., Frenk, C. S., Ludlow, A. D., & Navarro, J. F. 2019, MNRAS, 488, 2387, doi: 10.1093/mnras/stz1890

Benítez-Llambay, A., Navarro, J. F., Abadi, M. G., et al. 2015, MNRAS, 450, 4207, doi: 10.1093/mnras/stv925

—. 2016, MNRAS, 456, 1185, doi: 10.1093/mnras/stv2722

Bennett, M., & Bovy, J. 2019, Monthly Notices of the Royal Astronomical Society, 482, 1417, doi: 10.1093/mnras/sty2813

Binggeli, B., Sandage, A., & Tarenghi, M. 1984, AJ, 89, 64, doi: 10.1086/113484

Binney, J., & Tremaine, S. 1987, Galactic Dynamics. https://ui.adsabs.harvard.edu/abs/1987gady.book.....B

Blanton, M. R., Lupton, R. H., Schlegel, D. J., et al. 2005, ApJ, 631, 208, doi: 10.1086/431416

Blumenthal, G. R., Faber, S. M., Primack, J. R., & Rees, M. J. 1984, Nature, 311, 517, doi: 10.1038/311517a0

Bonaca, A., & Price-Whelan, A. M. 2025, New Astron. Rev., 100, 101713, doi: 10.1016/j.newar.2024.101713

Borukhovetskaya, A., Errani, R., Navarro, J. F., Fattahi, A., & Santos-Santos, I. 2022a, MNRAS, 509, 5330, doi: 10.1093/mnras/stab2912

Borukhovetskaya, A., Navarro, J. F., Errani, R., & Fattahi, A. 2022b, MNRAS, 512, 5247, doi: 10.1093/mnras/stac653

Bournaud, F., & Duc, P. A. 2006, A&A, 456, 481, doi: 10.1051/0004-6361:20065248

Bovy, J. in press 2026, Dynamics and Astrophysics of Galaxies (Princeton, NJ: Princeton University Press)

Brada, R., & Milgrom, M. 2000, ApJ, 541, 556, doi: 10.1086/309475

Breddels, M. A., & Helmi, A. 2013, A&A, 558, A35, doi: 10.1051/0004-6361/201321606

Brown, W. R., Geller, M. J., Kenyon, S. J., & Diaferio, A. 2010, AJ, 139, 59, doi: 10.1088/0004-6256/139/1/59

Bryan, G. L., & Norman, M. L. 1998, ApJ, 495, 80, doi: 10.1086/305262

Bullock, J. S., & Boylan-Kolchin, M. 2017, Annu. Rev. Astron. Astrophys., 55, 343, doi: 10.1146/annurev-astro-091916-055313

Bullock, J. S., & Johnston, K. V. 2005, ApJ, 635, 931, doi: 10.1086/497422

Bullock, J. S., Kolatt, T. S., Sigad, Y., et al. 2001, MNRAS, 321, 559, doi: 10.1046/j.1365-8711.2001.04068.x

Caldwell, N., Armandroff, T. E., Seitzer, P., & Da Costa, G. S. 1992, AJ, 103, 840, doi: 10.1086/116105

Caldwell, N., & Bothun, G. D. 1987, AJ, 94, 1126, doi: 10.1086/114550

Cardona-Barrero, S., Battaglia, G., Di Cintio, A., Revaz, Y., & Jablonka, P. 2021, MNRAS, 505, L100, doi: 10.1093/mnrasl/slab059

Carrera, R., Aparicio, A., Martínez-Delgado, D., & Alonso-García, J. 2002, AJ, 123, 3199, doi: 10.1086/340702

Casas, R. A., Arias, V., Peña Ramírez, K., & Kroupa, P. 2012, MNRAS, 424, 1941, doi: 10.1111/j.1365-2966.2012.21319.x

Cautun, M., Deason, A. J., Frenk, C. S., & McAlpine, S. 2019, MNRAS, 483, 2185, doi: 10.1093/mnras/sty3084

Chiang, B. T., van den Bosch, F. C., & Schive, H.-Y. 2024, The Tidal Evolution of Anisotropic Subhaloes: A New Pathway to Creating Isotropic and Cored Satellites, arXiv, doi: 10.48550/arXiv.2411.03192

Choi, J.-H., Weinberg, M. D., & Katz, N. 2009, MNRAS, 400, 1247, doi: 10.1111/j.1365-2966.2009.15556.x

Christensen, C. R., Brooks, A. M., Munshi, F., et al. 2024, ApJ, 961, 236, doi: 10.3847/1538-4357/ad0c5a

Cicuéndez, L., & Battaglia, G. 2018, MNRAS, 480, 251, doi: 10.1093/mnras/sty1748

Cicuéndez, L., Battaglia, G., Irwin, M., et al. 2018, A&A, 609, A53, doi: 10.1051/0004-6361/201731450

Coleman, M. G., Da Costa, G. S., & Bland-Hawthorn, J. 2005, AJ, 130, 1065, doi: 10.1086/432662

Correa Magnus, L., & Vasiliev, E. 2022, MNRAS, 511, 2610, doi: 10.1093/mnras/stab3726

Crain, R. A., Schaye, J., Bower, R. G., et al. 2015, MNRAS, 450, 1937, doi: 10.1093/mnras/stv725

de Boer, T. J. L., Tolstoy, E., Saha, A., et al. 2011, Astronomy and Astrophysics, 528, A119, doi: 10.1051/0004-6361/201016398

de los Reyes, M. A. C., Kirby, E. N., Ji, A. P., & Nuñez, E. H. 2022, ApJ, 925, 66, doi: 10.3847/1538-4357/ac332b

de Vaucouleurs, G. 1948, Ann. astrophys., 11, 247. https://ui.adsabs.harvard.edu/abs/1948AnAp...11..247D

—. 1959, Handbuch Phys., 53, 311, doi: 10.1007/978-3-642-45932-0_8

Deason, A., Wetzel, A., & Garrison-Kimmel, S. 2014, ApJ, 794, 115, doi: 10.1088/0004-637X/794/2/115

Deason, A. J., Bose, S., Fattahi, A., et al. 2022, MNRAS, 511, 4044, doi: 10.1093/mnras/stab3524

Dekel, A., & Silk, J. 1986, ApJ, 303, 39, doi: 10.1086/164050

del Pino, A., Aparicio, A., & Hidalgo, S. L. 2015, MNRAS, 454, 3996, doi: 10.1093/mnras/stv2174

del Pino, A., Łokas, E. L., Hidalgo, S. L., & Fouquet, S. 2017, MNRAS, 469, 4999, doi: 10.1093/mnras/stx1195

Demers, S., Battinelli, P., Irwin, M. J., & Kunkel, W. E. 1995, MNRAS, 274, 491, doi: 10.1093/mnras/274.2.491

Demers, S., Krautter, A., & Kunkel, W. E. 1980, AJ, 85, 1587, doi: 10.1086/112837

Di Cintio, A., Knebe, A., Libeskind, N. I., et al. 2013, MNRAS, 431, 1220, doi: 10.1093/mnras/stt240

Di Cintio, P., Iorio, G., Calura, F., Nipoti, C., & Cantari, M. 2024, A&A, 690, A61, doi: 10.1051/0004-6361/202451335

Diaz, J. D., & Bekki, K. 2012, ApJ, 750, 36, doi: 10.1088/0004-637X/750/1/36

Dong, S., Lin, D. N. C., & Murray, S. D. 2003, ApJ, 596, 930, doi: 10.1086/378091

D'Onghia, E., & Fox, A. J. 2016, Annu. Rev. Astron. Astrophys., 54, 363, doi: 10.1146/annurev-astro-081915-023251

Drakos, N. E., Taylor, J. E., & Benson, A. J. 2020, MNRAS, 494, 378, doi: 10.1093/mnras/staa760

—. 2022, MNRAS, 516, 106, doi: 10.1093/mnras/stac2202

Drimmel, R., & Poggio, E. 2018, Research Notes of the American Astronomical Society, 2, 210, doi: 10.3847/2515-5172/aaef8b

Drlica-Wagner, A., Ferguson, P. S., Adamów, M., et al. 2022, Astrophys. J. Suppl. Ser., 261, 38, doi: 10.3847/1538-4365/ac78eb

D'Souza, R., & Bell, E. F. 2022, MNRAS, 512, 739, doi: 10.1093/mnras/stac404

Dutta Chowdhury, D., van den Bosch, F. C., van Dokkum, P., et al. 2023, ApJ, 949, 68, doi: 10.3847/1538-4357/acc73d

Dutton, A. A., & Macciò, A. V. 2014, MNRAS, 441, 3359, doi: 10.1093/mnras/stu742

El-Badry, K., Wetzel, A., Geha, M., et al. 2016, ApJ, 820, 131, doi: 10.3847/0004-637X/820/2/131

El-Zant, A. A., Freundlich, J., Combes, F., & Halle, A. 2020, MNRAS, 492, 877, doi: 10.1093/mnras/stz3478

Elmegreen, B. G., & Struck, C. 2013, ApJ, 775, L35, doi: 10.1088/2041-8205/775/2/L35

Erkal, D., Belokurov, V., Laporte, C. F. P., et al. 2019, MNRAS, 487, 2685, doi: 10.1093/mnras/stz1371

Errani, R., & Navarro, J. F. 2021, MNRAS, 505, 18, doi: 10.1093/mnras/stab1215

Errani, R., Navarro, J. F., Peñarrubia, J., Famaey, B., & Ibata, R. 2023, MNRAS, 519, 384, doi: 10.1093/mnras/stac3499

Errani, R., & Peñarrubia, J. 2020, MNRAS, 491, 4591, doi: 10.1093/mnras/stz3349

Eskridge, P. B. 1988, AJ, 95, 1706, doi: 10.1086/114767

Euclid Collaboration, Mellier, Y., Abdurro'uf, et al. 2025, A&A, 697, A1, doi: 10.1051/0004-6361/202450810

Faber, S. M., & Lin, D. N. C. 1983, ApJ, 266, L17, doi: 10.1086/183970

Fabricius, C., Luri, X., Arenou, F., et al. 2021, A&A, 649, A5, doi: 10.1051/0004-6361/202039834

Fabrizio, M., Bono, G., Nonino, M., et al. 2016, ApJ, 830, 126, doi: 10.3847/0004-637X/830/2/126

Fattahi, A., Navarro, J. F., Frenk, C. S., et al. 2018, MNRAS, 476, 3816, doi: 10.1093/mnras/sty408

Fitts, A., Boylan-Kolchin, M., Elbert, O. D., et al. 2017, MNRAS, 471, 3547, doi: 10.1093/mnras/stx1757

Fouquet, S., Łokas, E. L., del Pino, A., & Ebrová, I. 2017, MNRAS, 464, 2717, doi: 10.1093/mnras/stw2510

Freeman, K. C. 1970, ApJ, 160, 811, doi: 10.1086/150474

Fritz, T. K., Battaglia, G., Pawlowski, M. S., et al. 2018, A&A, 619, A103, doi: 10.1051/0004-6361/201833343

Gaia Collaboration, Prusti, T., de Bruijne, J. H. J., et al. 2016, 595, A1, doi: 10.1051/0004-6361/201629272

Gaia Collaboration, Helmi, A., van Leeuwen, F., et al. 2018, A&A, 616, A12, doi: 10.1051/0004-6361/201832698

Gaia Collaboration, Brown, A. G. A., Vallenari, A., et al. 2021, A&A, 649, A1, doi: 10.1051/0004-6361/202039657

Gallagher, III, J. S., & Wyse, R. F. G. 1994, Publ. Astron. Soc. Pac., 106, 1225, doi: 10.1086/133500

Garavito-Camargo, N., Besla, G., Laporte, C. F. P., et al. 2021, ApJ, 919, 109, doi: 10.3847/1538-4357/ac0b44

Genina, A., Frenk, C. S., Benítez-Llambay, A., et al. 2019, Monthly Notices of the Royal Astronomical Society, 488, 2312, doi: 10.1093/mnras/stz1852

Girardi, L., Bertelli, G., Bressan, A., et al. 2002, A&A, 391, 195, doi: 10.1051/0004-6361:20020612

Gómez-Flechoso, M. Á., & Martínez-Delgado, D. 2003, ApJ, 586, L123, doi: 10.1086/374858

Graham, A. W., & Driver, S. P. 2005, Publ. Astron. Soc. Aust., 22, 118, doi: 10.1071/AS05001

Graham, A. W., & Guzmán, R. 2003, AJ, 125, 2936, doi: 10.1086/374992

Gration, A., Hendriks, D. D., Das, P., Heber, D., & Izzard, R. G. 2025, Stellar Velocity Distributions in Binary-Rich Ultrafaint Dwarf Galaxies, arXiv, doi: 10.48550/arXiv.2509.14316

GRAVITY Collaboration, Abuter, R., Amorim, A., et al. 2018, Astronomy and Astrophysics, 615, L15, doi: 10.1051/0004-6361/201833718

Green, S. B., & van den Bosch, F. C. 2019, MNRAS, 490, 2091, doi: 10.1093/mnras/stz2767

Gutcke, T. A., Pakmor, R., Naab, T., & Springel, V. 2021, MNRAS, 501, 5597, doi: 10.1093/mnras/staa3875

Gwyn, S., McConnachie, A. W., Cuillandre, J.-C., et al. 2025, UNIONS: The Ultraviolet near-Infrared Optical Northern Survey, arXiv, doi: 10.48550/arXiv.2503.13783

Hargreaves, J. C., Gilmore, G., Irwin, M. J., & Carter, D. 1994, MNRAS, 271, 693, doi: 10.1093/mnras/271.3.693

Hayashi, E., Navarro, J. F., Taylor, J. E., Stadel, J., & Quinn, T. 2003, ApJ, 584, 541, doi: 10.1086/345788

Hayashi, K., Hirai, Y., Chiba, M., & Ishiyama, T. 2023, ApJ, 953, 185, doi: 10.3847/1538-4357/ace33e

Helmi, A., Babusiaux, C., Koppelman, H. H., et al. 2018, 563, 85, doi: 10.1038/s41586-018-0625-x

Hernquist, L. 1990, ApJ, 356, 359, doi: 10.1086/168845

Hill, G. W. 1878, American Journal of Mathematics, 5. http://archive.org/details/jstor-2369430

Ho, N., Geha, M., Munoz, R. R., et al. 2012, ApJ, 758, 124, doi: 10.1088/0004-637X/758/2/124

Hodge, P. W. 1961, AJ, 66, 384, doi: 10.1086/108443

—. 1964, AJ, 69, 438, doi: 10.1086/109295

—. 1971, Annu. Rev. Astron. Astrophys., 9, 35, doi: 10.1146/annurev.aa.09.090171.000343

Hunt, J. A. S., & Vasiliev, E. 2025, New Astron. Rev., 100, 101721, doi: 10.1016/j.newar.2024.101721

Hunter, D. A., & Elmegreen, B. G. 2006, Astrophys. J. Suppl. Ser., 162, 49, doi: 10.1086/498096

Ibata, R., Irwin, M., Lewis, G., Ferguson, A. M. N., & Tanvir, N. 2001, Nature, 412, 49, doi: 10.1038/35083506

Ibata, R. A., Gilmore, G., & Irwin, M. J. 1994, Nature, 370, 194, doi: 10.1038/370194a0

Ibata, R. A., Malhan, K., & Martin, N. F. 2019, ApJ, 872, 152, doi: 10.3847/1538-4357/ab0080

Innanen, K. A., & Papp, K. A. 1979, AJ, 84, 601, doi: 10.1086/112455

Iorio, G., Nipoti, C., Battaglia, G., & Sollima, A. 2019, MNRAS, 487, 5692, doi: 10.1093/mnras/stz1342

Irwin, M., & Hatzidimitriou, D. 1995, MNRAS, 277, 1354, doi: 10.1093/mnras/277.4.1354

Ivezić, Ž., Kahn, S. M., Tyson, J. A., et al. 2019, ApJ, 873, 111, doi: 10.3847/1538-4357/ab042c

Jacobi, G. 1836, Comptes Rendus de l'Académie des Sciences de Pariss, 3, 59. https://www.scirp.org/reference/referencespapers?referenceid=3036953

Jagourel, P., Fitzsimons, E., Hammer, F., et al. 2018, in Ground-Based and Airborne Instrumentation for Astronomy VII, Vol. 10702, 10702A4, doi: 10.1117/12.2314135

Jensen, J., Hayes, C. R., Sestito, F., et al. 2024, MNRAS, 527, 4209, doi: 10.1093/mnras/stad3322

Johnston, K. V., Spergel, D. N., & Hernquist, L. 1995, ApJ, 451, 598, doi: 10.1086/176247

Kawata, D., Arimoto, N., Cen, R., & Gibson, B. K. 2006, ApJ, 641, 785, doi: 10.1086/500633

Kent, S. M. 1985, Astrophys. J. Suppl. Ser., 59, 115, doi: 10.1086/191066

Kim, S. Y., Read, J. I., Rey, M. P., et al. 2024, EDGE: Predictable Scatter in the Stellar Mass–Halo Mass Relation of Dwarf Galaxies, arXiv, doi: 10.48550/arXiv.2408.15214

King, I. 1962, AJ, 67, 471, doi: 10.1086/108756

Kleyna, J. T., Geller, M. J., Kenyon, S. J., Kurtz, M. J., & Thorstensen, J. R. 1998, AJ, 115, 2359, doi: 10.1086/300360

Kleyna, J. T., Wilkinson, M. I., Gilmore, G., & Evans, N. W. 2003, ApJ, 588, L21, doi: 10.1086/375522

Klimentowski, J., Łokas, E. L., Kazantzidis, S., Mayer, L., & Mamon, G. A. 2009, MNRAS, 397, 2015, doi: 10.1111/j.1365-2966.2009.15046.x

Kordopatis, G., Amorisco, N. C., Evans, N. W., Gilmore, G., & Koposov, S. E. 2016, MNRAS, 457, 1299, doi: 10.1093/mnras/stw073

Kowalczyk, K., Łokas, E. L., Kazantzidis, S., & Mayer, L. 2013, MNRAS, 431, 2796, doi: 10.1093/mnras/stt376

Kroupa, P. 1997, NewA, 2, 139, doi: 10.1016/S1384-1076(97)00012-2

Kuhn, J. R., & Miller, R. H. 1989, ApJ, 341, L41, doi: 10.1086/185453

Lang, D. 2014, AJ, 147, 108, doi: 10.1088/0004-6256/147/5/108

Laplace, P. S. 1798, in Traité de mécanique céleste, Vol. 4 (De L'Imprimerie de Crapelet : Chez J.B.M. Duprat), 306–312. https://doi.org/10.5479/sil.338664.39088005644752

Lasker, B. M., Doggett, J., McLean, B., et al. 1996, in Astronomical Data Analysis Software and Systems V, Vol. 101, 88. https://ui.adsabs.harvard.edu/abs/1996ASPC..101...88L

Lee, Y., Park, H. S., Kim, S. C., et al. 2018, ApJ, 859, 5, doi: 10.3847/1538-4357/aabc53

Li, C., & White, S. D. M. 2009, MNRAS, 398, 2177, doi: 10.1111/j.1365-2966.2009.15268.x

Li, T. S., Simon, J. D., Kuehn, K., et al. 2018, ApJ, 866, 22, doi: 10.3847/1538-4357/aadf91

Lin, D. N. C., & Pringle, J. E. 1987, ApJ, 320, L87, doi: 10.1086/184981

Lindegren, L., Klioner, S. A., Hernández, J., et al. 2021, A&A, 649, A2, doi: 10.1051/0004-6361/202039709

Lokas, E. L., Ebrova, I., Del Pino, A., & Semczuk, M. 2014, MNRAS, 445, L6, doi: 10.1093/mnrasl/slu128

Loken, C., Gruner, D., Groer, L., et al. 2010, J. Phys. Conf. Ser., 256, 12026, doi: 10.1088/1742-6596/256/1/012026

Lora, V., Just, A., Sánchez-Salcedo, F. J., & Grebel, E. K. 2012, ApJ, 757, 87, doi: 10.1088/0004-637X/757/1/87

Lovell, M. R., Frenk, C. S., Eke, V. R., et al. 2014, MNRAS, 439, 300, doi: 10.1093/mnras/stt2431

Ludlow, A. D., Bose, S., Angulo, R. E., et al. 2016, MNRAS, 460, 1214, doi: 10.1093/mnras/stw1046

Ludlow, A. D., Navarro, J. F., Angulo, R. E., et al. 2014, MNRAS, 441, 378, doi: 10.1093/mnras/stu483

Makarov, D., Makarova, L., Sharina, M., et al. 2012, MNRAS, 425, 709, doi: 10.1111/j.1365-2966.2012.21581.x

Mao, Y.-Y., Geha, M., Wechsler, R. H., et al. 2021, ApJ, 907, 85, doi: 10.3847/1538-4357/abce58

Martin, N. F., Ibata, R. A., Lewis, G. F., et al. 2016, ApJ, 833, 167, doi: 10.3847/1538-4357/833/2/167

Martínez-Delgado, D., Alonso-García, J., Aparicio, A., & Gómez-Flechoso, M. A. 2001, ApJ, 549, L63, doi: 10.1086/319150

Martínez-García, A. M., del Pino, A., & Aparicio, A. 2023, MNRAS, 518, 3083, doi: 10.1093/mnras/stac3305

Mateo, M. L. 1998, Annu. Rev. Astron. Astrophys., 36, 435, doi: 10.1146/annurev.astro.36.1.435

Maxwell, A. J., Wadsley, J., Couchman, H. M. P., & Mashchenko, S. 2012, ApJL, 755, L35, doi: 10.1088/2041-8205/755/2/L35

Mayer, L., Governato, F., Colpi, M., et al. 2001, ApJ, 547, L123, doi: 10.1086/318898

McConnachie, A. W. 2012, AJ, 144, 4, doi: 10.1088/0004-6256/144/1/4

McConnachie, A. W., Arimoto, N., & Irwin, M. 2007, MNRAS, 379, 379, doi: 10.1111/j.1365-2966.2007.11969.x

McConnachie, A. W., & Irwin, M. J. 2006, MNRAS, 365, 1263, doi: 10.1111/j.1365-2966.2005.09806.x

McConnachie, A. W., & Venn, K. A. 2020a, AJ, 160, 124, doi: 10.3847/1538-3881/aba4ab

—. 2020b, Res. Notes Am. Astron. Soc., 4, 229, doi: 10.3847/2515-5172/abd18b

McGaugh, S. S., & Wolf, J. 2010, ApJ, 722, 248, doi: 10.1088/0004-637X/722/1/248

McMillan, P. J. 2011, Monthly Notices of the Royal Astronomical Society, 414, 2446, doi: 10.1111/j.1365-2966.2011.18564.x

Meisner, A. M., Lang, D., & Schlegel, D. J. 2017a, AJ, 153, 38, doi: 10.3847/1538-3881/153/1/38

—. 2017b, AJ, 154, 161, doi: 10.3847/1538-3881/aa894e

Mercado, F. J., Bullock, J. S., Boylan-Kolchin, M., et al. 2021, MNRAS, 501, 5121, doi: 10.1093/mnras/staa3958

Meza, A., Navarro, J. F., Abadi, M. G., & Steinmetz, M. 2005, MNRAS, 359, 93, doi: 10.1111/j.1365-2966.2005.08869.x

Milgrom, M. 1995, ApJ, 455, 439, doi: 10.1086/176592

Miller, T. B., van den Bosch, F. C., Green, S. B., & Ogiya, G. 2020, MNRAS, 495, 4496, doi: 10.1093/mnras/staa1450

Mirabel, I. F., Dottori, H., & Lutz, D. 1992, A&A, 256, L19. https://ui.adsabs.harvard.edu/abs/1992A&A...256L..19M

Miyamoto, M., & Nagai, R. 1975, Publ. Astron. Soc. Jpn., 27, 533. https://ui.adsabs.harvard.edu/abs/1975PASJ...27..533M

Moore, B. 1994, Nature, 370, 629, doi: 10.1038/370629a0

Moore, B., & Davis, M. 1994, MNRAS, 270, 209, doi: 10.1093/mnras/270.2.209

Moskowitz, A. G., & Walker, M. G. 2020, ApJ, 892, 27, doi: 10.3847/1538-4357/ab7459

Moster, B. P., Naab, T., & White, S. D. M. 2013, MNRAS, 428, 3121, doi: 10.1093/mnras/sts261

Muñoz, R. R., Côté, P., Santana, F. A., et al. 2018, ApJ, 860, 66, doi: 10.3847/1538-4357/aac16b

Muñoz, R. R., Geha, M., Côté, P., et al. 2012, ApJ, 753, L15, doi: 10.1088/2041-8205/753/1/L15

Navarro, J. F., Eke, V. R., & Frenk, C. S. 1996a, MNRAS, 283, L72, doi: 10.1093/mnras/283.3.L72

Navarro, J. F., Frenk, C. S., & White, S. D. M. 1996b, ApJ, 462, 563, doi: 10.1086/177173

—. 1997, ApJ, 490, 493, doi: 10.1086/304888

Navarro, J. F., Ludlow, A., Springel, V., et al. 2010, MNRAS, 402, 21, doi: 10.1111/j.1365-2966.2009.15878.x

Noeske, K. G., Papaderos, P., Cairós, L. M., & Fricke, K. J. 2003, A&A, 410, 481, doi: 10.1051/0004-6361:20031147

Ogiya, G., van den Bosch, F. C., Hahn, O., et al. 2019, MNRAS, 485, 189, doi: 10.1093/mnras/stz375

Oh, K. S., Lin, D. N. C., & Aarseth, S. J. 1995, ApJ, 442, 142, doi: 10.1086/175429

Oh, S.-H., Hunter, D. A., Brinks, E., et al. 2015, AJ, 149, 180, doi: 10.1088/0004-6256/149/6/180

Olszewski, E. W., & Aaronson, M. 1985, AJ, 90, 2221, doi: 10.1086/113925

Orkney, M. D. A., Read, J. I., Rey, M. P., et al. 2021, MNRAS, 504, 3509, doi: 10.1093/mnras/stab1066

Pace, A. B. 2024, The Local Volume Database: A Library of the Observed Properties of Nearby Dwarf Galaxies and Star Clusters. https://ui.adsabs.harvard.edu/abs/2024arXiv241107424P

Pace, A. B., Erkal, D., & Li, T. S. 2022, ApJ, 940, 136, doi: 10.3847/1538-4357/ac997b

Pace, A. B., & Li, T. S. 2019, ApJ, 875, 77, doi: 10.3847/1538-4357/ab0aee

Pace, A. B., Martinez, G. D., Kaplinghat, M., & Muñoz, R. R. 2014, MNRAS, 442, 1718, doi: 10.1093/mnras/stu938

Pace, A. B., Kaplinghat, M., Kirby, E., et al. 2020, MNRAS, 495, 3022, doi: 10.1093/mnras/staa1419

Palma, C., Majewski, S. R., Siegel, M. H., et al. 2003, AJ, 125, 1352, doi: 10.1086/367594

Panithanpaisal, N., Sanderson, R. E., Wetzel, A., et al. 2021, ApJ, 920, 10, doi: 10.3847/1538-4357/ac1109

Patel, E., Kallivayalil, N., Garavito-Camargo, N., et al. 2020, ApJ, 893, 121, doi: 10.3847/1538-4357/ab7b75

Peñarrubia, J., Benson, A. J., Walker, M. G., et al. 2010, MNRAS, 406, 1290, doi: 10.1111/j.1365-2966.2010.16762.x

Peñarrubia, J., Errani, R., Vitral, E., & Walker, M. G. 2025, Gravothermal Expansion of Dwarf Spheroidal Galaxies Heated by Dark Subhaloes, arXiv, doi: 10.48550/arXiv.2506.03904

Peñarrubia, J., Gómez, F. A., Besla, G., Erkal, D., & Ma, Y.-Z. 2015, Mon. Not. R. Astron. Soc. Lett., 456, L54, doi: 10.1093/mnrasl/slv160

Peñarrubia, J., Navarro, J. F., & McConnachie, A. W. 2008, ApJ, 673, 226, doi: 10.1086/523686

Peñarrubia, J., Navarro, J. F., McConnachie, A. W., & Martin, N. F. 2009, ApJ, 698, 222, doi: 10.1088/0004-637X/698/1/222

Piatek, S., & Pryor, C. 1995, AJ, 109, 1071, doi: 10.1086/117342

Piatek, S., Pryor, C., Bristow, P., et al. 2005, AJ, 130, 95, doi: 10.1086/430532

Planck Collaboration, Aghanim, N., Akrami, Y., et al. 2020, A&A, 641, A6, doi: 10.1051/0004-6361/201833910

Plummer, H. C. 1911, MNRAS, 71, 460, doi: 10.1093/mnras/71.5.460

Ponce, M., van Zon, R., Northrup, S., et al. 2019, in Practice and Experience in Advanced Research Computing 2019: Rise of the Machines (Learning), PEARC '19 (New York, NY, USA: Association for Computing Machinery), 1–8, doi: 10.1145/3332186.3332195

Power, C., Navarro, J. F., Jenkins, A., et al. 2003, MNRAS, 338, 14, doi: 10.1046/j.1365-8711.2003.05925.x

Putman, M. E., Gibson, B. K., Staveley-Smith, L., et al. 1998, Nature, 394, 752, doi: 10.1038/29466

Qi, Y., Zivick, P., Pace, A. B., Riley, A. H., & Strigari, L. E. 2022, MNRAS, 512, 5601, doi: 10.1093/mnras/stac805

Querci, L., Pallottini, A., Branca, L., & Salvadori, S. 2025, A&A, 694, A17, doi: 10.1051/0004-6361/202452476

Read, J. I., & Gilmore, G. 2005, MNRAS, 356, 107, doi: 10.1111/j.1365-2966.2004.08424.x

Read, J. I., Walker, M. G., & Steger, P. 2019, MNRAS, 484, 1401, doi: 10.1093/mnras/sty3404

Read, J. I., Wilkinson, M. I., Evans, N. W., Gilmore, G., & Kleyna, J. T. 2006, MNRAS, 367, 387, doi: 10.1111/j.1365-2966.2005.09959.x

Reid, M. J., & Brunthaler, A. 2004, The Astrophysical Journal, 616, 872, doi: 10.1086/424960

Revaz, Y., & Jablonka, P. 2018, A&A, 616, A96, doi: 10.1051/0004-6361/201832669

Richardson, T., & Fairbairn, M. 2014, MNRAS, 441, 1584, doi: 10.1093/mnras/stu691

Ricotti, M., Polisensky, E., & Cleland, E. 2022, MNRAS, 515, 302, doi: 10.1093/mnras/stac1485

Riello, M., Angeli, F. D., Evans, D. W., et al. 2021, A&A, 649, A3, doi: 10.1051/0004-6361/202039587

Riley, A. H., Shipp, N., Simpson, C. M., et al. 2024, Auriga Streams I: Disrupting Satellites Surrounding Milky Way-Mass Haloes at Multiple Resolutions, arXiv, doi: 10.48550/arXiv.2410.09144

Rockosi, C. M., Odenkirchen, M., Grebel, E. K., et al. 2002, AJ, 124, 349, doi: 10.1086/340957

Roederer, I. U., Pace, A. B., Placco, V. M., et al. 2023, ApJ, 954, 55, doi: 10.3847/1538-4357/ace3c1

Ryden, B. 2016, Introduction to Cosmology. https://ui.adsabs.harvard.edu/abs/2016inco.book.....R

Sales, L. V., Wetzel, A., & Fattahi, A. 2022, Nat. Astron, 6, 897, doi: 10.1038/s41550-022-01689-w

Sánchez-Salcedo, F. J., & Hernandez, X. 2007, ApJ, 667, 878, doi: 10.1086/521213

Santistevan, I. B., Wetzel, A., Tollerud, E., et al. 2024, MNRAS, 527, 8841, doi: 10.1093/mnras/stad3757

Santistevan, I. B., Wetzel, A., Tollerud, E., Sanderson, R. E., & Samuel, J. 2023, MNRAS, 518, 1427, doi: 10.1093/mnras/stac3100

Santos-Santos, I. M. E., Frenk, C. S., Navarro, J. F., Cole, S., & Helly, J. 2025, MNRAS, 540, 1107, doi: 10.1093/mnras/staf749

Sato, K. S., Komiyama, Y., Okamoto, S., et al. 2025, The Star Formation and Chemical Evolution Histories of Ursa Minor Dwarf Spheroidal Galaxy, doi: 10.48550/arXiv.2505.13161

Sawala, T., Frenk, C. S., Fattahi, A., et al. 2016, MNRAS, 457, 1931, doi: 10.1093/mnras/stw145

Schaye, J., Crain, R. A., Bower, R. G., et al. 2015, MNRAS, 446, 521, doi: 10.1093/mnras/stu2058

Schlegel, D. J., Finkbeiner, D. P., & Davis, M. 1998, ApJ, 500, 525, doi: 10.1086/305772

Sérsic, J. L. 1963, Bol. Asoc. Argent. Astron. Plata Argent., 6, 41. https://ui.adsabs.harvard.edu/abs/1963BAAA....6...41S

Sestito, F., Roediger, J., Navarro, J. F., et al. 2023a, MNRAS, 523, 123, doi: 10.1093/mnras/stad1417

Sestito, F., Zaremba, D., Venn, K. A., et al. 2023b, MNRAS, 525, 2875, doi: 10.1093/mnras/stad2427

Shapley, H. 1938, Harv. Coll. Obs. Bull., 908, 1. https://ui.adsabs.harvard.edu/abs/1938BHarO.908....1S

Shipp, N., Panithanpaisal, N., Necib, L., et al. 2023, ApJ, 949, 44, doi: 10.3847/1538-4357/acc582

Simon, J. D. 2018, ApJ, 863, 89, doi: 10.3847/1538-4357/aacdfb

—. 2019, Annu. Rev. Astron. Astrophys., 57, 375, doi: 10.1146/annurev-astro-091918-104453

Simon, J. D., & Geha, M. 2007, ApJ, 670, 313, doi: 10.1086/521816

Skúladóttir, Á., Puls, A. A., Amarsi, A. M., et al. 2023, Messenger, 190, 19, doi: 10.18727/0722-6691/5304

Smith, S. E. T., Cerny, W., Hayes, C. R., et al. 2024, ApJ, 961, 92, doi: 10.3847/1538-4357/ad0d9f

Sohn, S. T., Patel, E., Besla, G., et al. 2017, ApJ, 849, 93, doi: 10.3847/1538-4357/aa917b

Spencer, M. E., Mateo, M., Olszewski, E. W., et al. 2018, AJ, 156, 257, doi: 10.3847/1538-3881/aae3e4

Springel, V., Pakmor, R., Zier, O., & Reinecke, M. 2021, MNRAS, 506, 2871, doi: 10.1093/mnras/stab1855

Springel, V., Yoshida, N., & White, S. D. M. 2001, NewA, 6, 79, doi: 10.1016/S1384-1076(01)00042-2

Springel, V., Wang, J., Vogelsberger, M., et al. 2008, MNRAS, 391, 1685, doi: 10.1111/j.1365-2966.2008.14066.x

Starkenburg, T. K., Helmi, A., & Sales, L. V. 2016, A&A, 587, A24, doi: 10.1051/0004-6361/201527247

Stinson, G. S., Dalcanton, J. J., Quinn, T., et al. 2009, MNRAS, 395, 1455, doi: 10.1111/j.1365-2966.2009.14555.x

Strigari, L. E. 2010, Adv. Astron., 2010, 407394, doi: 10.1155/2010/407394

Strobel, N. V., & Lake, G. 1994, ApJ, 424, L83, doi: 10.1086/187280

Stücker, J., Ogiya, G., Angulo, R. E., Aguirre-Santaella, A., & Sánchez-Conde, M. A. 2023, MNRAS, 521, 4432, doi: 10.1093/mnras/stad844

Tarumi, Y., Yoshida, N., & Frebel, A. 2021, ApJL, 914, L10, doi: 10.3847/2041-8213/ac024e

Tchiorniy, K., & Genina, A. 2025, Broken Expectations: The Effects of Modelling Assumptions on the Inferred Dark Matter Distribution in the Milky Way's Satellites, doi: 10.48550/arXiv.2504.18617

Tollet, E., Macciò, A. V., Dutton, A. A., et al. 2016, MNRAS, 456, 3542, doi: 10.1093/mnras/stv2856

Tolstoy, E., Irwin, M. J., Helmi, A., et al. 2004, ApJ, 617, L119, doi: 10.1086/427388

Tolstoy, E., Skúladóttir, Á., Battaglia, G., et al. 2023, A&A, 675, A49, doi: 10.1051/0004-6361/202245717

Tsujimoto, T., & Shigeyama, T. 2002, ApJ, 571, L93, doi: 10.1086/341370

van Agt, S. L. Th. J. 1978, Publ. David Dunl. Obs., 3, 205. https://ui.adsabs.harvard.edu/abs/1978PDDO....3..205V

van den Bosch, F. C., Ogiya, G., Hahn, O., & Burkert, A. 2018, MNRAS, 474, 3043, doi: 10.1093/mnras/stx2956

Vasiliev, E. 2019, MNRAS, 482, 1525, doi: 10.1093/mnras/sty2672

—. 2023, Galaxies, 11, 59, doi: 10.3390/galaxies11020059

—. 2024, MNRAS, 527, 437, doi: 10.1093/mnras/stad2612

Vitral, E., van der Marel, R. P., Sohn, S. T., et al. 2025, HSTPROMO Internal Proper Motion Kinematics of Dwarf Spheroidal Galaxies: II. Velocity Anisotropy and Dark Matter Cusp Slope of Sculptor, doi: 10.48550/arXiv.2508.20711

Walcher, C. J., Fried, J. W., Burkert, A., & Klessen, R. S. 2003, A&A, 406, 847, doi: 10.1051/0004-6361:20030768

Walker, M. G., Mateo, M., & Olszewski, E. W. 2008, ApJ, 688, L75, doi: 10.1086/595586

—. 2009a, AJ, 137, 3100, doi: 10.1088/0004-6256/137/2/3100

Walker, M. G., Mateo, M., Olszewski, E. W., et al. 2009b, ApJ, 704, 1274, doi: 10.1088/0004-637X/704/2/1274

Walker, M. G., Mateo, M., Olszewski, E. W., Sen, B., & Woodroofe, M. 2009c, AJ, 137, 3109, doi: 10.1088/0004-6256/137/2/3109

Walker, M. G., & Peñarrubia, J. 2011, ApJ, 742, 20, doi: 10.1088/0004-637X/742/1/20

Wang, E., & Lilly, S. J. 2022, ApJ, 927, 217, doi: 10.3847/1538-4357/ac49ed

Wang, J., Hammer, F., Yang, Y., et al. 2024, MNRAS, 527, 7144, doi: 10.1093/mnras/stad3651

Wechsler, R. H., & Tinker, J. L. 2018, Annu. Rev. Astron. Astrophys., 56, 435, doi: 10.1146/annurev-astro-081817-051756

Weisz, D. R., Dolphin, A. E., Skillman, E. D., et al. 2014, ApJ, 789, 147, doi: 10.1088/0004-637X/789/2/147

Westfall, K. B., Majewski, S. R., Ostheimer, J. C., et al. 2006, AJ, 131, 375, doi: 10.1086/496975

White, S. D. M. 1983, ApJ, 274, 53, doi: 10.1086/161425

White, S. D. M., & Frenk, C. S. 1991, 379, 52, doi: 10.1086/170483

White, S. D. M., & Rees, M. J. 1978, MNRAS, 183, 341, doi: 10.1093/mnras/183.3.341

Willman, B., & Strader, J. 2012, AJ, 144, 76, doi: 10.1088/0004-6256/144/3/76

Wolf, J., Martinez, G. D., Bullock, J. S., et al. 2010, MNRAS, 406, 1220, doi: 10.1111/j.1365-2966.2010.16753.x

Woo, J., Courteau, S., & Dekel, A. 2008, MNRAS, 390, 1453, doi: 10.1111/j.1365-2966.2008.13770.x

Wright, A. C., Brooks, A. M., Weisz, D. R., & Christensen, C. R. 2019, MNRAS, 482, 1176, doi: 10.1093/mnras/sty2759

Wu, J., Struck, C., Elmegreen, B. G., & D'Onghia, E. 2022, MNRAS, 517, 4417, doi: 10.1093/mnras/stac2870

Yang, Y., Hammer, F., Fouquet, S., et al. 2014, MNRAS, 442, 2419, doi: 10.1093/mnras/stu931

A. The Reliability of Projected Number Density Profiles Derived from *Gaia*

In this section, we detail the J+24 membership algorithm and test the resulting density profiles for Scl and UMi. We compare profiles derived with alternative methodologies and literature results. We also present a non-parametric Bayesian density profile, which reproduces J+24's results in the inner regions but differs when the background dominates. We find the density profiles are robust up to the background-limited radius derived here.

A.1 Bayesian membership probabilities

To create a high-quality sample, J+24 select stars initially from Gaia within a 2–4 degree region around each satellite with reliable astrometry, sensible photometry, consistent parallaxes, and broadly consistent proper motions and colours. Stars are removed if they have excess astrometric noise (ruwe > 1.3, see Lindegren et al. 2021), colour excess 3σ outside of expectations (from Riello et al. 2021), proper motions $> 10\,\mathrm{mas}^{-1}\,\mathrm{yr}^{-1}$ in $|\mu_{\alpha*}|$ or $|\mu_\delta|$, magnitudes brighter than the tip of the red giant branch[1] or fainter than $G = 22$, or colours outside $-0.5 < G_{\mathrm{BP}} - G_{\mathrm{RP}} < 2.5$. Photometry is dereddened with Schlegel et al. (1998) extinction maps.

J+24 construct satellite likelihoods in spatial, proper motion, and CMD space following expected satellite properties. J+24 model the spatial likelihood as either a one or two-component exponential (Eq. 1.3). The structural parameters of the inner component are fixed, and marginalized over if one-component. The outer profile scale radius and normalization are free parameters.

The PM likelihood is a bivariate Gaussian with variance and covariance equal to each star's proper motions.

J+24 model the CMD as a Padova isochrone (Girardi et al. 2002), with metallicity matching that obtained spectroscopically, 12 Gyr age (or 2 Gyr for Fornax), and a Gaussian width of 0.1 mag plus the *Gaia* colour uncertainty at each magnitude. The horizontal branch is

[1]Derived from the maximum RGB magnitude from the associated Padova isochrone plus 5σ times the distance modulus uncertainty.

modelled as a constant-magnitude[2] sequence extending blue of the CMD with the same width as the RGB. The CMD likelihoods are marginalized over the distance modulus and take the maximum of the RGB and horizontal branch likelihoods.

The background likelihoods are determined empirically from kernel density estimates of stars outside $5R_h$ in PM and CMD space. The spatial background likelihood is uniform.

J+24 derive the distributions of parameters (proper motions, satellite fraction $f_{\rm sat}$, and second spatial component if included) through Monte Carlo Markov chain sampling with broad or weakly-informative priors. The posterior modes are used to calculate the final $P_{\rm sat}$ values.

A.2 Independent sample selection

To test for possible limitations in the J+24 methodology (discussed below), we compare their density profiles against samples derived from absolute cuts in *Gaia* and external photometric surveys.

The `simple` sample is selected from stars in *Gaia* using absolute astrometric and quality cuts. We require high-quality astrometry (`ruwe` < 1.3), parallaxes 3σ-consistent with the dwarf's distance, proper motions with $1\,\mathrm{mas}^{-1}\,\mathrm{yr}^{-1}$ of the systemic value, and colours within the dwarf's apparent CMD as determined from stars near the dwarf's centre (see Fig. A.1).

We also determine density profiles from the deeper photometric surveys. For Scl, we use data from the DECam Local Volume Exploration Survey (DELVE) DR2 survey (Drlica-Wagner et al. 2022). We select sources within an ellipse of radius 150 arcminutes, categorized as likely stars, with reliable g and r magnitudes (associated flags ≤ 4), and within Scl's CMD selection (orange polygon in Fig. A.1). Ursa Minor lies within the Ultraviolet Near-Infrared Optical Northern Survey (UNIONS, Gwyn et al. 2025). We select sources within an ellipse of radius 230 armin, with no `FLAGS_CFIS` set, both `s21` and `s31` < 3 (i.e., not extended sources), and within the CMD polygon in Fig. A.1.

A.3 Possible biases in *Gaia*-derived density profiles

We now discuss potential biases in J+24's algorithm for *Gaia* data. We then test how these biases may influence density profiles. In all cases, density profiles converge within $R_{\rm ell} \approx 60$ arcmin, where background contamination begins to dominate.

Likelihood misspecification. The J+24 likelihoods may be misspecified. Particularly, the CMD model is simple and does not account for, e.g., the expected number of stars on

[2]Specifically, the mean magnitude of the 12 Gyr, [Fe/H] = −2.2, Padova isochrone's horizontal branch.

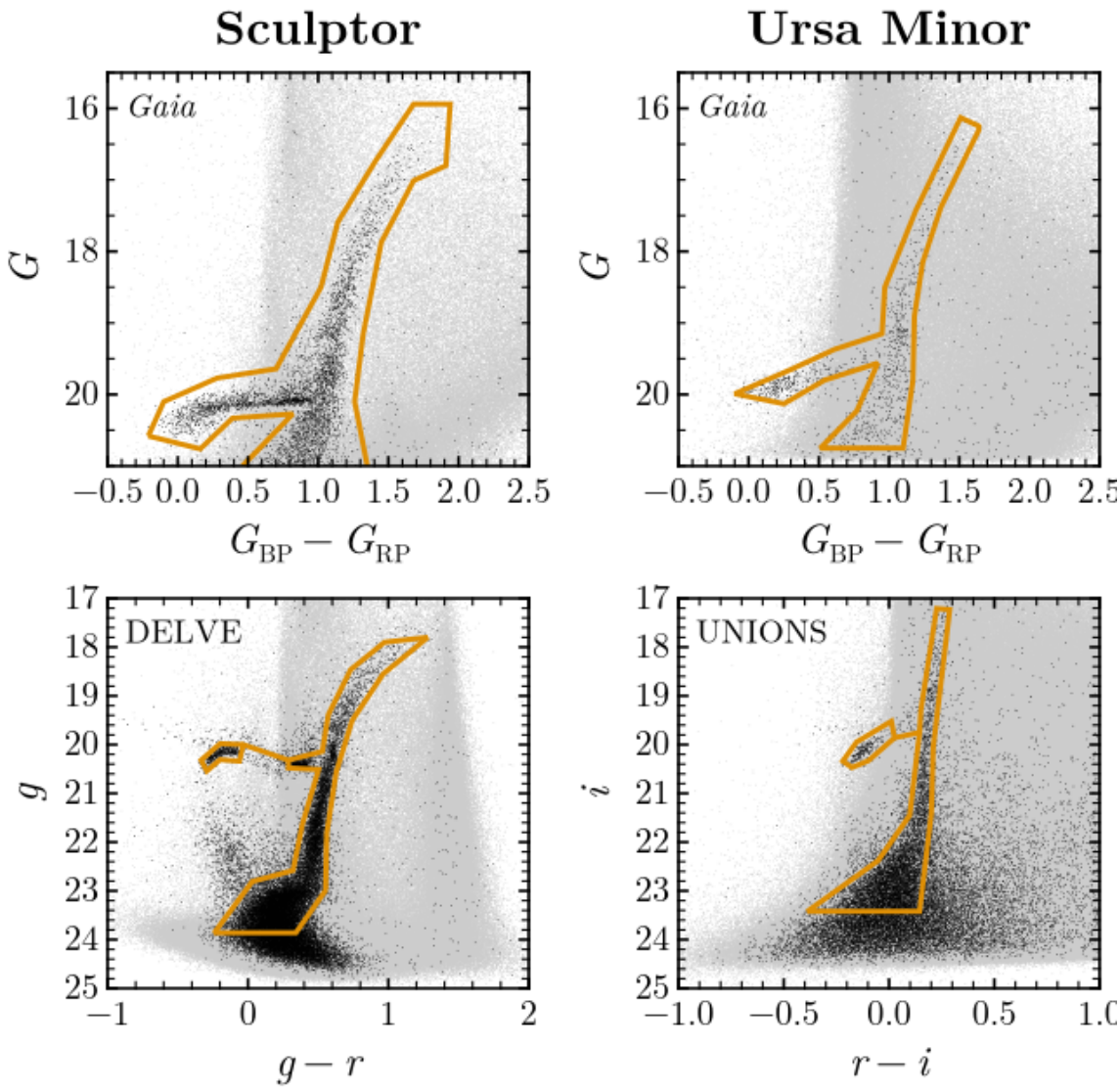

Figure A.1: Colour-magnitude diagram cuts used in samples in this section. Black points represent stars within $1R_h$, light grey shows all field stars passing quality cuts, and the orange polygon shows the CMD cut. The central, likely-member stars inform the CMD selections.

various parts of the isochrone and assume the galaxy is a single population. In this case, the probabilities likely do not reflect true membership probabilities.

Spatial likelihood. Since J+24 include a spatial likelihood, the resulting density profiles risk "double fitting"—the same spatial distribution of stars informs the membership catalogue and the subsequent density profiles. If the spatial likelihood misrepresents the underlying satellite structure, then the density profiles may be biased towards the assumed shape.

Structural uncertainties. The assumed structural parameters of a dwarf (centre, position angle, ellipticity, scale radius) may be inaccurate or vary radially. This would change the elliptical radii of stars ($R_{\rm ell}$) and likewise the density profiles.

Completeness. *Gaia*'s completeness appears high but imperfect, more limited in crowded fields, for faint sources ($G \gtrsim 20$), and in $G_{\rm BP}$-$G_{\rm RP}$ magnitudes. In Fabricius et al. (2021), the completeness down to $G \approx 20$ is $\sim 80\%$ for low-density globular clusters. As dwarfs are even less dense, their completeness is likely higher.

The top row of Fig. A.2 compares the density profiles assuming different spatial likelihoods: the `2-exp` and `1-exp` use two or one-component spatial likelihoods in J+24, and `simple` does not assume a spatial likelihood (described above). All profiles agree within the background-limited (BG-limited) radius, derived below. The `1-exp` profile predicts lower outer densities, yet the outer density excess in Sculptor and Ursa Minor persists. Thus, the spatial likelihood can influence the outer regions but has less effect on the inner regions.

The lower panels of Fig. A.2 test other possible biases. The `circ` profile uses circular bins and the J+24 sample, assuming a circular outer profile. As the profile is nearly identical to the fiducial model, an extreme change in ellipticity does not affect our conclusions. The `bright` profile is derived using only the brighter half of stars. We find no substantive change compared to our fiducial density profiles, showing completeness-related magnitude biases are likely small. Finally, the DELVE and UNIONS density profiles nearly identically trace the `2-exp` profile, but both become background-limited near the BG-limited radius.

In all cases, there is little evidence for biases in *Gaia*'s completeness or sensitivity to structural parameters. As the spatial likelihood appears to be the most severe bias, we next consider a more flexible model.

A.4 A Bayesian density profile

To address the concerns discussed above, we consider here a non-parametric model to fit the density in each bin. We demonstrate that the non-parametric model fails to find evidence

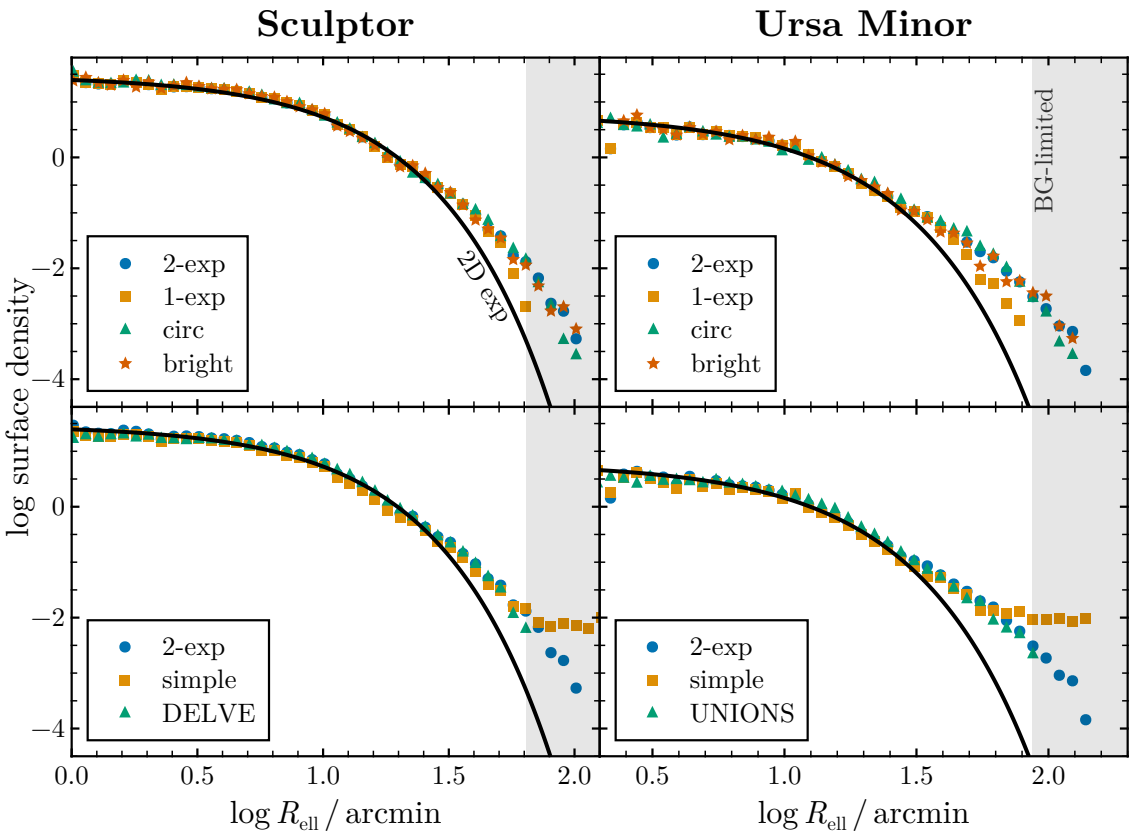

Figure A.2: Density profiles for various assumptions for Sculptor (left) and Ursa Minor (right). Each profile is plotted as points in log surface density (scaled to the `2-exp` profile) versus log radius, the black line marks a 2D exponential profile, and the grey shaded region represents the background-limited region derived in Section A.4.

for stellar density, where J+24 still detects members. Notably, our density profiles diverge substantially from J+24 for Antlia II. We suggest these differences arise from background contamination, motivating our "limiting radii" representing where densities may become unreliable.

A.4.1 Methodology

As a non-parametric but similar model to J+24, we consider a piecewise constant spatial likelihood. In this model, the stars are divided into radial bins, which are then considered independently. Each bin has only one free parameter, the fraction of satellite stars in that bin, $f_{\rm sat}$. This model thus directly derives the density profile from the data in a single step. If a bin contains insufficient information to estimate a precise satellite density, then the posterior $f_{\rm sat}$ should reflect this uncertainty.

We parameterize $f_{\rm sat}$ in terms of a log-relative density, θ

$$\begin{aligned} \theta &\equiv \log_{10}(\Sigma_{\rm sat}/\Sigma_{\rm bg}) \\ f_{\rm sat} &= \frac{10^{\theta}}{1+10^{\theta}}. \end{aligned} \tag{A.1}$$

We then adopt a broad uniform prior on θ from -12 to 6. The CMD and PM likelihoods are unchanged from J+24, except that the systemic PM is fixed for efficiency.

To bin stars, we hold fixed J+24's structural parameters and create bins of width $\Delta \log R = 0.05$ or containing the next 20 stars, whichever is wider. We then derive posterior $f_{\rm sat}$ distributions with MCMC (48 walkers of 1000 steps each, and using the No-U-Turn sampler as implemented in Turing.jl). The final density profile is directly derived from $f_{\rm sat}$ and the number of stars in each bin.

A.4.2 Results

Figs. A.3, A.4 show the derived MCMC density profiles as compared to J+24. In general, both methodologies produce similar densities. However, J+24 tend to systematically overestimate faint densities and confidently derive densities where the MCMC model fails to determine the satellite density.

In the outskirts of satellites, more background/foreground stars may have consistent PM and CMD properties than satellite members. Improperly estimating the satellite's density in this "background-limited" regime likely affects the inferred density of members. If the satellite's density is severely overestimated, then a J+24-like sample may select many additional

Table A.1: For each classical dwarf, the limiting radius $R_{\rm limit}$ in units of R_h and arcminutes. $R_{\rm limit}$ represents where there is no longer evidence of Emph(Str(Gaia)) members using the nonparametric MCMC density profiles.

Galaxy	$R_{\rm limit}/R_h$	$R_{\rm limit}/'$
Fornax	5.25	79.1
Sculptor	6.39	64.1
Leo I	4.23	13.5
Ursa Minor	6.42	86.4
Leo II	3.63	8.76
Carina	4.16	33.3
Draco	3.59	27.3
Canes Venatici I	1.95	12.5
Sextans I	3.42	67.9
Crater II	1.93	39.0

background stars. The density of candidates would then be biased towards the assumed density. As J+24 only use a one or two-component density profile across the entire dwarf, the density profile is likely biased where the CMD+PM background dominates. The nonparametric MCMC model instead does not assume a local density, so it should better represent the underlying satellite density.

Antlia II represents an extreme example—J+24 and the non-parametric density model systematically disagree across the entire galaxy. Additionally, the piecewise model derives densities with larger uncertainties and over a smaller range than J+24. The methodological divergence here likely arises due to an extraordinary background/foreground of MW stars. *Gaia* data alone may be unable to properly constrain the density of such background-contaminated objects.

To properly compare density profiles before background-limiting effects become important, we only calculate our profiles in the main text out to the radii in Table A.1. We derive these "background-limited" radii based on the outermost derived density in the MCMC non-parametric model with an uncertainty lower than 1 dex. This closely corresponds to the background density from the "CMD+PM" samples in the main text (see Fig. 2.4).

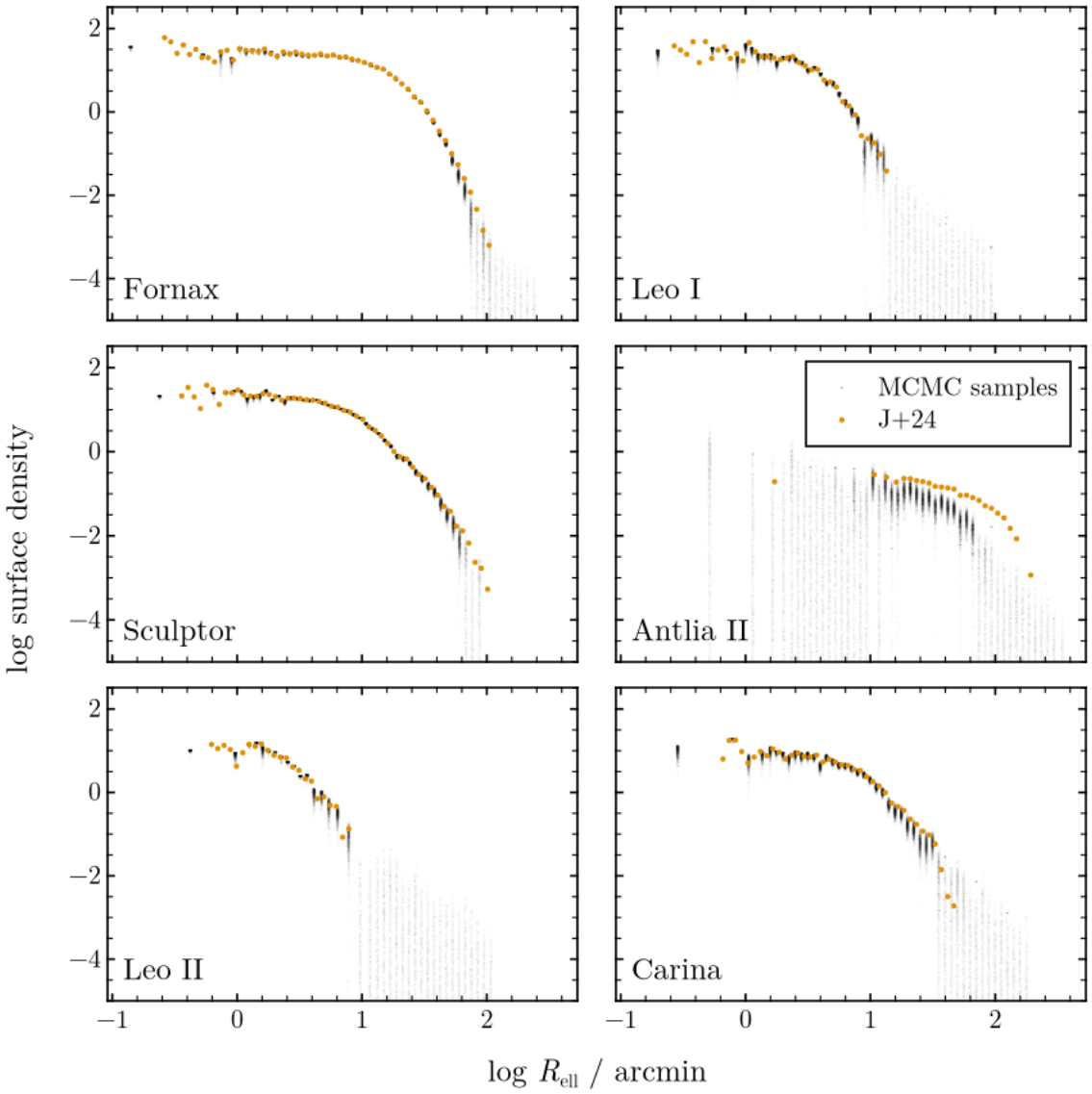

Figure A.3: A comparison between the MCMC histogram method and J+24. The MCMC samples in each bin are black transparent dots (with added jitter), and the J+24 derived density profiles (i.e., $P_{\rm sat} < 0.2$) are orange solid dots.

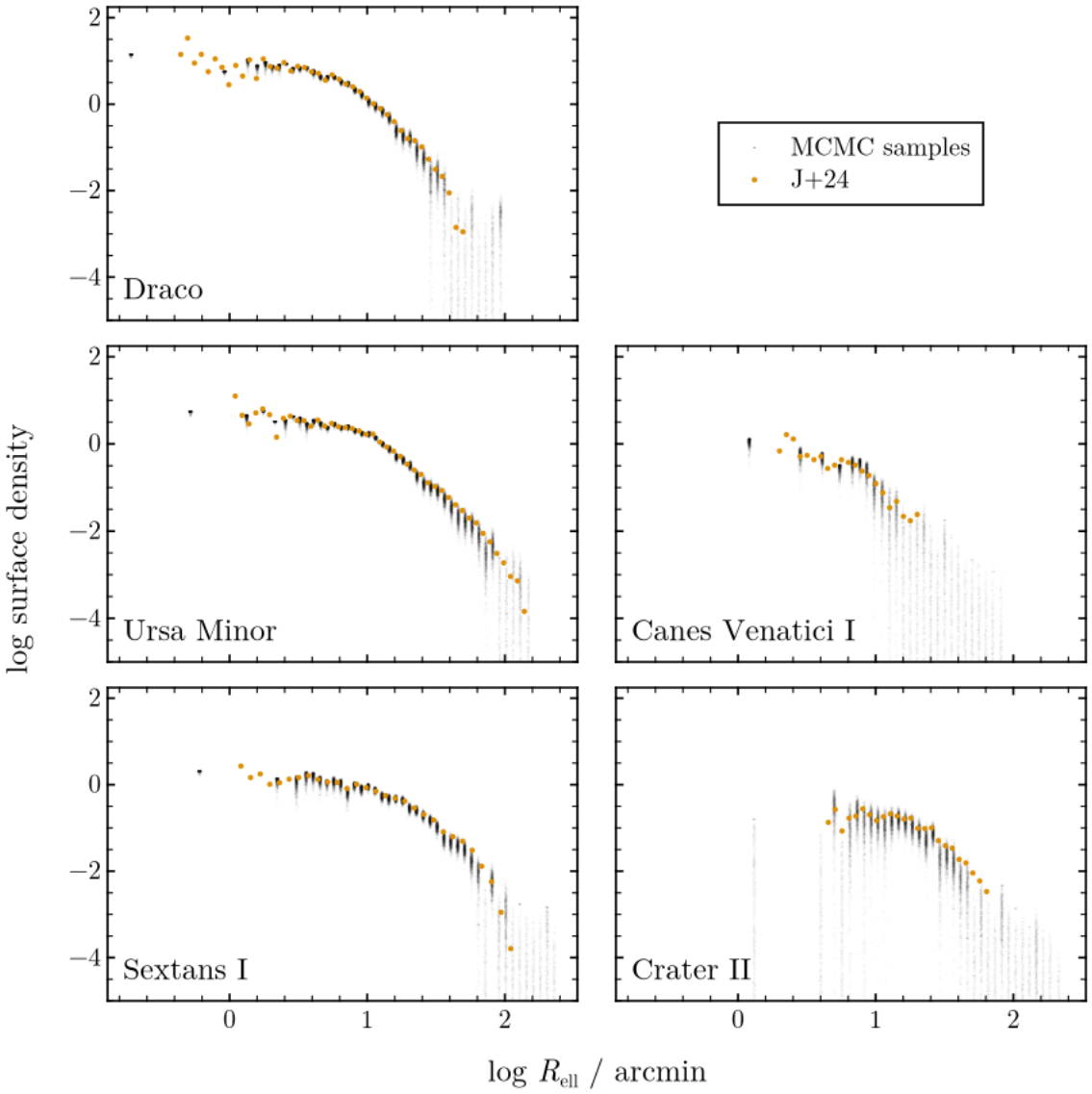

Figure A.4: Fig. A.3 continued.

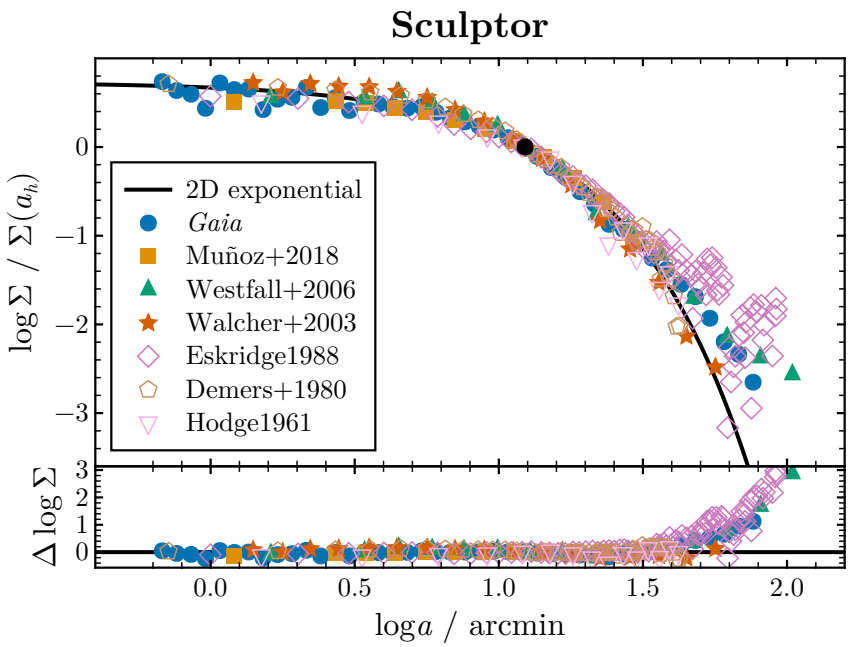

Figure A.5: A comparison of density profiles of Sculptor for works from the literature. Unlike most profiles in this thesis, this density profile is plotted with respect to the semi-major elliptical radius ($a = R_{\rm ell}/\sqrt{1-{\rm ell}}$). The solid black line is a 2D exponential with a corresponding scale radius to Scl's half-light radius, and the residuals in the bottom panel are with respect to this profile. References are (in order), Muñoz et al. (2018); Westfall et al. (2006); Walcher et al. (2003); Eskridge (1988); Demers et al. (1980); and Hodge (1961).

A.5 Comparison to literature

Finally, we compare our density profiles against a sample of literature-derived density profiles in Figs. A.5, A.6. Deviations between different profiles are small, despite the range of methods across time, and all density profiles extending into the outskirts of Scl and UMi show a similar overdensity to the ones we find. The extended stellar profiles of Scl and UMi appear to be a robust result across the literature.

A.6 Summary

In this Appendix, we discussed the methodological details of the J+24 sample selection algorithm. We consider possible biases due to the assumed spatial likelihood, *Gaia*'s completeness, and structural parameters. In all cases, we find that these assumptions likely do

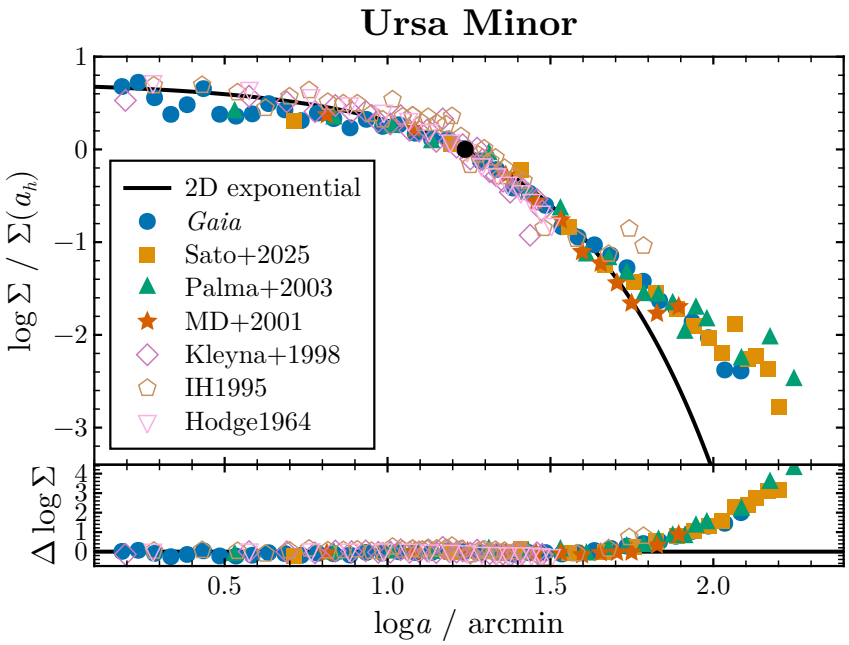

Figure A.6: Similar to Fig. A.5 except for Ursa Minor. The references are (in order) Sato et al. (2025; derived using their minor axis profile); Palma et al. (2003); Martínez-Delgado et al. (2001); Kleyna et al. (1998); Irwin & Hatzidimitriou (1995); and Hodge (1964).

not cause major biases in the derived density profiles. However, we show that J+24's density profiles may become unreliable when dropping below the background of satellite-like stars. Finally, comparing our density profiles against the literature, we find our results to be consistent. We conclude that the detection of an extended density profile in Scl and UMi is robust to incompleteness, methodology, alternative surveys, and across the literature.

B. Line-of-Sight Velocities: Sample Selection and Modelling

In this section, we analyze the observed line-of-sight (LOS) velocity distributions for Sculptor (Scl) and Ursa Minor (UMi). We aim to test for kinematic tidal signatures by combining literature LOS velocities with J+24's membership framework. Our derived systemic velocities and dispersions are consistent with the literature. We find weak evidence for a velocity gradient in Scl. As the gradient is misaligned with the orbit, the gradient more likely reflects intrinsic rotation than tidal disruption. Scl's velocity dispersion also rises within the effective radius, but predominantly in the inner regions, contrary to tidal disruption. We find no evidence of a gradient in mean velocity or velocity dispersion in UMi. We conclude that Scl and UMi do not show clear features of tidal disruption given current velocity observations.

B.1 Data processing and selection

We compile LOS velocities from several spectroscopic surveys. For Sculptor, we combine Tolstoy et al. (2023); Walker et al. (2009c); Sestito et al. (2023a); and APOGEE (DR17, Abdurro'uf et al. 2022). For Ursa Minor, we combine Spencer et al. (2018); Pace et al. (2020); Sestito et al. (2023b); and APOGEE. We then cross-match all catalogues to J+24 Gaia stars. If a study did not report *Gaia* DR3 source IDs, we match to the nearest star within 1–3 arcseconds. We combine measurements of the same star using inverse-variance weighting. To reduce likely binaries, we remove stars with significant velocity dispersions.[1]

We build on J+24's likelihood by adding multiplicative terms in the total likelihood for the velocity consistency (see Section 2.1). We assume that the satellite and background $v_{\rm los,gsr}$ distributions are Gaussian in the Galactic Standard of Rest (GSR, i.e., same location as ICRS but velocities relative to the galactic centre). For the satellite, we adopt a mean and standard deviation based on Tables 1.1, 1.2, and, for the background, mean $0\,{\rm km\,s^{-1}}$ and dispersion $\sigma_{\rm halo} = 100\,{\rm km\,s^{-1}}$ (e.g. Brown et al. 2010). We select stars with velocity-informed satellite membership probabilities of greater than 0.2. For Scl, we find 1918 unique mem-

[1]Specifically, using that $\chi^2 = \frac{s^2}{\delta\bar{v}^2}$, we remove stars with a χ^2 larger than the 99.9th percentile of the χ^2 distribution with $N-1$ measurements.

bers and UMi, 831.

For UMi, we shifted the velocities of Spencer et al. (2018) ($-1.1\,\mathrm{km\,s^{-1}}$) and Pace et al. (2020) ($+1.1\,\mathrm{km\,s^{-1}}$) to account for a systematic velocity offset. Otherwise, all studies appear to be on a similar velocity scale.

We correct the velocities for the solar motion and the on-sky size of the galaxy. We transform the velocities into the GSR and correct for the apparent gradient induced by the dwarf's proper motion (see, Walker et al. 2008; Strigari 2010). We define v'_{gsr} to be velocities in the GSR frame, subtracting the PM-induced gradient. The correction from both effects induces an apparent gradient of about $1.3\,\mathrm{km\,s^{-1}\,deg^{-1}}$ for Sculptor and less for Ursa Minor. The uncertainty on this velocity correction is less than the individual star uncertainties and any derived velocity gradients.

B.2 Monte Carlo Markov chain modelling

We fit Monte Carlo Markov chain (MCMC) models to solve for the systemic velocity, velocity dispersion, and possible gradients in velocities or velocity dispersions. We assume that the galaxy follows a planar velocity gradient. The mean velocity at a given point on the sky, μ, is assumed to be,

$$\mu(\xi, \eta) = \mu_0 + a\,\xi + b\,\eta, \tag{B.1}$$

for tangent plane coordinates ξ and η, systemic velocity μ_0, and velocity gradient slopes a and b. The velocity dispersion at a given position, σ, is assumed to depend as a power-law on elliptical radius R_{ell} alone:

$$\log\sigma = \log\sigma_0 + c\ \log(R_{\mathrm{ell}}/R_h) \tag{B.2}$$

where σ_0 is the system's velocity dispersion at R_h, and c is the velocity dispersion gradient slope. We use weakly-informative priors, as described in Table B.1, and with $a, b \sim N(0, 6^2)\,\mathrm{km\,s^{-1}\,deg^{-1}}$.

B.3 Results

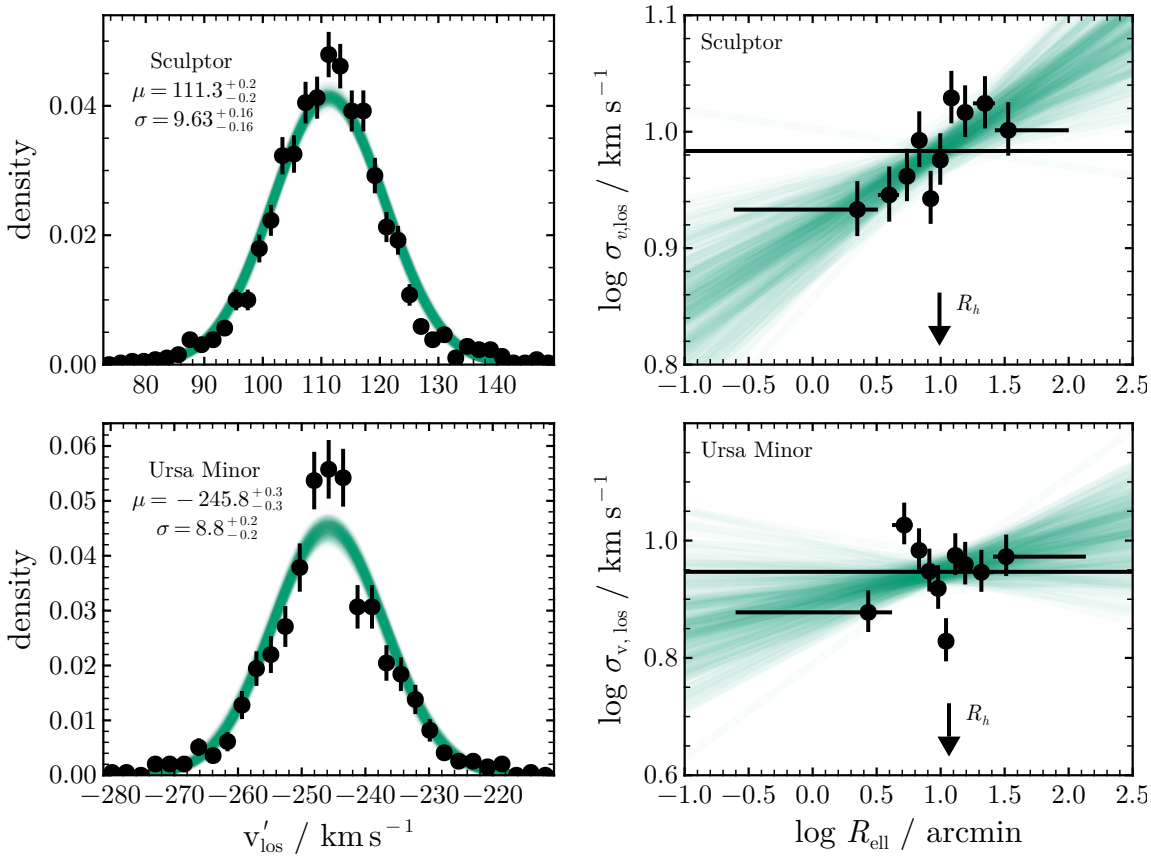

Figure B.1: **Left:** Velocity histogram of Scl and UMi in terms of projected-correction LOS velocity. Black points with error bars are a histogram of LOS-velocity members, and green lines represent MCMC fits to the velocity dispersion. **Right:** The observed velocity dispersion gradient (black points) in 10 equal number bins and the derived slopes for MCMC samples (green lines). Scl shows moderate evidence for an increasing velocity dispersion with radius, but Scl's velocity dispersion appears to flatten outside of R_h. UMi's evidence for a radial gradient is weaker.

Table B.1: MCMC fits for different RV datasets for Sculptor among 3 different models. The first row contains the priors (N for normal with mean and variance, U for uniform distributions).

galaxy	study	μ	σ	$\partial \log \sigma / \partial \log R$	$\partial v_z / \partial x$	$\theta_{\rm sigma}$	$\log b f_{\rm grad}$	$\log b f_{\rm grad}$
units	—	km s^{-1}	km s^{-1}	dex	km s^{-1} dec^{-1}	deg	—	—
Prior	—	$N(0, 100^2)$	$U(0, 20)$	$N(0, 0.3^2)$				
Scl								
	all	111.3 ± 0.2	9.63 ± 0.16	0.07 ± 0.02	4.4 ± 1.4	-146^{+18}_{-14}	-3.4	-2.7
	tolstoy+23	111.2 ± 0.3	9.70 ± 0.18	0.083 ± 0.023	4.4 ± 1.5	-154^{+18}_{-15}	-4.1	-0.9
	walker+09	111.1 ± 0.3	9.5 ± 0.2	0.05 ± 0.03	5.2 ± 1.8	-135^{+23}_{-17}	$+0.7$	-1.7
	apogee	111.2 ± 0.7	8.4 ± 0.5	0.06 ± 0.06	$5.4^{+2.7}_{-2.4}$	-127^{+49}_{-36}	$+1.1$	$+0.2$
UMi								
	all	-245.8 ± 0.3	8.8 ± 0.2	0.04 ± 0.03	4 ± 2	-210^{+21}_{-17}	$+1.4$	$+1.1$
	pace+20	-244.5 ± 0.4	9.1 ± 0.3	0.08 ± 0.05	5 ± 3	-216 ± 25	$+0.5$	$+0.7$
	spencer+18	-247.0 ± 0.4	8.7 ± 0.3	-0.004 ± 0.05	6 ± 3	-214 ± 20	$+1.8$	-0.2
	apogee	-245.9 ± 1.3	10.0 ± 1.0	0.04 ± 0.98	6^{+4}_{-3}	-200 ± 50	$+1.0$	$+0.5$

We derive a systemic velocity for Sculptor of $111.3 \pm 0.2\,\mathrm{km\,s^{-1}}$ with velocity dispersion $9.64 \pm 0.16\,\mathrm{km\,s^{-1}}$ (see Fig. B.1). Our values are very consistent with previous work (e.g., Walker et al. 2009c; Arroyo-Polonio et al. 2024; Battaglia et al. 2008). We detect a moderately significant gradient of $4.3 \pm 1.3\,\mathrm{km\,s^{-1}\,deg^{-1}}$ at a position angle of -149^{+17}_{-13} degrees, similar to past detections (e.g., Arroyo-Polonio et al. 2024; Battaglia et al. 2008; but see also Strigari 2010; Martínez-García et al. 2023).

Fig. B.2 plots the combined velocity sample and the MCMC samples for the velocity gradient. While some samples have a gradient consistent with 0, most samples have a positive velocity gradient, consistent with the rolling median trend. The velocity gradient in Scl is misaligned with the proper motion.

We derive a mean $-245.8 \pm 0.3_{\mathrm{stat}}\,\mathrm{km\,s^{-1}}$ and velocity dispersion of $8.8 \pm 0.2\,\mathrm{km\,s^{-1}}$ for UMi (see Fig. B.1). We do not find evidence for a velocity gradient. This is consistent with previous work (Pace et al. 2020; somewhat with Spencer et al. 2018; Martínez-García et al. 2023).

B.4 Discussion and caveats

Binarity. Binary star systems may inflate the inferred system's velocity dispersion. For Scl and UMi with high measured velocity dispersion, binaries likely add $\sim 1\,\mathrm{km\,s^{-1}}$ to the velocity dispersion (Spencer et al. 2018; Gration et al. 2025).

Multiple populations. Both Sculptor and Ursa Minor likely contain multiple populations with different kinematics (see Section 5.1.2). We do not model these separately—it is unclear how to define a velocity dispersion in such a case.

Inter-study biases. While basic crossmatches and a simple velocity shift, combining data from multiple instruments is challenging. Studies may also have biased selection effects or misrepresentative uncertainties, biasing our results. However, besides the $\sim 1\,\mathrm{km\,s^{-1}}$ velocity offset in Ursa Minor, our results are consistent across samples.

Tangential motions. Precise star-by-star proper motions would further test for kinematic disequilibrium. Presently, *Gaia* uncertainties are too large to permit such studies for Sculptor and Ursa Minor.[2]

[2]Specifically, typical proper motion uncertainties for faint, member stars of Scl and UMi are around $0.5\,\mathrm{mas^{-1}\,yr^{-1}}$, corresponding to velocities $\sim 100\,\mathrm{km\,s^{-1}}$.

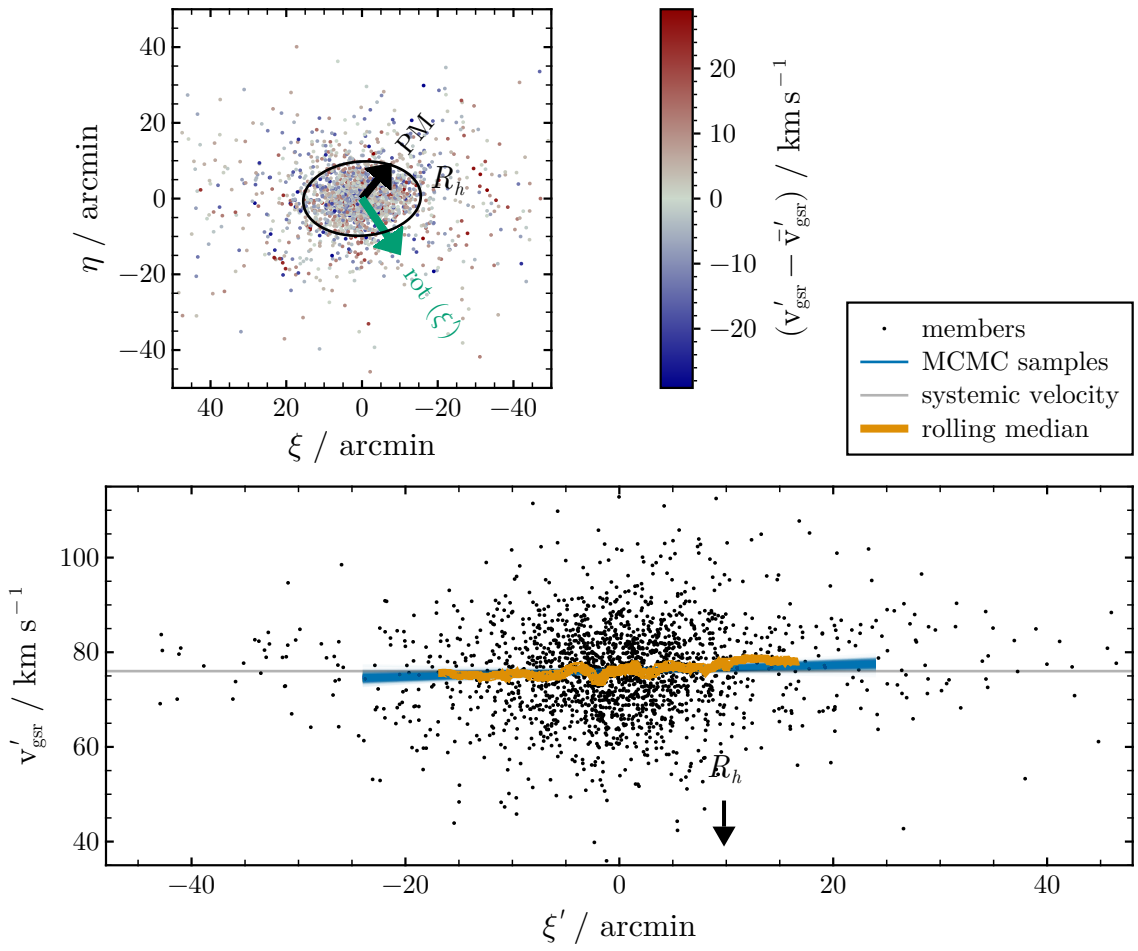

Figure B.2: **Top** members of Sculptor plotted in the tangent plane, coloured by corrected velocity difference from mean $v'_{\rm gsr} - \bar{v}'_{\rm gsr}$. The black ellipse marks the half-light radius in Fig. 2.1. The black and green arrows mark the proper motion (PM, GSR frame) and derived velocity gradient (rot) vectors (to scale). **Bottom**: The corrected LOS velocity along the most likely rotational axis. RV members are black points, the systematic $v''_{\rm gsr}$ is the horizontal grey line, blue lines represent the (projected) gradient from MCMC samples, and the orange line is a rolling median (with a window size of 50).

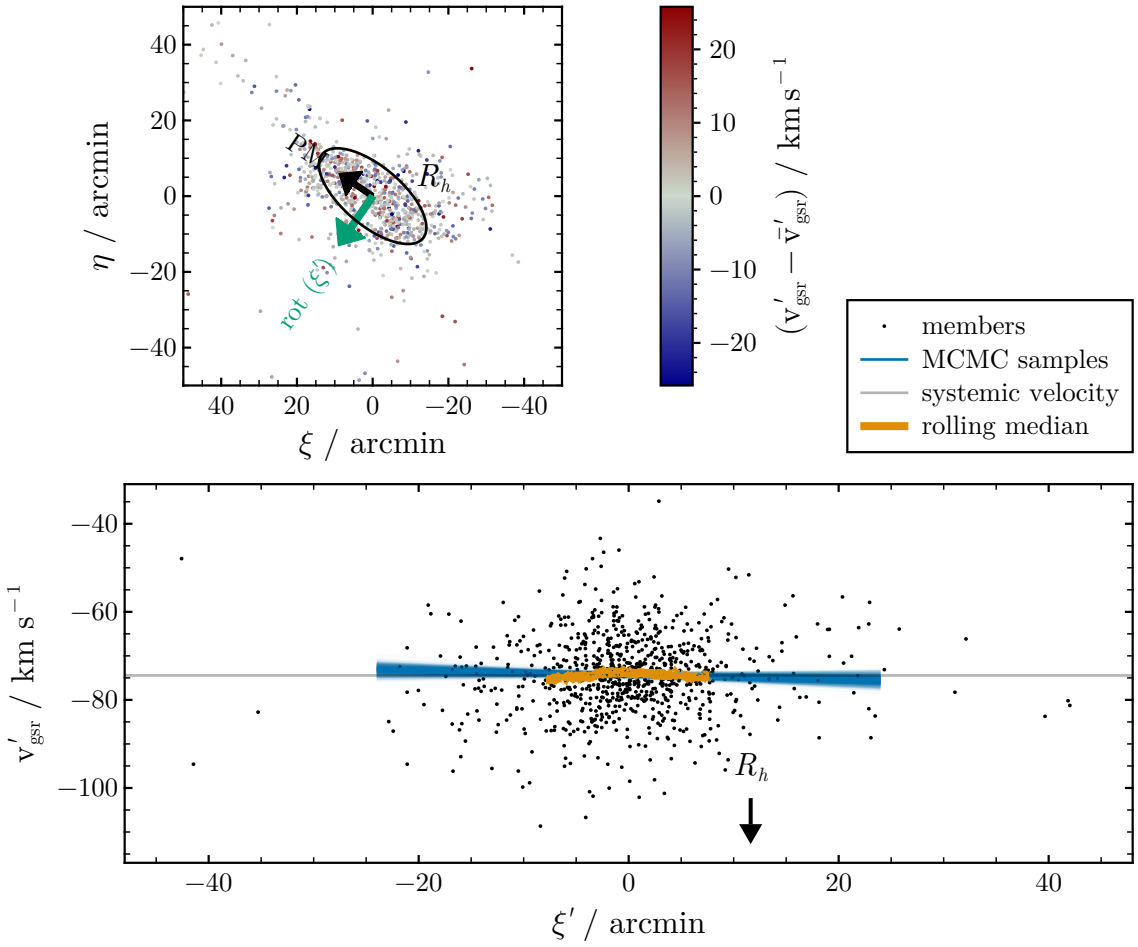

Figure B.3: Similar to Fig. B.2 except for Ursa Minor. Ursa Minor does not have clear evidence of a velocity gradient.

B.5 Summary

In this section, we analyze literature samples of LOS velocity measurements for both Scl and UMi. In each case, we find systemic velocities and dispersions consistent with past work. We detect weak evidence for a velocity gradient in Scl, but the gradient is misaligned with the proper motion of Scl, so it is unlikely to be of tidal origin. Sculptor also shows evidence for a mildly rising velocity dispersion with radius; however, the outer regions appear to be flat in velocity dispersion. The lack of observational evidence for ongoing tidal disruption in the velocity distribution of stars in Scl and UMi further supports our interpretations in the main text.

C. Numerical convergence and parameters

Here, we describe the numerical specifics of our simulation and analysis. We present convergence tests supporting our choices of softening and additional parameters. We find that alternate choices of numerical parameters neither improve convergence nor the resulting evolution.

Due to the finite resolution of N-body simulations, collisional (close) encounters between particles are inevitable. Such collisional encounters are both unphysical (with possible arbitrary acceleration, violating the "collisionless" assumption) and computationally expensive (requiring many small time-steps). As a remedy, many N-body codes use a *softened* gravitational force law, where the force weakens when closer to a particle than a *softening length.* The choice of softening length ideally balances resolution and computational speed.

Empirically, Power et al. (2003) suggest that the ideal softening is

$$h_{\rm grav} = 4\frac{R_{200}}{\sqrt{N_{200}}}, \tag{C.1}$$

where $h_{\rm grav}$ is the softening length, and N_{200} is the number of particles within R_{200}. This choice balances integration time and only compromises resolution in the collisional regime. For our isolation halo ($r_{\rm max} = 6\,{\rm kpc}$, $v_{\rm max} = 31\,{\rm km\,s^{-1}}$) with 10^7 particles, this works out to be $0.044\,{\rm kpc}$. Next, we consider the effect of softening as applied to our isolation halo.

The top panel of Fig. C.1 illustrates the influence of softening length for simulations of Scl's `smallperi` orbit with 10^5 particles. We show a model with the fiducial softening length ($h = 0.14\,{\rm kpc}$), and larger and smaller softenings by a factor $\sqrt{10}$. The larger softening length is consistent with Eq. C.1's prediction. With a larger softening length, the halo diverges from the expectation (using $100\times$ more particles) across most radii. On the other hand, the fiducial and smaller softening lengths predict similar final results. As computation time increases with decreasing softening length, the fiducial softening length balances efficiency and accuracy for this simulation.

The two other key numerical parameters in GADGET-4 are the tree-force and time-step accuracy parameters. Specifically, GADGET-4 opens a node if $M\,l/r^3 < \alpha|a|$, where the node's mass is M, the distance from the particle is r, the side-length is l, and the particle's

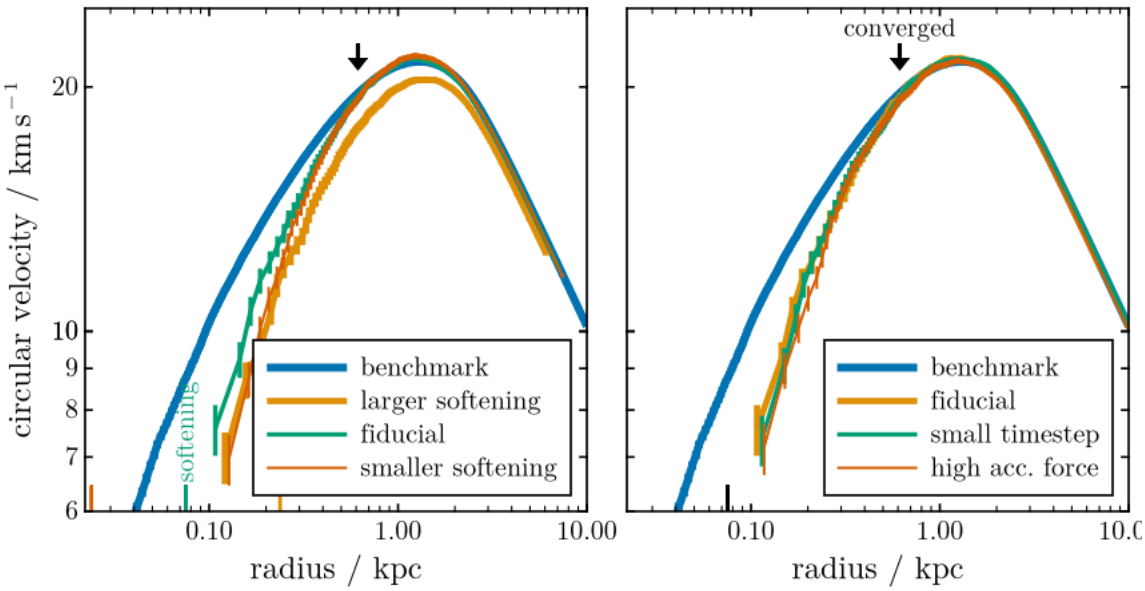

Figure C.1: Similar to Fig. 3.5, except a comparison of the final velocity profiles using different simulation methods for Sculptor's `smallperi` model. The benchmark model is our fiducial 10^7 particle run, and all other models use 10^5 particles, with their "converged radius" marked by the black arrow and softening by the vertical bar(s). **Left:** Models with $\sqrt{10}$ larger and smaller softening lengths than the fiducial. **Right:** Models with more precise timestep accuracy and gravitational force accuracy.

total acceleration is a. We adopt $\alpha = 0.005$. We also elect to use adaptive time stepping with integration accuracy set to $\eta = 0.01$. (particles must take time-steps smaller than $dt < \sqrt{2\,\eta\,h_{\rm grav}/a}$ for acceleration a). The lower panel of Fig. C.1 tests changes to these parameters. We include a model with smaller integration accuracy ($\eta = 0.003$ in "small timestep") and a stricter tree-force tolerance ($\alpha = 0.001$, "high acc. force"). More precise tolerances on these parameters do not affect the evolution within the uncertainties of the final profile.

As demonstrated in this subsection, stricter numerical accuracy and modified softening lengths do not affect our results. We thus conclude that our simulations are numerically well-converged (up to the "convergence" radius).

D. Additional Simulation Results

In this section, we briefly explore additional simulations testing variations in the halo concentration, cored halos, alternative orbits, anisotropies, and ellipticities. While each of these variables influences total dark matter evolution, the resulting inner structure is similar across models. We conclude that consideration of these effects likely would not change our conclusions.

D.1 Alternative initial conditions

The following models aim to reproduce the stellar velocity dispersion of Sculptor to within $\lesssim 1\,\mathrm{km\,s^{-1}}$ with a similar present-day half-light radius.

D.1.1 Halo concentration

Changing the initial concentration (or v_{max} and r_{max}) primarily affects total dark matter evolution. Fig. D.1 compares models on the `smallperi` orbit with different initial halo parameters. The heavier halo has $v_{max} = 43\,\mathrm{km\,s^{-1}}$ and $r_{max} = 7\,\mathrm{kpc}$, whereas the lighter halo has $v_{max} = 25\,\mathrm{km\,s^{-1}}$ and $r_{max} = 2.5\,\mathrm{kpc}$. While the less concentrated halo loses more mass, the halo evolves to similar final structural parameters.

The heavier halo diverges from the initial point orbit more substantially. We show the results of correcting the orbit (akin to Ursa Minor's correction, see Section 3.1.4) in Fig. D.1 as the "heavier, new orbit" halo. Since correcting the orbit has a relatively small effect on the tidal evolution, we neglect these corrections in further comparisons for simplicity.

D.1.2 Dark matter cores

Many dwarf galaxies appear to have dark matter cores. In Scl, the presence or absence of a core has been debated (e.g., Battaglia et al. 2008; Walker et al. 2009b; Agnello & Evans 2012; Breddels & Helmi 2013; Amorisco et al. 2014b; Richardson & Fairbairn 2014). To

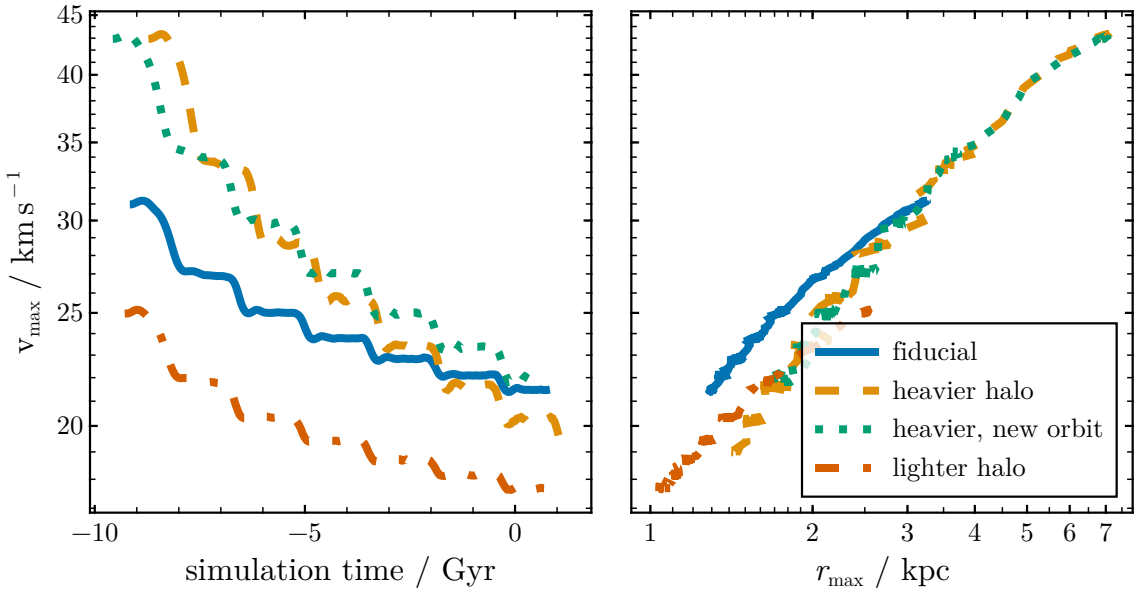

Figure D.1: A comparison of the evolution of different N-body models for different halo concentrations (heavier and lighter halo), and the heavy halo with the action-angle corrected orbit. **Left:** The maximum circular velocity v_{max} of the dark matter halo is plotted as a function of simulation time. **Right:** v_{max} is instead plotted as a function of r_{max}.

simulate the evolution of a cored dark matter halo, we adopt a "cored-NFW" model,

$$\rho/\rho_s = \frac{1}{(1+r/r_s)^2(r_c/r_s + r/r_s)}, \tag{D.1}$$

where r_c is the core radius. We set $M_s = 0.54 \times 10^{10}\,M_\odot$ where $M_s = 4\pi/3\; r_s^3 \rho_s$, $r_s = 1.08\,\mathrm{kpc}$, $r_c = r_s$, and use the same truncation as our fiducial halo (Eq. 3.3). We plot the initial and final density, as compared to a cuspy NFW, in Fig. D.2.

In Fig. D.3, we show the evolution of the cored model as compared to a heavier halo. The cored halo appears to evolve more mildly than the NFW halo. This is possibly because, to match the velocity dispersion, the cored halo has $\sim 50\%$ more mass within 1 kpc than a similar cuspy halo.

D.1.3 Velocity anisotropy

Velocity anisotropy quantifies the number of radial versus circular orbits. Specifically, the anisotropy parameter, $\beta = 1 - \frac{\sigma_\phi^2 + \sigma_\theta^2}{2\sigma_r^2}$ where σ^2 is the velocity dispersion in the spherical r, ϕ, or θ direction. Radial velocity anisotropy may cause halos to disrupt faster (e.g. Chiang et al. 2024). To test the effects of moderate velocity anisotropy, we initialize a model with

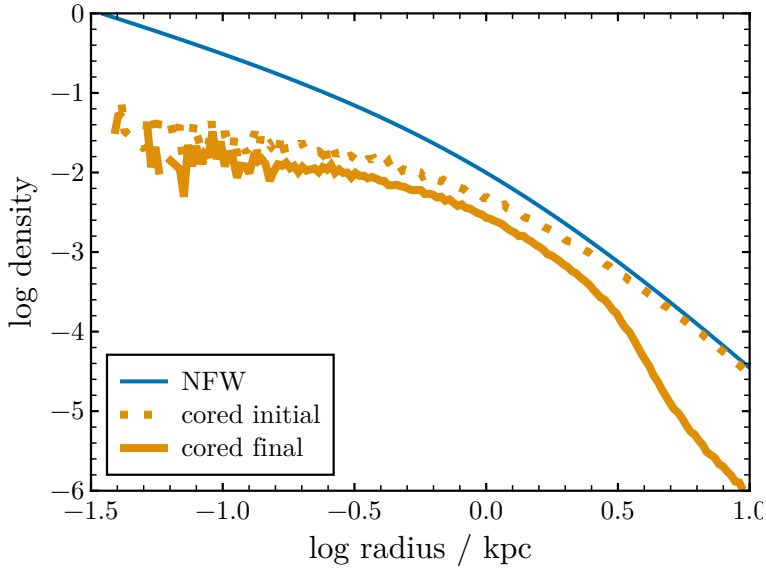

Figure D.2: The initial (dotted orange) and final (solid orange) 3D density profiles for the cored model of Scl on the `smallperi` orbit. The blue thin line represents an NFW halo with the same M_s and r_s.

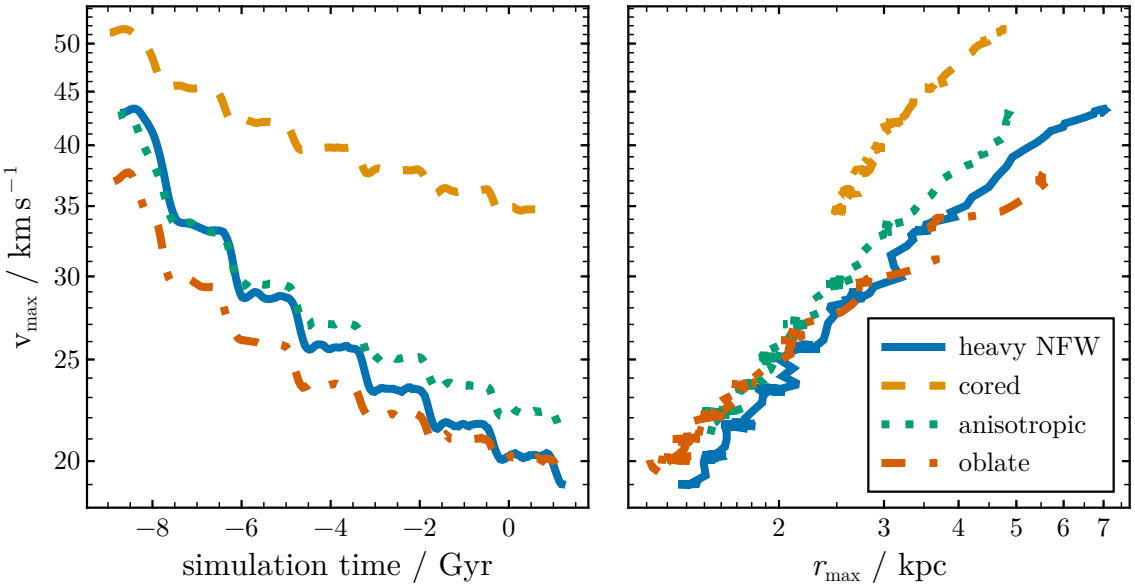

Figure D.3: Similar to Fig. D.1, except testing the effects of including a core, velocity anisotropy, and evolving an oblate halo. While the normalization may differ, the tidal evolution is similar.

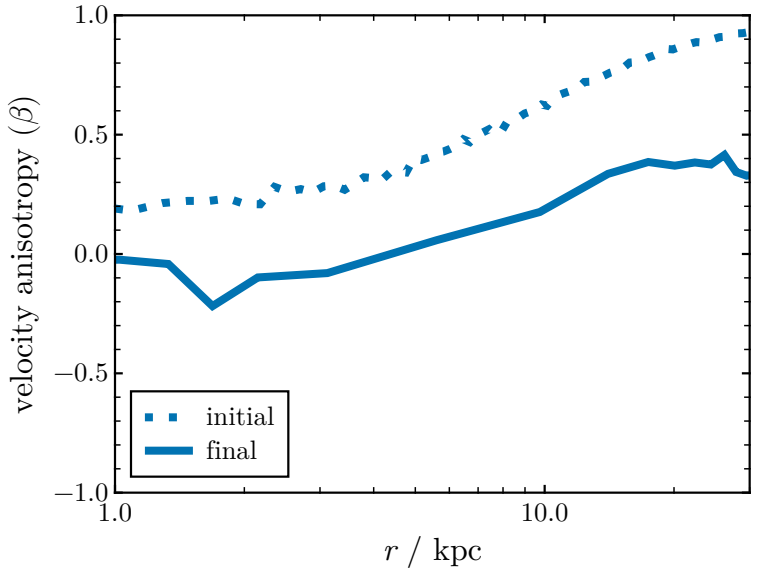

Figure D.4: The initial and final anisotropy profiles for the initially anisotropic model of Scl on the `smallperi` orbit. The final profile is more isotropic (closer to $\beta = 0$) than the initial.

a velocity anisotropy with an Osipkov-Merritt profile rising from $\beta = 0.2$ at the centre to $\beta = 1$ and infinity, with scale length $4r_s$.

Fig. D.4 shows the initial and final anisotropy profiles after tidal evolution on Scl's `smallperi` orbit. The dwarf galaxy becomes more isotropic with tidal evolution. Particles on more radially anisotropic orbits are more easily stripped as they have larger apocentres than more circular orbits of the equivalent energy. Regardless, the overall tidal evolution is very similar to our fiducial, isotropic case (see Fig. D.3).

D.1.4 An ellipsoidal halo

Sculptor and Ursa Minor may be highly elliptical in 3D, possibly violating the assumption of spherical symmetry (e.g., An & Koposov 2022). Although, the shape of the underlying dark matter halo is unknown.

We create an oblate initial dark matter halo using Agama. Fig. D.5 shows the initial equilibrium (after 5 Gyr in isolation) isodensity contours of our model. The initial snapshot

is sampled from the distribution function

$$f(\mathbf{J}) = \frac{M_0}{(2\pi J_0)^3}\left[1+\left(\frac{J_0}{h(\mathbf{J})}\right)^{\eta}\right]^{\Gamma/\eta}\left[1+\left(\frac{g(\mathbf{J})}{J_0}\right)^{\eta}\right]^{-B/\eta} \exp\left[-\left(\frac{g(\mathbf{J})}{J_{\rm cutoff}}\right)^{\zeta}\right], \tag{D.2}$$

(`doublePowerLaw` in Agama), with $g(\mathbf{J}) = g_r J_r + g_z J_z + (3 - g_r - g_z)|J_\phi|$ and $h(\mathbf{J}) = h_r J_r + h_z J_z + (3 - h_r - h_z)|J_\phi|$. The `example_doublepowerlaw.py` script in Agama solves for the best parameters matching a given density profile. We chose to create a model resembling an NFW but scaled by a factor of 0.5 in the z-axis. For a scale-free halo ($r_s = 1$, $M_s = 1$), the best-fit parameters are $J_0 = 0.890$, $\Gamma = 1.46$, $\eta = 0.568$, $B = 2.97$, $h_r = 0.845$, $h_z = 1.66$, $g_r = 0.753$, $g_z = 1.69$, $M_0 = 0.965$, $J_{\rm cutoff} = 2.40$, $\zeta = 20$. The resulting initial conditions are stable in isolation and produce a halo with near the desired density profile and ellipticity. We scale the halo to have a major axis density profile equivalent to an NFW with $r_{\rm max} = 7$ kpc and $\mathrm{v}_{\rm max} = 48$ kpc.

We find the evolution of the oblate halo to be nearly identical to the spherical halo (see Fig. D.3), similar to Battaglia et al. (2015). The oblate halo becomes spherical after tidal evolution (Fig. D.5). If Scl's dark matter halo is indeed elliptical today, this model may not be an adequate description.

D.1.5 Orbital variation

As discussed in Section 4.3.2, the long-term orbit of Scl is uncertain. For a more massive LMC (e.g., the L3M11 model), Scl may have undergone an extreme pericentric passage with the MW ~ 6 Gyr ago. We find that the 3σ smallest pericentre is 4 kpc, and simulate this model to test if such a pericentre may be sufficient.

Because of the strong tidal interaction with the MW, the trajectory is substantially perturbed from a point orbit. We adjust the initial conditions by comparing the change in actions (as calculated in the static MW-only potential) before and after the pericentre. Our final model, the `MW impact` model, can approximately reproduce the observed position of Scl (see Fig. D.6). The model has a Galactocentric initial position of $[67.83, -352.2, 110.3]$ kpc and velocity of $[-3.68, 30.79, -22.77]$ km s^{-1}.

Fig. D.7 compares the tidal evolution of Scl on the mean, `MW impact`, and `smallperi` orbit. The mean orbit loses less mass than the `smallperi` model. Instead, the `MW impact` orbit experiences most tidal evolution during its first MW pericentre. While evolving further along the tidal track, the stars of this model nevertheless remain exponential (Fig. D.8). We

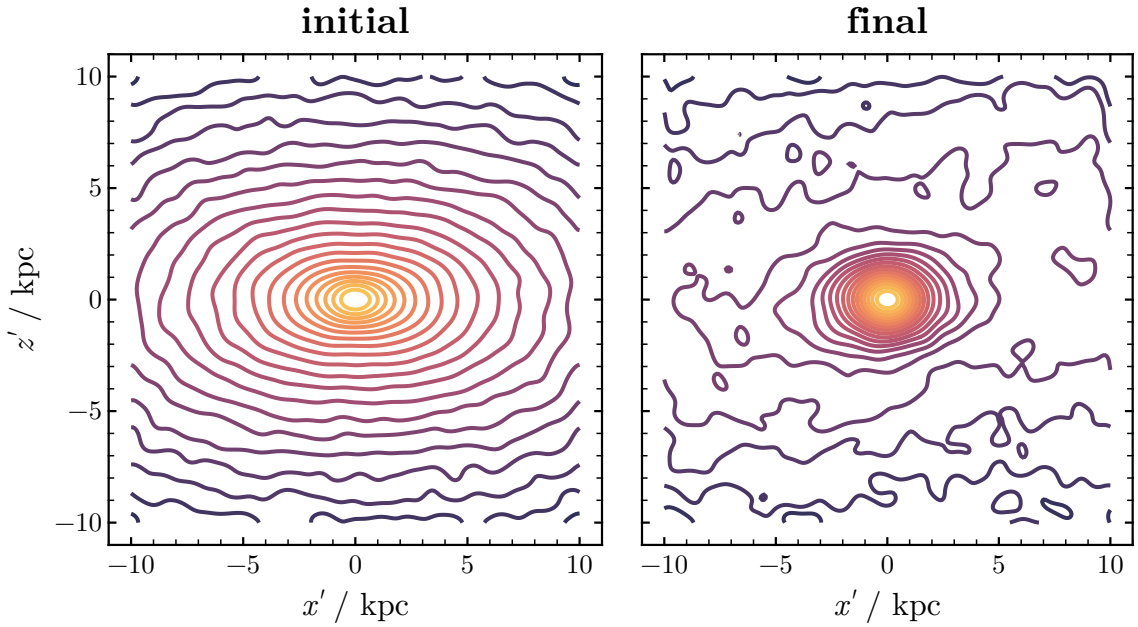

Figure D.5: The initial and final (after 9 Gyr of tidal evolution) projected density profiles for the oblate halo on Scl's `smallperi` orbit, projected on with x' and z' the major and minor axes. The contours are drawn assuming normal smoothing of 0.4 kpc and are log-spaced with intervals of 0.1 dex.

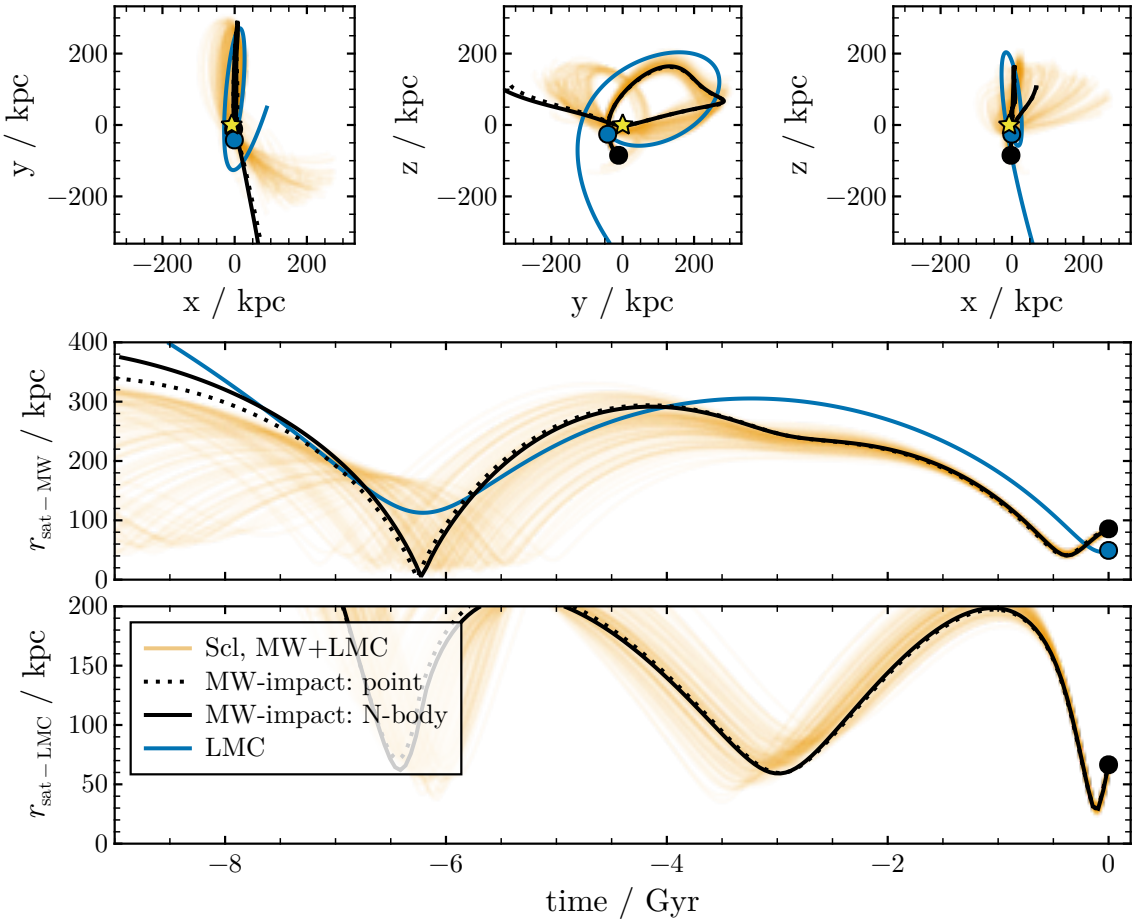

Figure D.6: Similar to Fig. 4.5, except for the orbit of Sculptor for the MW-impact model. The point (dotted) and N-body (solid) diverge by ~ 50 kpc at early times.

suggest that the impulsive pericentric passage does not occur for long enough in this model to produce the expected extended density profile. A yet more extreme orbital history would be necessary to tidally transform Scl's stars.

D.2 The formation of tidal tails

As discussed in Section 4, any hints of a possible tidal stream around Scl and UMi are beyond the reach of current observational facilities. However, we can still predict the properties of such a stream.

Fig. D.9 and Fig. D.10 show the resulting distributions of velocities and distance along the stream orbital axis ξ' for Scl and UMi. The tidal tails may have detectible gradients

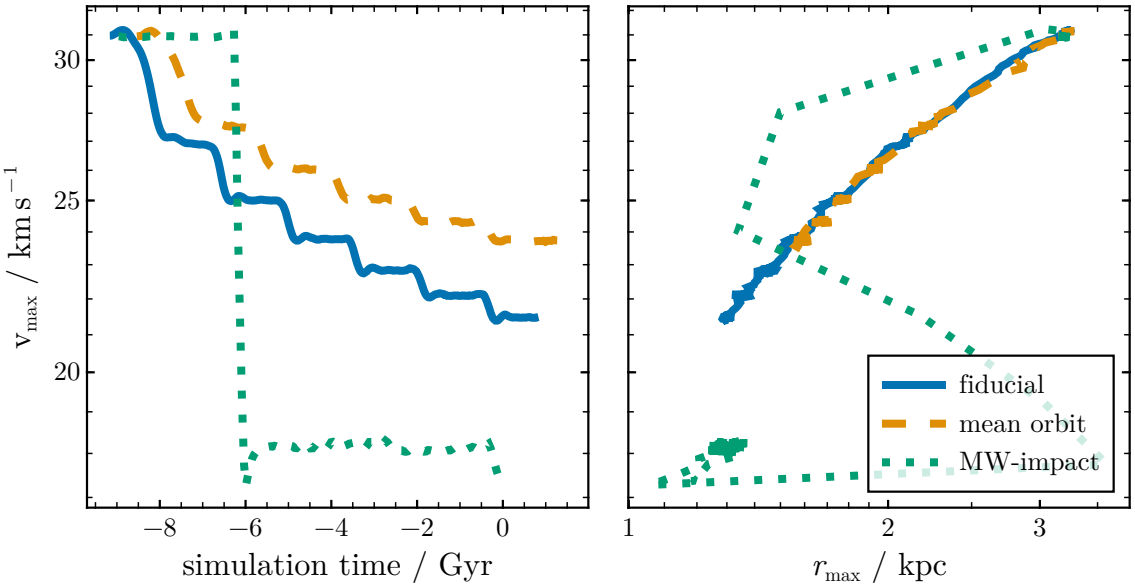

Figure D.7: Similar to Fig. D.1, except testing the effects of orbits in the LMC. Most LMC models evolve more weakly than the MW models.

in radial velocities ($\sim$ 10 km s^{-1} over 5 degrees) and proper motions (mostly for UMi, of $\sim$ 0.1 mas^{-1} yr^{-1} over 5 degrees). However, detecting such a gradient would require tracing stars across several degrees on the sky.

D.3 Summary

While we compared the evolution of orbits of Scl in the MW-only potential for simplicity, we expect the differences between models in the MW and LMC potential to be more slight due to the weaker tidal evolution. And while UMi has a lower pericentre than Scl, the differences between halo structure should apply similarly to UMi. We conclude that our assumptions regarding orbits, halo concentration, cuspyness, anisotropy, and ellipticity likely do not dramatically change our conclusions.

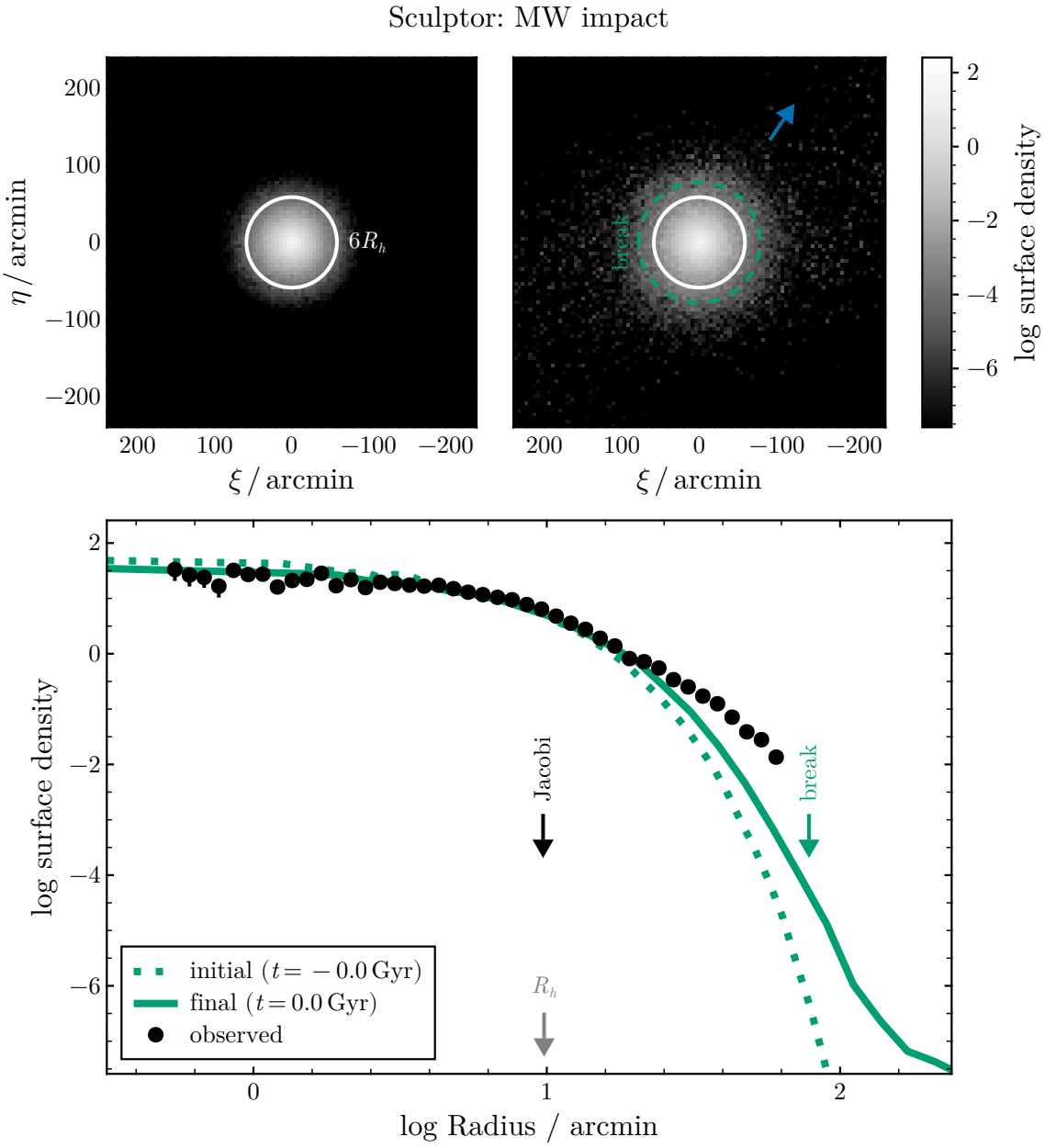

Figure D.8: Similar to Fig. 4.3 except for the orbit of Scl passing through the MW.

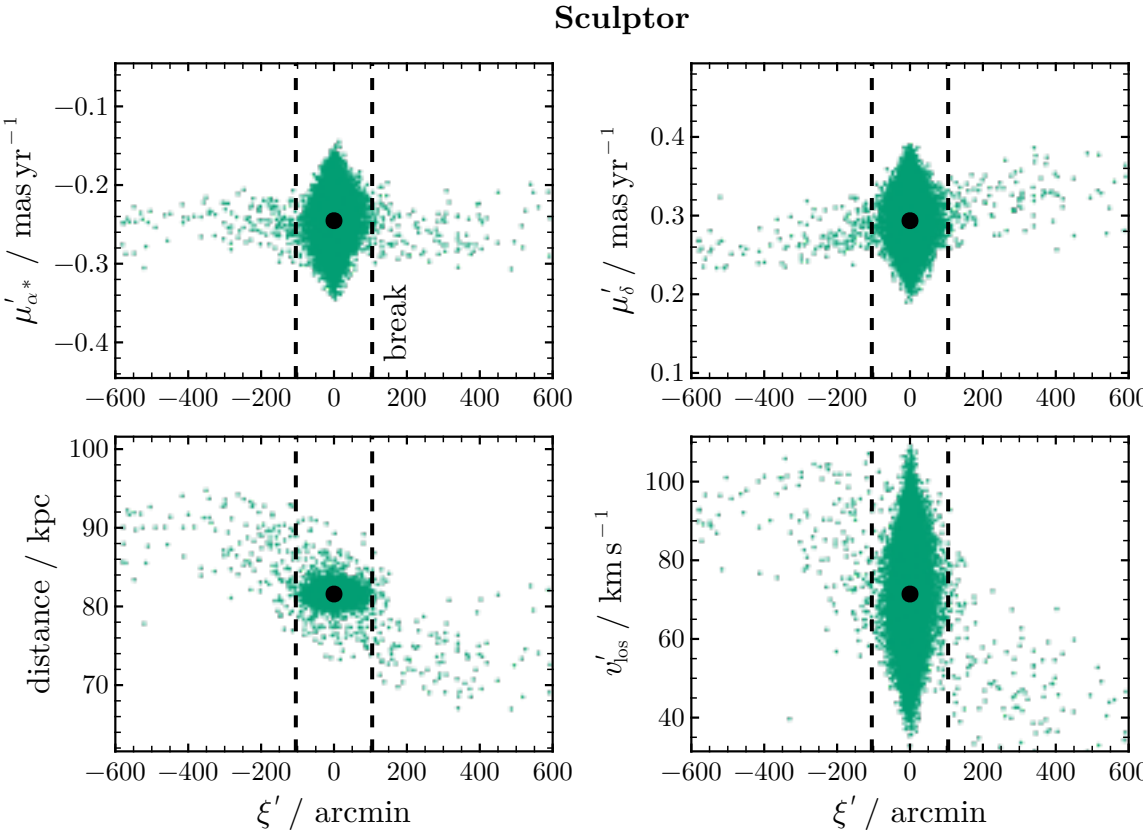

Figure D.9: The predicted properties of a tidal tail in the Scl model. The panels are all as a function of ξ', the distance along the stream as defined by the current GSR proper motion vector. The top panels show the GSR proper motions in RA and Dec, and the bottom two show the distance and GSR radial velocities. To sample the stream, we randomly draw 100,000 samples from the snapshot based on the stellar weights. A detectible gradient in $\mu_{\alpha*}$ and LOS velocity should be detectible if the stream is tracked across several degrees.

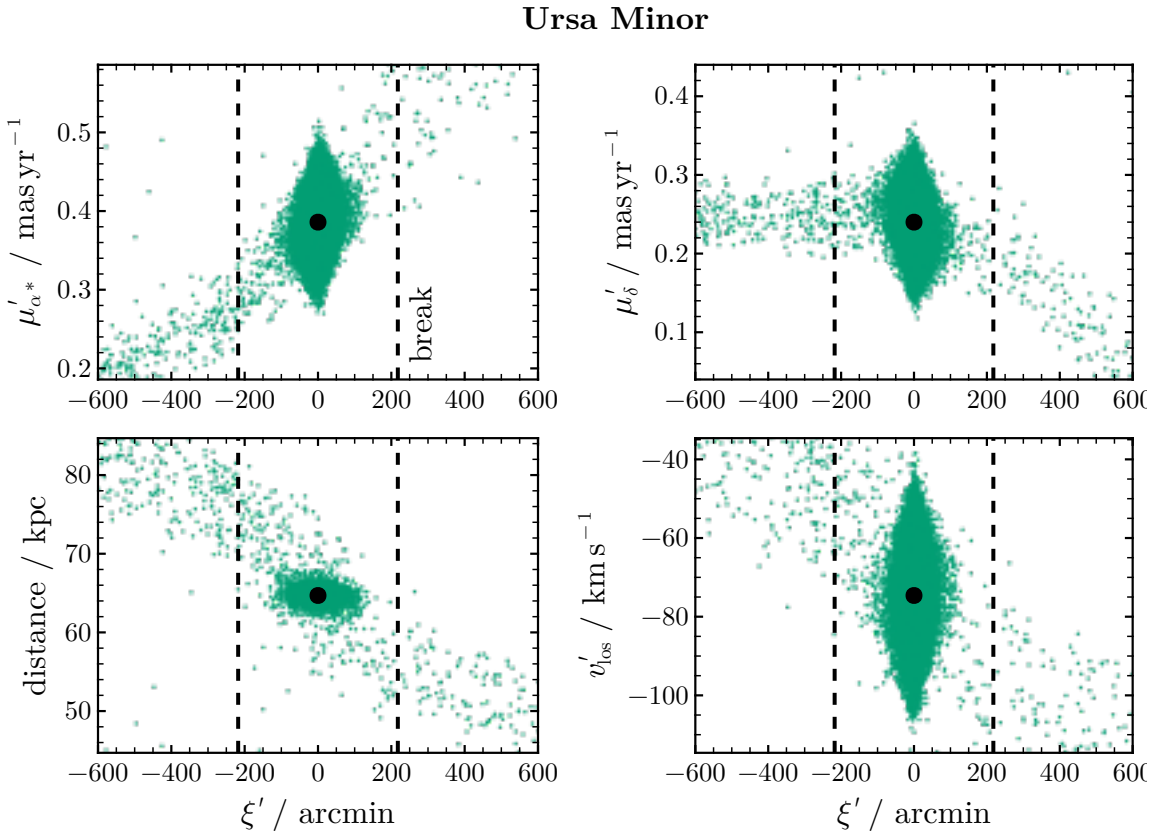

Figure D.10: The properties of the stream around the UMi `smallperi` orbit with Plummer stars.